# Kelvin-Helmholtz Instability in Aluminium Reduction Cells

A thesis presented to the
University of Waikato
in fulfillment of the thesis requirement
for the degree of

Doctor of Philosophy

by

SUNG NAM SHIN
Department of Mathematics

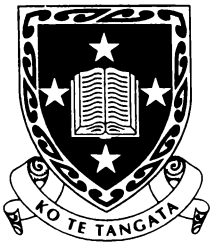


The University of Waikato
*Te Whare Wānanga o Waikato*

30 April 2000

## Abstract

In aluminium reduction cells the intense magnetic fields and associated Lorentz forces drive steady flows in the cryolite and aluminium layers. Generally there is a discontinuity in velocity between the layers, which gives rise to a Kelvin-Helmholtz instability, and the study of this effect is the subject of the thesis.

The role of the basic steady flow is focused in this analysis, while most previous MHD analyses neglect it and emphasise on the interaction between the interface wave and the electromagnetic field by the electromagnetic perturbation. The stationary magnetic field is considered important as a strong driving source for the steady velocity in our model.

Steady velocity fields are studied in terms of a stream function and global stability criteria are discussed with disturbances. Non-linear evolution of flow is investigated to find a steady condition and show that steady flows are stable. A normal mode analysis is used to formulate wave evolution equations, which are integrated forwards in time.

Also an improved treatment of electromagnetic damping is developed, which includes the effect of the induced electric field.

Using a normal mode form of the steady-state current, magnetic field or flow, the scheme developed in this research is suitable for industrial application where these would be calculated numerically.

## Acknowledgements

First and foremost, I would like to thank my supervisors, Associate Professor Alfred Sneyd and Ian Craig for their invaluable advice and support, without which the completion of this thesis would not have been possible. Especially, I appreciate Dr. Sneyd for his enthusiastic guidance during this study as my principal supervisor.

Also I would like to thank the Department of Mathematics and all the staff for providing the facilities and financial support for this research. It was a great privilege for me to study in this lovely environment with my nice colleagues, Dr. M.Reddy, Dr .S.Manda, Dr. K.Ruggiero, Dr. L.Dediu, F.Ali, Dr .Y.Wang and Dr. N.Zhu.

Special thanks go to Dr. Anping Wang and many other authors, although most of them are known to me only through their excellent papers. Assistances from Dr. Stephen Joe and Dr. Alec Zwart in computing works are also most appreciated.

Finally, I would like to thank my wife Hyunju, my daughter Soojeong and my parents for their understanding, love, and support while I was studying. Shalom.

# Contents

# List of Figures

# Chapter 1

# Introduction

Aluminium is produced in Hall-Héroult electrolytic cells. These consist of large carbon anodes suspended in an electrolyte of molten cryolite, below which is a molten pool of reduced aluminium which acts as a cathode. The cryolite is a solvent for the aluminium oxide fed to the cell. Beneath the cryolite is a pool of molten aluminium. The reduction of the aluminium ions to metal occurs at the anodes and the aluminium pool thereby increases. A strong magnetic field is generated by applied electric currents. The liquid aluminium is generally driven faster than the cryolite flow by the electromagnetic forces because of its different material properties such as density, viscosity and electrical conductivity. The electrical conductivity of the materials is especially important. The aluminium is an excellent conductor, the carbon a moderate conductor and the cryolite a very poor conductor. These differences in the electrical conductivity are critical to the current redistribution in the cells.

It is well known that the interface can become unstable due to the stationary electromagnetic field and the steady velocity field driven by it. The velocity difference between the liquid layers can cause the interface to fluctuate, which is known as a Kelvin-Helmholtz instability. Other unwanted disturbances may be triggered at the interface, for example a current flow instability, where gravity waves are modified by the intense electromagnetic force. These waves are observed to grow, damaging the normal operation of the cell.

The analysis of the interfacial instability has always been a great challenge which

needs much time and effort. It has been intensively studied to achieve optimum cell design and operation for the last two decades and more. Although aluminium is one of the most important materials in modern industry, the production cost has always been an issue and depends largely on the electrical power consumption during the reduction process. The main goal is to consume the least electrical energy to produce the most aluminium.

In large-scale reduction cells, a small surface/volume ratio is desirable to minimise heat loss. As these large-scale reduction cells require greater current flow, more intense magnetic forces induced from strong electric currents are generated. The strong magnetic forces and the circulation flows originating from them are considered important factors in cell operation and energy efficiency, as they can seriously disturb the interface between two liquid layers. The unstable interface can make an electric short by direct contact between liquid aluminium and anodes and consume a huge amount of electric energy. Therefore, it is essential that the interfacial instability be controlled.

The main part of this dissertation is devoted to studying the K-H (Kelvin-Helmholtz) instability, which arises from the velocity difference between two liquid layers. It will be shown that the interfacial instability can occur with the different liquid densities and/or with the different steady velocities between the liquid layers, as both cause a pressure imbalance at the interface which transfers energy into the interface disturbance. While the first mechanism arises purely from the density difference even when the velocity field is continuous at the interface, the second mechanism or the K-H instability is much stronger.

Ziegler [85] investigated the effect of the steady velocity on the interface with the first mechanism. Though his work deserves our attention, it seems to be insufficient to explain the cell instability, as the velocity difference is not considered in the analysis. We should consider both the density difference and the steady velocity difference, because there is always a velocity difference between the aluminium and the cryolite layers in a real cell. Since the KH instability is known to be a strong effect (see Section 1.2) it is likely to be the strongest destabilising influence, although there exist also other possible instabilities which will be reviewed in Chapter 2.

A nonlinear cell model will be integrated forwards in time. In order to avoid an

unphysical pressure discontinuity across the layers, we start the system from a state in which both layers are at rest. The steady velocity is gradually increased from zero to a constant value in the transient period of 10 seconds as shown in Figure 5.1. The normal mode techniques, which were developed by Sneyd & Wang [74], are adapted to formulate the wave evolution equations. This leads to a coupled system of nonlinear ordinary differential equations which can be integrated numerically.

In the first section, the background of this dissertation is introduced. We will review the aluminium reduction process and the physical model for the interfacial instability analysis, including cell geometry. In the second section, the difference between the current flow instability and the K-H instability will be briefly discussed in terms of the steady velocity of the basic flow and the stationary electromagnetic field. The layout of this thesis will be presented in the last section.

## 1.1 Background

### 1.1.1 Aluminium reduction process

Aluminium is produced by the electro-chemical reduction of alumina to aluminium. The process consumes much electricity and is represented by the following electro-chemical equilibrium equation:

$$2Al_2O_3 + 3C + \text{ Electrical Energy} \Longrightarrow 4Al + 3CO_2.$$

Strong magnetic fields are generated by the electrical current fields. Then they interact together and cause strong electromagnetic forces, which can drive circulation flows in the molten electrolyte (a mixture of sodium and aluminium fluorides, which is usually known as cryolite) and the molten aluminium contained in the cell and impair the current efficiency. They deform the interface between the two liquids which impedes efforts to reduce electrical energy consumption, although they also have a beneficial stirring effect. It is well known that this electrical energy consumption has always been a major issue in the aluminium industry. Actually, the energy consumption has been reduced remarkably by improved cell design, for example by reducing the ACD (anode-cathode distance) since Charles Hall and Paul Héroult invented the modern reduction process for manufacturing aluminium from

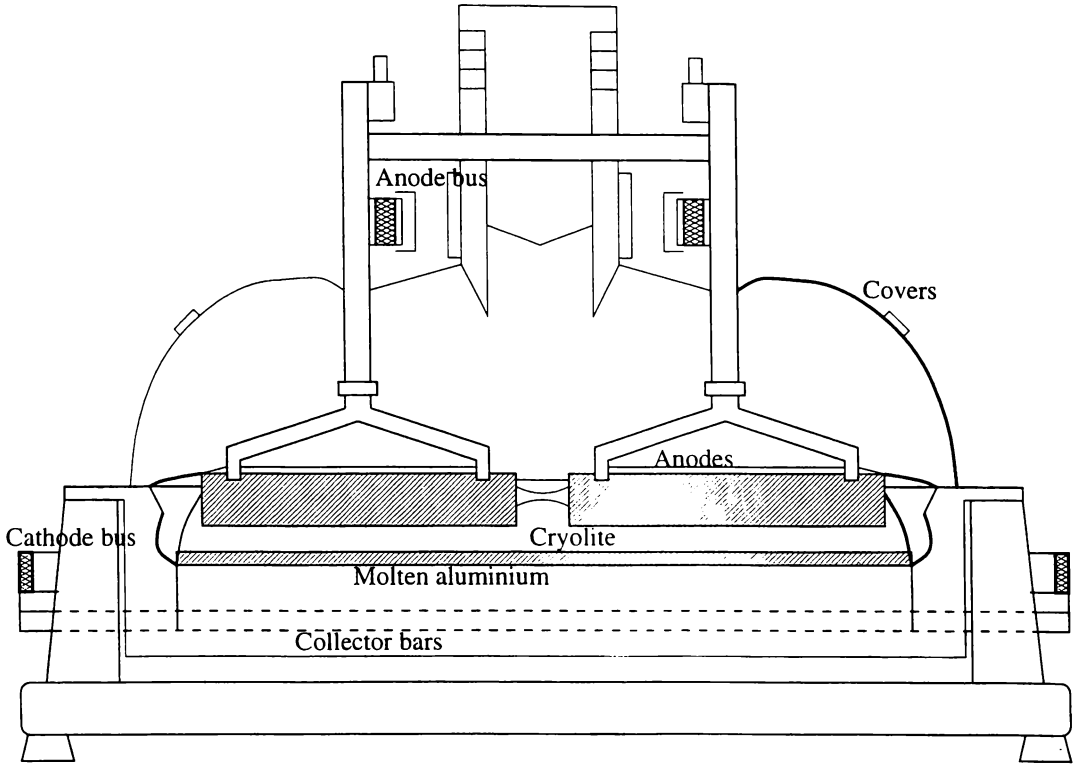


Figure 1.1: Cross-section of an aluminium reduction cell

alumina. It cost about 34kWh to produce one kilogram of aluminium when the first commercial reduction cell was built in 1890. This figure has now been reduced to about 13kWh [83].

A typical cell would carry 100-500kA, contain ten to twenty anodes, operate at 960°C and have a rectangular steel shell 7-12m long, 3-5m wide and 1-2m deep as shown in Figures 1.1 and 1.2. Reduction cells are usually arranged in lines of several tens of cells known as pot-lines and an aluminium plant might contain several pot-lines usually running parallel to one another and a few meters apart. Figure 1.1 shows a cross-section of a typical reduction cell. An inner liner of carbon materials is insulated from the steel shell with refractory material. The insulation by the carbon lining and the frozen cryolite is important for the control of heat efficiency. The normal thickness of the aluminium layer is 0.1-0.2m. The thickness of the cryolite is 0.03-0.05m, which is one of major factors for interfacial instability and energy consumption. A thick cryolite layer often results in the cell being overheated, as it is a much poorer conductor than the aluminium layer. Most Joule dissipation occurs here. On the contrary, a thin cryolite layer may not be able to raise the cryolite temperature high enough for an efficient reduction process. Also, a thin cryolite

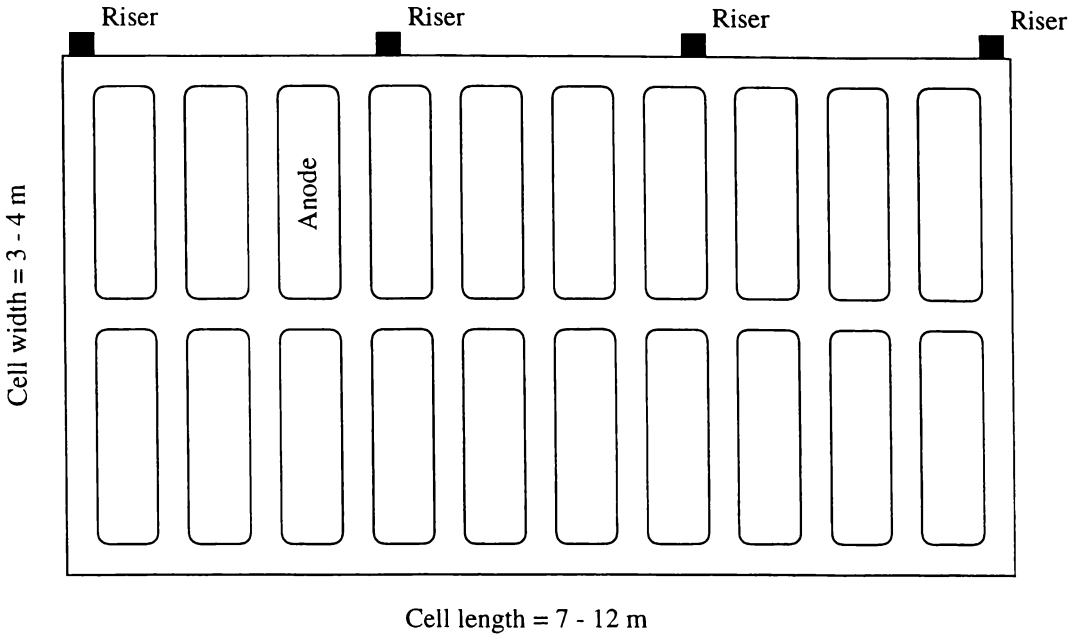


Figure 1.2: Position of anodes

layer may cause an unstable interface, as will be discussed in Chapter 6. The anode must be adjusted regularly to maintain the ACD as the anode carbon is consumed by the reduction process.

The electric current enters from the riser bus, goes to an anode bus from which it is distributed to each anode. Then it flows through the anodes into the electrolyte, into the molten aluminium pool and into the carbon cathode blocks. After passing through the carbon cathode blocks, the current is carried to the next cell through a bus bar system, which interconnects all the collector bars to the riser bus between the cells.

The large currents surrounding conductors and adjacent cells generate strong electromagnetic fields within the two liquids contained in the cell. As the currents pass through these liquids Lorentz forces are developed. These forces cause circulation of the liquids in a predominantly horizontal direction with velocities of the order of $10^{-1}$m/sec. In addition, they cause an undesirable deformation of the interface. The cryolite has much greater resistivity than the other materials and the energy consumption can be significantly reduced if the ACD is minimised. However, there are great penalties associated with making this distance too small. Touching the aluminium with the anode results in local overheating due to excessive current densities and to passage of current through the cell without the usual electro-chemical

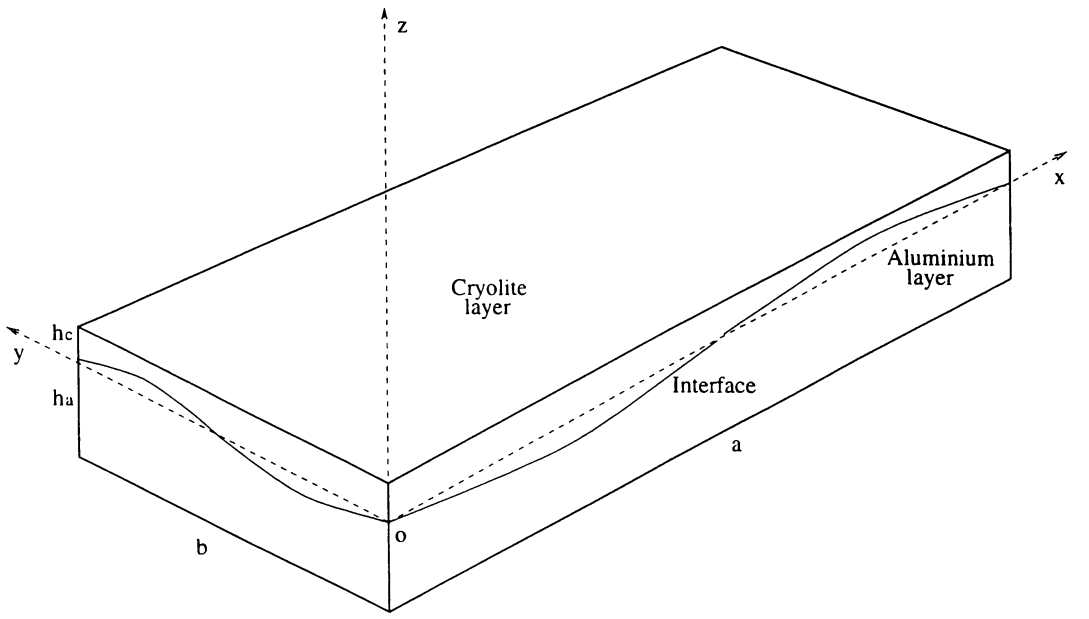


Figure 1.3: A simplified cell geometry.

generation of aluminium. The reduction or elimination of such distortion will therefore result in the ability to run the cell at much lower energy consumption rates. An ACD of about 0.04m is used for a cell.

Aluminium has a slight solubility in the cryolite and this dissolved aluminium is transported from the aluminium/cryolite interface to the vicinity of the anodes where it is reoxidised, presumably by carbon dioxide bubbles. The transport mechanism is convection and turbulent diffusion in the cryolite layer. Therefore the cryolite flow driven by the electromagnetic forces can have an effect on current efficiency. It also has the beneficial effect already mentioned.

### 1.1.2 Mathematical model

Our model consists of a large rectangular box with three horizontal layers representing the liquid aluminium, cryolite and anodes as shown in Figure 1.3. The flat aluminium/cryolite interface is located at $z = 0$ and the $z$-axis is directed upward. The heights of the liquid aluminium and the cryolite are $h_a$ and $h_c$ respectively.

The current densities, magnetic fields, velocities, mass transport rate and current efficiency should be amenable to calculation with some reasonable simplifications. The flows are three dimensional and normally unsteady. The magnetic fields are

affected by the ferromagnetic steel shell. Current distributions within the cell are a function of electro-chemical reactions and contact resistances that are difficult to predict.

In spite of these difficulties, cell analysis appears to be worthwhile. Even idealised calculations can result in reasonable agreement with measurements. The calculations can, to some extent, substitute for measurements which are expensive or impossible in the hostile environment of a real cell. Furthermore they can be an economical alternative to optimisation of actual operating cells. Even quite simple changes in the conductors around a cell would cost tens of thousands of dollars in materials and labour. It will take several days at least to determine the current efficiency and interface geometry for the modified cell. On the contrary, the same modification can be simulated on the computer without spending much time or money.

## 1.2 The current flow instability and the K-H instability

The physics of interfacial instability in aluminium reduction cells has been widely discussed by means of MHD or hydrodynamics. In spite of many theoretical discrepancies among the various analyses arising from the different simplifying assumptions, the production efficiency has been improved greatly by these efforts. It is useful to introduce basic features of the current flow instability and the K-H instability, before we review previous instability theories in Chapter 2.

Moreau & Ziegler [52] showed that two different kinds of instabilities can develop in aluminium reduction cells. One is the classical K-H instability of a sheared interface slightly modified by MHD effects. The other is a MHD instability, essentially electromagnetic, which can generate long wavelength waves (about 1.5m) propagating in the direction of horizontal current.

Later, Ziegler [85] confirmed that the interfacial instability can arise from MHD driven steady flows, even when there is no velocity discontinuity at the interface. Some Russian authors also indicated that the interfacial instability is hydrodynamic

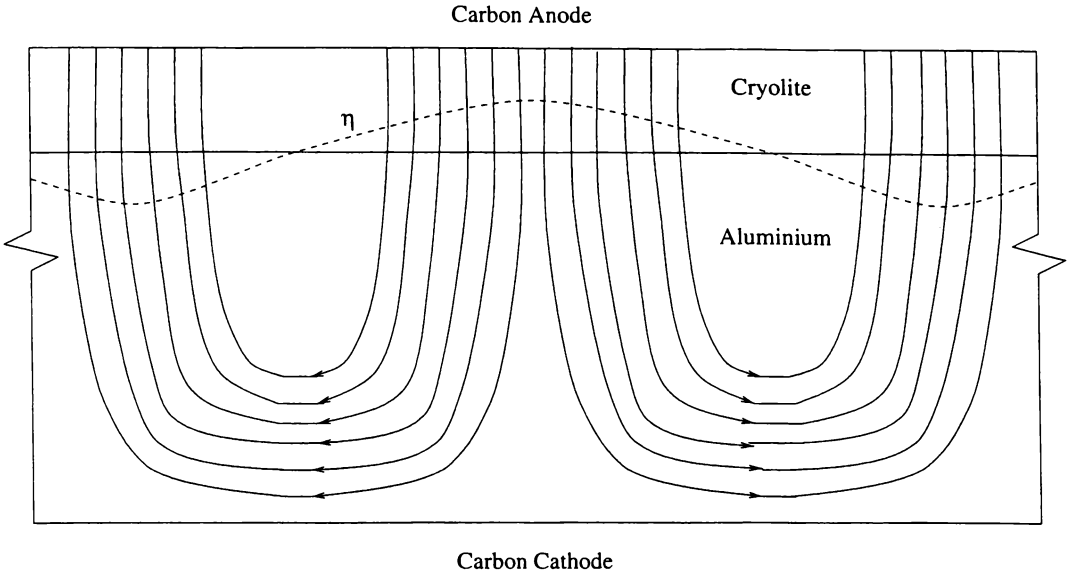


Figure 1.4: Current perturbation due to the interfacial displacement $\eta$ in a cell

rather than MHD in nature (see Almukhametov [2], [3] and Ai [1]). Recently, Wang [83] pointed out the importance of the K-H instability mechanism. Although it is not a new idea completely, the K-H instability approach is remarkable because most other authors (Potočnik [60], [59] & [58], Urata [77], [55] & [54], Leblanc [37], Echelini [24], Medina [43], Kent [32] and other authors [64], [76], [23], [40] & [39]) have dealt with the current flow instability.

In this thesis, we will discuss the above two different interfacial instabilities in aluminium reduction cells - one is the current flow instability with MHD interaction between the interface wave motion and the current flow in a strong magnetic field, and the other is the K-H instability.

### 1.2.1 The current flow instability

As reviewed in previous sections, strong electric current passes through both aluminium and cryolite layers during the reduction process. The current flow is distributed according to the electric conductivities of the layers and the electromagnetic boundary conditions between the layers (see [83] for further details).

Figure 1.4 shows a current perturbation due to the interface wave displacement $\eta$ in a cell, which generates dynamic forces in a strong magnetic field. As cryolite is

a poor conductor, the current flow is diverted through the narrowest part of the cryolite layer. The consequent change in electromagnetic forces may accentuate the layer perturbation. The instability depends crucially on the change in the current distribution. Thus, we call it the current flow instability in this thesis.

It is obvious that the electromagnetic interaction is an important factor in cell instability. However, it does not seem to be so critical always in real cells. Sneyd's analysis [74] supports this very well. He pointed out that typically, when the aluminium/cryolite interface is perturbed, the restoring force due to gravity is much stronger than that due to electromagnetic effects. The resulting oscillation is therefore essentially a combination of normal gravity modes, weakly coupled by the electromagnetic force.

### 1.2.2 The K-H instability

The KH instability is driven by the velocity difference between the aluminium and cryolite layers. In a simplified model as shown in Figure 1.5, a sheet vortex is generated by the steady velocity difference between the liquid layers. When a disturbance is applied to the liquid layers, the growth rate of the sheet vortex $\sigma$ is proportional to the gravitational wave number $n$ and the magnitude of the steady velocity $U$ as follows [9]:

$$\sigma = \mp nU/2.$$

The positive root for $\sigma$ corresponds to an exponentially-growing disturbance, showing that the sheet vortex is unstable to any disturbance periodic with respect to x for which $n \neq 0$. In this instability, no MHD interaction is included. This instability is purely hydrodynamic but owes its existence to the MHD body forces. In Chapter 6, we will discuss the K-H instability further in detail.

In the K-H instability approach, one of our main conclusions is that vertical magnetic field, which is the main source of the horizontal driving force for the steady velocity, is one of most important sources of instability in aluminium reduction cells.

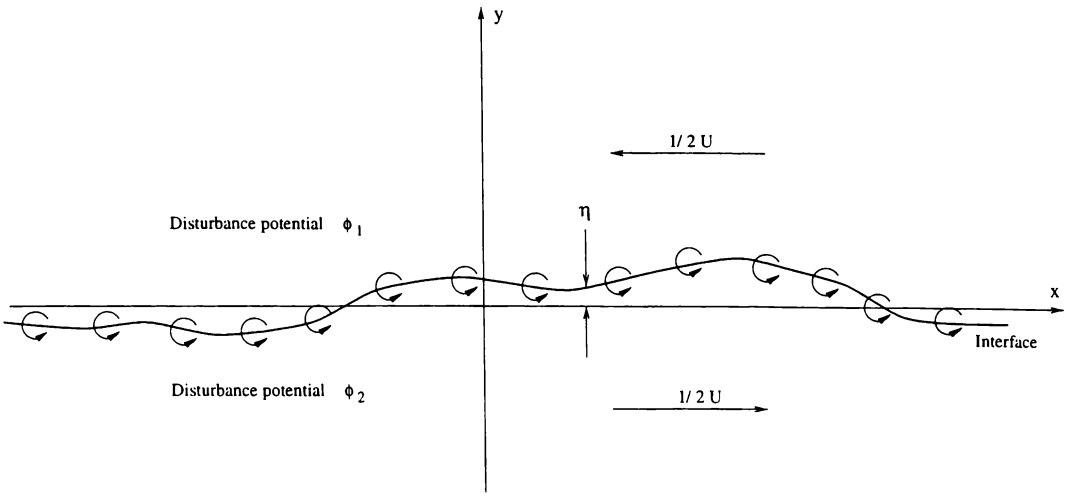


Figure 1.5: A plane sheet vortex to a small disturbance

## 1.3 Scheme of the thesis

The aim of this dissertation is to study the Kelvin-Helmholtz instability and the electromagnetic damping effect in aluminium reduction cells. This research progresses through three main steps. Firstly, we establish a hydrodynamic instability model and formulate wave evolution equations to simulate the interface movement. Secondly, based on this mathematical model, we investigate the K-H instability mechanism. Finally, the effect of the electromagnetic damping force due to the induced current is calculated and compared with previous results.

To investigate the effect of the steady velocity on the interfacial instability more realistically, the steady pressure distribution term at the interface and the initial transient adjustment of the steady velocity are included in our improved model. As the steady velocity term is gradually increased to a constant value in time, we use a time integration method to solve the wave evolution equation instead of normal eigen analysis.

In Chapter 1, the background and the scope of this study is introduced and the general information about aluminium reduction cells is reviewed.

In Chapter 2, we will discuss previous theories and analyses of the interfacial instabilities.

In Chapter 3, basic physics of interfacial instability will be reviewed. The Navier-

Stokes equations, the Maxwell equations, the Lorentz force and the perturbation equations are summarised in this chapter.

We shall discuss the stability of the two-dimensional flows with closed stream lines in Chapter 4. This will give some useful information about the instability of single layer flows in rectangular containers. Based on this study, we find that the instability observed in aluminium reduction cells is not due to an intrinsic instability in the single-layer flows, but the K-H instability mechanism between two liquid layers.

Chapter 5 formulates the wave evolution equations and explores the K-H instability, which is the main part of this thesis. We shall establish our model with some physical and mathematical assumptions, formulate the dynamic equations with the normal mode method and verify the numerical model by testing gravity-wave periods and energy conservation.

The numerical simulations for the K-H instability and the results will be discussed in Chapter 6. Various cell design and operation parameters such as the steady velocity magnitudes, ACD, damping coefficient, cell dimension and liquid metal depth will be included in this discussion.

In Chapter 7, we will formulate and evaluate electromagnetic damping due to the induced current, which is a stabilising effect. The numerical results will be compared with previous work.

Finally, we shall summarise and conclude the research results in Chapter 8.

# Chapter 2

# Review of literature

The physics of the interfacial instability is well known, but its application to improving cell design has always been a great challenge. The strong current and the associated magnetic field generate electromagnetic forces which are useful for maintaining an even temperature distribution by stirring the bath, but which may also cause many undesirable effects by driving the steady velocity in the liquid layers. Also, they affect the interface movement by the electromagnetic interaction.

In this chapter, we briefly review and discuss the major instability theories introduced in the past two decades. During this period, numerical analysis has emerged as an important tool in applying the theories. The analytical approach is seldom possible, as the theory becomes more complicated [35]. The disagreements between the theories have their origins in the different assumptions made in describing the physics of the cell.

## 2.1 Introduction

In this section, we first give a brief list of the papers and then will discuss each in more detail in Section 2.2.

Urata [79], [77] is the first author to formulate an approximate wave equation for the interface to investigate the MHD effects in aluminium reduction cells. His work

highlighted the destabilising of horizontal gradients in the vertical background magnetic field.

Several previous authors (Sneyd [72], Moreau & Ziegler [52], Pigny & Moreau [57], Potocňik [59] and Descloux, Flueck & Romerio [20]) have analysed the linear stability of the interfacial waves and concluded that the magnetic field distribution and the ACD are all important factors. It was indicated by Urata and Potocňik that unstable modes are of relatively long wavelength (one meter or more). Moreau & Ziegler [52] emphasised the importance of horizontal distribution of a vertical cell current. They show a horizontal component of current in the steady aluminium layer can give rise to unstable waves on the interface.

The first self-consistent MHD instability theory was established by Sneyd [72] using a horizontally infinite model. It was found that the external magnetic field could drive a long-wavelength instability which became easier to trigger as the ACD diminished. This work was extended [73] later to show that a much stronger instability arises from the vertical gradient in the horizontal background magnetic field. His analysis relies on a perturbation technique.

Moreau & Ziegler [52] developed a similar model in which the field and the current are uniform, but with a horizontal current component in the aluminium layer. The drag force was assumed to depend linearly on the velocity vector by Moreau. Davidson [16] examined the effect of vertical magnetic field or the vertical gradient of the horizontal magnetic field.

Ziegler [85] suggested a time integration method in which a small perturbation to the interface is given as an initial condition for evaluating the coefficients of the next time step. The stability of a system can be measured by a form of energy expressed in terms of the wave evolution coefficients. This method is an alternative to solving the eigenvalue problem.

A recent study by Sneyd & Wang [74], [83] considers a system of coupled ordinary differential equations for time-development of the mode amplitudes and shows that instability can occur via mode interactions by the electromagnetic perturbation force due to one mode feeding energy into the other. They studied the effect of cell dimensions, electric current density and magnetic field.

Bojarevics and Romerio [13] derive equations very similar to Sneyd and Wang's work. The governing equations couple hydrodynamic variables and electric current. Modified gravitational waves were examined, which can be either purely oscillating or exponentially growing. With an approximation method, the eigenvalues of the two interacting modes were deduced from the wave equations.

Davidson & Lindsay [17] derived a sufficient condition for the interface stability from the MHD coupled equations without extracting the eigenvalues. Using Gershgorin's theorem [34] to estimate the eigenvalues of the coupled system of equations they produced a new instability criterion for both travelling and standing waves.

## 2.2 Instability theories

### 2.2.1 Urata equation for single Fourier-component wave

After the first formal research on the cell instability was reported by a group of engineers at Mitsubishi, Urata was the first author to formulate the interfacial wave equations using shallow water theory [79]. He derived linearised perturbation equations from the two dimensional Navier-Stokes equation in Cartesian coordinates.

It is well known that the electromagnetic forces affect the interface oscillation, as shown in the Urata equation (2.1). When we assume that both the liquids are steady and the vertical electromagnetic force is negligible, it is written as

$$\nabla^2\eta = \frac{1}{(\rho^c - \rho^a)g}\left(j_y\frac{\partial B_z}{\partial x} - j_x\frac{\partial B_z}{\partial y}\right), \tag{2.1}$$

where $\eta$ represents the interface wave displacement. The horizontal component of the electromagnetic force is induced by the interaction between the vertical magnetic field $B_z$ and the horizontal current $j_x$, $j_y$. The interaction between the vertical current $j_z$ and the horizontal magnetic field $B_x$, $B_y$ can be neglected since it does not contribute to the slope of the liquid metal due to the continuity at the interface. The above equation shows that the gradients of the vertical magnetic field $\frac{\partial B_z}{\partial x}$, $\frac{\partial B_z}{\partial y}$ affect the slope of the liquid aluminium surface. The horizontal current around the metal pad interacts with the vertical magnetic field and induces the strong horizontal flow of the metal. The uniform component of $B_z$ contributes only to

the circulation of the metal, while the horizontal gradients of $B_z$ contribute to the interface displacement.

Segatz [65] separated the total transferred energy into components caused by the different terms of the electromagnetic forces as shown below. Most of the kinetic energy is transferred by the terms involving the vertical magnetic field $B_z$ and the horizontal current $j_x$, $j_y$.

| | |
|---|---|
| $B_x(j_z u_y - j_y u_z)$ | -10.6% |
| $B_y(j_x u_z - j_z u_x)$ | 0.7% |
| $B_z(j_y u_x - j_x u_y)$ | 92.1% |
| $J_x(b_y u_z - b_z u_y)$ | 21.7% |
| $J_y(b_z u_x - b_x u_z)$ | 0.0% |
| $J_z(b_x u_y - b_y u_x)$ | -3.9% |

In this theory, the mechanism that drives the instability is the interaction of the vertical field with the local currents set up in the metal by an arbitrary electrolyte-metal interface disturbance (see Urata & Mori [79], Shiota & Ikeuchi [54] and Urata [77]). This engenders forces that propagate the interface disturbance. This method is based on solution of a wave equation for the interface of a specific cell, so that values of the magnetic fields are input from a theoretical model or from measured values of the cell. Their conclusion is that horizontal gradients of the externally imposed vertical magnetic field are the main causes in destabilising the interface.

### 2.2.2 Sele's instability model

Sele ([68], [69], [70] and [71]) has studied the interfacial instability based on a numerical flow model. A local increase in the height of the electrolyte-metal interface leads to an increase in the local vertical current density in the bath. This increase in current spreads out horizontally in the metal pad. The horizontal currents interact with the vertical magnetic flux density to produce a horizontal force in the metal pad, normal to the slope of the interface. This causes the interface to rotate, leading to a wave that travels around the cell. A stability criteria is devised correlating the ACD, metal depth, cell current and the vertical magnetic flux density. He derived an instability criterion by extracting eigenvalues in a finite rectangular cell on the basis of a simple dynamic model, which described the motion of a rotating tilted interface due to the interaction between horizontal electric currents and a vertical

magnetic induction field. Sele's conclusion is that a weak vertical magnetic field gives the most stable cells.

### 2.2.3 Moreau and Ziegler's instability model

Moreau & Ziegler [52] also explained a mechanism for an electromagnetic instability that depends on the interaction of the magnetic field caused by an interface disturbance or perturbation with the steady horizontal current in the metal pad. Important parameters in determining the stability are the magnitude of the horizontal current density, ACD and metal depth. It is shown that the vertical current has almost no effect.

### 2.2.4 Sneyd's horizontally infinite model

Besides the above effects, the interfacial instability can be affected by the external magnetic field due to distant current sources. Sneyd [72] analysed a plane horizontal poorly conducting layer (cryolite), sandwiched between two highly conducting semi-infinite layers, the lower one a fluid (liquid aluminium) and the upper solid (carbon anode). In the static state, he assumed the uniform electric current $\mathbf{J}$ as purely vertical,

$$\mathbf{J} = J_o \hat{\mathbf{z}}, \tag{2.2}$$

and the magnetic field $B_i$ as a linear function of position as follows:

$$B_i = B_{oi} + \alpha_{ij} x_j,$$

or

$$\mathbf{B}_i = \mathbf{B}_o + \mathbf{B}, \tag{2.3}$$

where $\mathbf{B}_o$ is a constant vector and $\alpha_{ij}$ a constant second-order tensor.

The first term is due to local currents, while the second term is due to remote (background) current sources. Using the above magnetic field, Sneyd calculated the Lorentz force. A dispersion relation at the interface is derived from the linearised equation of motion in the fluid layers. The eigenvalues are extracted to obtain the growth rate of the interface wave. His result shows that the stability of the interface

depends on the form of the magnetic field due to far current sources. Finally, Sneyd suggested the cell should be made as symmetrical as possible to minimise horizontal gradients in the far field. Lympany [39], [40] also found that the connection geometry in which the current is delivered and withdrawn from the cell has an important influence on the interface movement.

In spite of the above useful results, this model has the limitation that the analysis is two-dimensional and the lateral boundary condition is not considered.

### 2.2.5 Sneyd and Wang's normal mode analysis: resonance of standing waves

The normal mode method is a useful tool for analysing general systems. It is based on the idea of expressing variables as a linear combination of normal modes. Then the equations can be simplified by the orthogonal property of the normal modes. Sneyd and Wang [74] developed a normal mode analysis for a combination of gravity waves, while Urata analyses a single Fourier component wave. Sneyd and Wang derive a system of coupled ordinary differential equations for the time-development of the mode amplitudes. In order to determine the conditions for instability, growth rates are determined by computing the eigenvalues of an interaction matrix and an approximate method using only the three leading diagonals (see (2.6)) is developed to reduce the computation efforts.

The main advance in this analysis is that this model is three-dimensional and considers the vertical and lateral boundary conditions realistically. Also the main physical parameters such as velocity, force, current and magnetic fields can be analytically expressed in terms of Fourier components. Thus, this approach is very practical for real application.

As will be explained in detail for the general normal mode analysis in Chapter 5, the interface displacement $\eta(x, y)$ can be expanded in terms of the eigenfunctions $E_n$ as follows:

$$\eta(x, y, t) = \sum_{n=1}^{\infty} \eta_n(t) E_n(x, y), \tag{2.4}$$

where

$$E_n(x,y) = \cos\frac{n_x \pi x}{a} \cos\frac{n_y \pi y}{b},$$

which satisfies lateral boundary conditions. The subscripts $n$, $n_x$ and $n_y$ are integers in the above equations. The coefficients $\eta_n(t)$ are functions of time describing the evolution of the wave. They should be small, as we make usual small-amplitude linearising assumption.

The linearised equation of motion in each layer is written as:

$$\rho\frac{\partial \mathbf{u}}{\partial t} = -\nabla p - \rho g\hat{\mathbf{z}} + \mathbf{f}_M, \tag{2.5}$$

where $p$ is the perturbation pressure and $\mathbf{f}_M$ denotes the perturbed Lorentz force.

Wave evolution equations for the interface coefficients $\eta_k(t)$ are obtained by taking the inner product of the above equation with irrotational gravity-wave modes $\nabla\phi_k$ in each layer, yielding the following coupled system of evolution equations:

$$\ddot{\eta}_k + \Omega_k^2\left(\eta_k - \epsilon\sum_{n=0}^{\infty}\gamma_{kn}\eta_n(t)\right) = 0, \tag{2.6}$$

where the gravitational frequency $\Omega_k$ is a constant and the dimensionless parameter $\epsilon$ is a measure of the relative importance of magnetic and gravity restoring forces to interfacial waves. The growth rates of the interface displacement coefficients $\eta_k$ are determined by the above wave evolution equations. The magnetic interaction coefficients $\gamma_{kn}$ represent mode coupling arising from the Lorentz force perturbation.

Sneyd & Wang [74] showed that a resonance of the neighbouring waves can occur when two different modes have similar frequencies. For two modes with approximately equal frequencies, the stability can be analysed in term of the 2x2 interaction matrix for two such modes. Their analysis shows how the cell dimensions affect the instability by changing the natural frequencies of the standing waves. The magnetic term is considered to be small compared with the gravity term. The waves consist essentially of a combination of gravity modes weakly coupled by electromagnetic effects. The heterogeneous magnetic field links evolution of different modes, which may thereby destabilize one another. If any two modes have similar frequencies they may interact resonantly to destabilize the cell at quite small electrical current density, the magnetic restoring force established by one mode feeding energy into the other. The combination of two modes can be more unstable than either mode individually. The cell dimension and the vertical magnetic field are the most important

factors in avoiding this interaction between the neighbouring modes in optimum cell designs. The equation quoted on this section is of exactly the same form as Sneyd and Wang's.

### 2.2.6 Bojarevics and Romerio's work

Bojarevics & Romerio [13] generalised Sele's criterion [69], which depends on the aspect ratio of cell. They derive equations very similar to Sneyd and Wang's work in the previous section.

The governing equations couple hydrodynamic variables and electric current. Modified gravitational waves were obtained, which can be either purely oscillating or exponentially growing. For approximated solutions, having in mind the situation in which two neighbouring frequencies are very close and the natural frequency is located between them, the eigenvalues of the two interacting modes were deduced from the wave equations. Bojarevics and Romerio studied the effect of cell dimensions, electric current density and magnetic field with the criterion.

They established a coupled set of interface equations of the form

$$\ddot{\mathbf{x}} + \boldsymbol{\Omega}\mathbf{x} = \epsilon \mathbf{K}\mathbf{x},$$

where $\mathbf{x}$ is a column vector which represents the amplitude of the gravitational modes. The gravitational wave matrix $\boldsymbol{\Omega}$ is diagonal with elements equal to the square of the gravitational frequencies and the $\mathbf{K}$ is the interaction matrix which arises from the Lorentz force. The scalar $\epsilon$ is the ratio of the Lorentz force to inertia. The interaction matrix $\mathbf{K}$ is determined by calculating the redistribution of current caused by one gravitational mode. Normally, there is a critical value of $\epsilon$ at which complex eigenvalues appear. The dominant contribution to the perturbed Lorentz force arises from the interaction between a horizontal current in the aluminium and the vertical component of the background magnetic field $B_z$. Their results show that standing waves are predicted to go unstable once $B_z$ exceeds some critical value. On the other hand, travelling waves are unstable whenever there is a horizontal gradient in $B_z$, provided that friction is ignored.

### 2.2.7 Davidson & Lindsay's work

Recently, Davidson & Lindsay [17] introduced a simplified mechanical analogy to find a stability threshold in aluminium reduction cells. They considered a compound pendulum as shown in Figure 2.1. It consists of a large flat aluminium plate attached to an adjacent, parallel surface by a light, rigid strut. The strut is pivoted at its top end so that the plate is free to swing about two horizontal axes, x and y. The density of the cryolite ($\rho_c$) and the horizontal magnetic field ($B_x$ and $B_y$) are ignored in this analysis.

Taking moments about the pivot, two equations of motion for the pendulum are obtained, which include the coupling terms associated with the Lorentz forces. Finally, they derive an instability equation as

$$\frac{2j_oB_z}{\rho_aH} = |\omega_x^2 - \omega_y^2|,$$

where $\omega$ is the conventional gravitational frequencies of the pendulum.

The behaviour of $\omega^2$ can be explained in a complex plane. As $j_oB_z$ is increased the two natural frequencies converge on the real axis. At a critical value of $j_oB_z$, the two frequencies meet and then move off into the complex plane. Thus, the result shows that the sensitivity of the pendulum to the destabilizing influence of $j_oB_z$ depends on the initial separation of the gravitational frequencies, which was established by Sneyd & Wang and Bojarevics & Romerio.

Also Davidson & Lindsay derived a sufficient condition for the interface stability from the MHD coupled equations in the previous section

$$(\mathbf{\Omega}_g - \epsilon\mathbf{K})\mathbf{x} = \omega^2\mathbf{x},$$

without extracting the eigenvalues. Using Gershgorin's theorem [34] on the eigenvalues of the interface wave equations, they produced a new instability criterion for both travelling and standing waves. Gershgorin's theorem links each eigenvalues to one of the diagonal elements of the matrix $\mathbf{\Omega_g}$ and places a bound on the separation of the natural frequencies $\omega_i^2$ and the gravitational frequencies $\omega_{gi}^2$ in the complex plane:

$$|\omega_i^2 - \omega_{gi}^2| \leq \epsilon \sum_{k=1}^{\infty} |K_{ik}|,$$

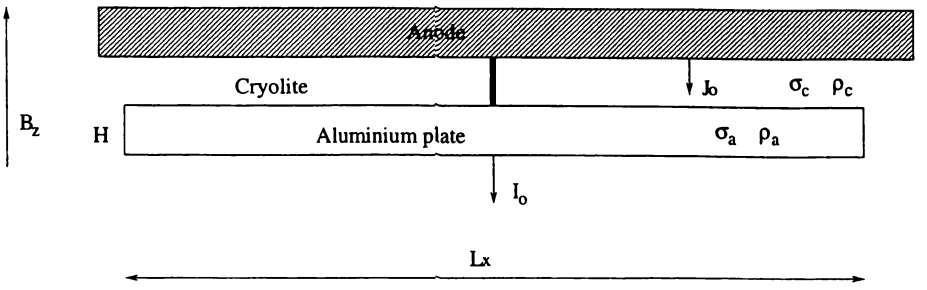


Figure 2.1: A compound pendulum.

where $K_{ik}$ is the element of the interaction matrix $\mathbf{K}$. This allows us to place a lower bound on the critical value of the background magnetic field at which an instability first appears. Finally, for the closest gravitational frequencies $\omega_{gi}^2$ and $\omega_{gj}^2$, a sufficient condition for stability is expressed as:

$$|\omega_{gi}^2 - \omega_{gj}^2| > \epsilon(\sum_{k=1}^{\infty} |K_{ik}| + \sum_{k=1}^{\infty} |K_{jk}|)$$

or

$$\frac{|\omega_{gi}^2 - \omega_{gj}^2|}{\sum_{p=1}^{\infty} |K_{ip}| + \sum_{p=1}^{\infty} |K_{jp}|} > \frac{J_o B_z}{\rho_a h_c + \rho_c h_a}.$$

It is remarkable that we can obtain the instability condition directly without solving the governing equations of motion. Also we do not need to solve the eigenvalue problem, while Sneyd & Wang and Bojarevics & Romerio give simple approximate methods to solve it. Above all, the new equation is valid regardless of the existence or form of boundaries.

When an infinitely long channel is considered, the travelling waves may become unstable even with a uniform, vertical magnetic field. This result is quite different to previous works by Sneyd [72], Moreau & Ziegler [52] and Pigny & Moreau [57] which require more complex magnetic fields to become unstable. However, in any case, as the influence of the lateral boundaries of the cell is ignored, these travelling wave models have their limit in real applications.

Davidson & Lindsay also derived a sufficient condition for the stability of standing waves in a finite domain. In case of rectangular lateral boundaries, the model leads to the standing waves of Sneyd & Wang's work. According to this instability condition, it is frequently not the pair of modes with closest gravitational frequencies which first become unstable. The largest growth rate is not necessarily observed in the first unstable mode-pair. It is interesting to note that relatively few mode-pairs are

coupled to be destabilised geometrically in rectangular cells and the uncoupled pairs cannot become unstable.

Finally, we can conclude that Bojarevics & Romerio, Sneyd & Wang and Davidson & Lindsay, in spite of the slight differences in their approaches, all of them tried to produce an instability condition by observing the eigenvalues of the MHD coupled equations which represent the growth rate of the interface waves.

### 2.2.8 Ziegler's steady velocity analysis

Ziegler [85] established a purely hydrodynamic instability model without considering the electromagnetic interaction effect between the interface wave and the magnetic field. Using Fourier-Galerkin spatial discretization and the finite difference discretization in time, the evolution equations are solved with basis functions, which are chosen to satisfy the vertical and lateral boundary conditions for the interface and horizontal velocity field. He assumed the same steady velocity in both liquid layers and showed that the interface becomes unstable above a critical value of the steady velocity.

Ziegler formulated the perturbation equations for the interfacial instability using shallow-water theory. The shallow-water approximation assumes the liquid layer thickness is quite small compared to a typical wavelength. This method is similar to that used by Urata [79].

In order to represent the velocity field Ziegler used a stream function of the form of Fourier components in phase $p$:

$$\psi_p = \sum_{i=0}^{I} \sum_{j=0}^{J} S_{pij} \sin X_i \sin Y_j. \tag{2.7}$$

However, we shall show later that a superposition of such modes cannot represent a steady flow. Thus only a single Fourier component should be allowed if $\psi_p$ is to represent a steady flow. In any case Ziegler used the stream function with a single Fourier component in his numerical simulations.

The final set of equations is solved for the first 8 modes in each horizontal direction, and is integrated in time using Adams-Moulton method. A trial velocity is input and

the program is run until the perturbation energy is either 100 times greater or 100 times less than the initial energy or if the simulated time exceeds 1.5 hours without either of these occurring. If the configuration is stable, the velocity is increased and the process repeated to find the critical velocity.

Both fluids are assumed to have the same steady velocity in this calculation. The results determined from this hydrodynamic analysis for the four flow configurations examined are shown below. Figure 5.4 shows a typical steady flow configuration (2,1) used in Ziegler's calculation.

| Flow configuration | Modes | Critical velocity (m/sec) |
|---|---|---|
| (1,1) | $8 \times 8$ | 0.43 |
| (1,2) | $6 \times 6$ | 0.28 |
| (2,1) | $6 \times 6$ | 0.16 |
| (2,2) | $6 \times 6$ | 0.17 |

Generally speaking, higher steady velocities and more complex steady flow patterns make the system more unstable, although the dependence is not linear. The velocity at which the interface becomes unstable is of the same order as that measured in industrial cells.

The effect of drag parameter $\alpha$ on critical velocity is calculated with the steady flow configuration (2,1) as follows:

| Drag Parameter $\alpha$ | Critical Velocity (m/sec) |
|---|---|
| 0.5 | 0.11 |
| 1.0 | 0.17 |
| 2.0 | 0.33 |

The ACD is one of the most important factors for cell operation. Figure 2.2 shows the critical velocity for various values of the ACD. As the ACD is increased, the system becomes less stable. This comes from the simple fact that the damping force will be decreased as the ACD is increased since the Moreau damping coefficient has been adopted (see the next section). His result on the ACD is contradictory to the conventional knowledge and the real measurements. We discuss this point in more detail in Chapter 6.

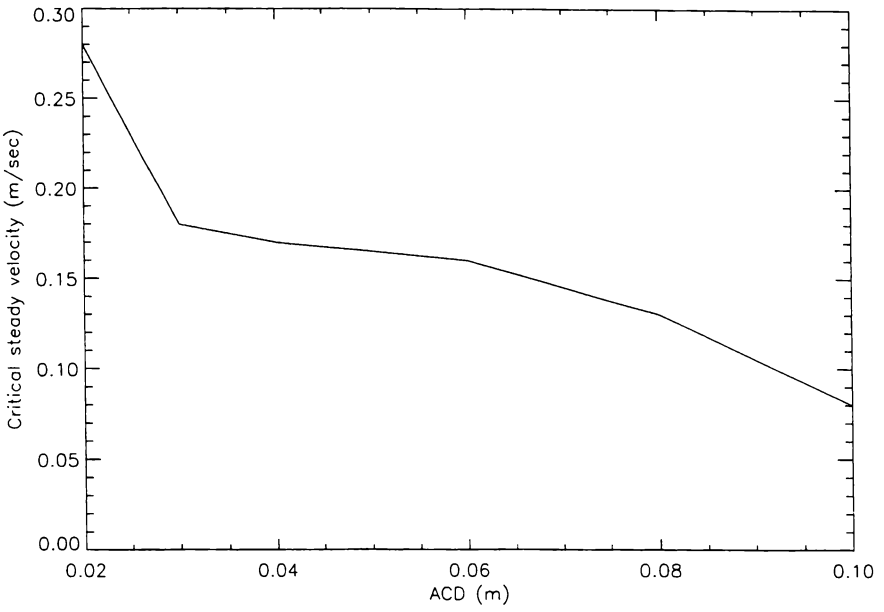


Figure 2.2: Effect of ACD on the critical steady velocity by Ziegler for the basic flow configuration (2,2).

### 2.2.9 Damping

In this section, we review simple drag models which incorporate both the drag force, which is associated with turbulent viscosity and the induced current density, due to the external magnetic fields. Normally, the threshold for the instability predicted from many theories is much lower than that observed in real cells, because damping has been neglected.

Moreau [51] introduced a simplified model by considering the damping due to the no-slip condition on the solid boundaries. This model produced convincing results compared with those from a two-dimensional hydrodynamic model based on the Navier-Stokes equations. Later, this model was incorporated into the interfacial instability theory for infinite models by Sneyd [73] and Pigny & Moreau [57] allowing steady flows in both layers.

Moreau's model was mainly concerned with the vertical momentum flux and the friction on the interface. This was estimated by analysing orders of magnitude in the Navier-Stokes equation with a magnetic body force:

$$\rho\left(\mathbf{U}\cdot\nabla\right)\mathbf{U} = -\nabla P + \mathbf{J}\times\mathbf{B} - \frac{\mathbf{T}}{H} + \frac{\partial}{\partial x_i}\left(\eta_e\frac{\partial}{\partial x_i}\mathbf{U}\right), \tag{2.8}$$

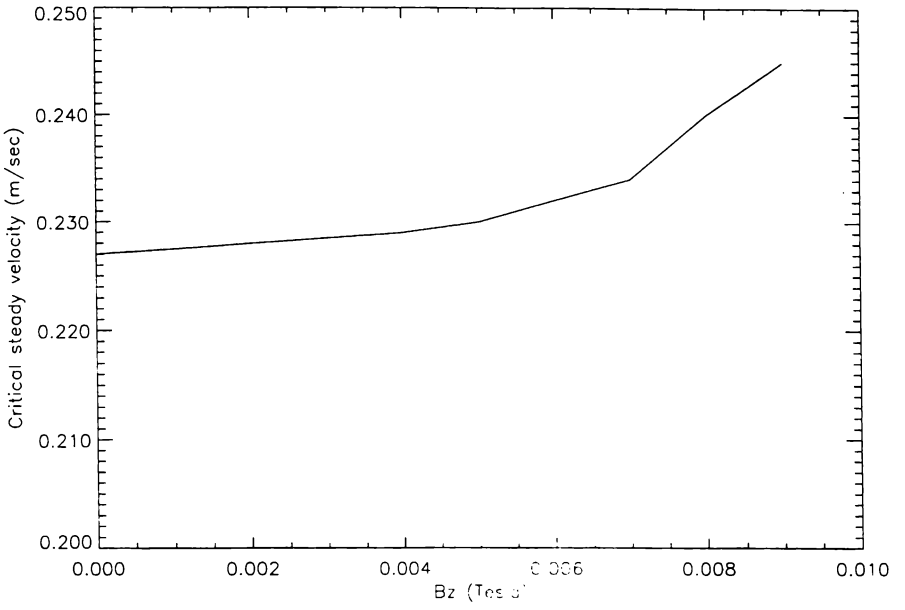


Figure 2.3: Effect of Wang's model of magnetic damping on the critical velocity in a reduction cell when $\beta = 0.5\sigma^a = 2.5 \times 10^6$ is assumed, where cell length a=7.7m, width b=3.3m, metal depth $h_a$=0.2m and ACD=0.04m.

$$\nabla \cdot \mathbf{U} = 0. \tag{2.9}$$

where $\mathbf{U}$ stands for the velocity, $P$ for the pressure and $\eta_e$ for the effective viscosity associated with two-dimensional motion. The term $\frac{\mathbf{T}}{H}$ represents the drag force induced from the no-slip condition at the top and bottom of the fluid layer. $H$ is the fluid layer depth and $\mathbf{T}$ is a drag force. Moreau showed that the force balance of the system can be achieved only between the magnetic force, the pressure gradient and the drag force, while other terms are relatively small.

Using a constant drag coefficient $k$, he assumed an approximately linear relationship between the drag force $\mathbf{T}$ and the velocity $\mathbf{U}$ as follows:

$$\mathbf{T} = k\mathbf{U}. \tag{2.10}$$

To consider the damping due to the induced current density, Wang [83] modified Moreau's linear damping model by assuming a drag coefficient dependent on the magnetic field as well as the thickness of each layer:

$$k = \beta B_o^2 + \frac{\alpha}{h}. \tag{2.11}$$

The value of coefficient $\alpha$ suggested by Ziegler [85]

$$\alpha = 1.0 \text{ kg}/\left(m^2 \sec\right), \tag{2.12}$$

is used while we expect $\beta$ to be of the same order as the electrical conductivity $\sigma$. $\alpha = 1.0$ is calculated with values of $V_x = 0.15$ m/s and $L = 3$ m respectively, from the following formula by Bird [11] for turbulent drag on a flat plate:

$$\alpha = 0.037 \rho V_x^2 \left(\frac{L V_x \rho}{\mu}\right)^{-1/5}$$

Figure 2.3 shows Wang's result. The damping effect of induced current is increased greatly when $B_z$ is greater than 0.008 Tesla. We will discuss this result further in Chapter 7.

In this chapter, we reviewed and discussed previous interfacial instability theories which are related with our research. Based on this review, our model will be established, simulated and compared with other models in Chapter 5 and 6.

# Chapter 3

# Basic physics of interfacial instability

Interfacial instability can be caused by the current perturbation or the KH instability. As reviewed in Chapter 2, the steady velocity fields and the magnetic fields are the crucial parameters in the analysis. These effects can be predicted by the MHD equations. In this chapter, we review the basic MHD equations and linearised perturbation equations (For further details, see [49], [22], [27], [36], [50] and [26]).

## 3.1 Basic MHD equations

### 3.1.1 Navier-Stokes equations

The superscript $a$ and $c$ will denote the aluminium and the cryolite layer respectively. This notation is used in this thesis, unless specified otherwise. The Navier-Stokes equations are commonly used to describe the flow. As we assume that the liquids are incompressible and inviscid, we have the following form of the Navier-Stokes equations,

$$\rho\dot{\mathbf{U}} + \rho\left(\mathbf{U}\cdot\nabla\right)\mathbf{U} + \nabla P - \mathbf{F} = 0, \tag{3.1}$$

and the continuity equation,

$$\nabla\cdot\mathbf{U} = 0, \tag{3.2}$$

where $\rho$ = the mass density, $\mathbf{U}$ = the velocity field, $P$ = the pressure and $\mathbf{F}$ = the body force.

The body force includes gravity and the electromagnetic forces:

$$\mathbf{F} = -\rho g \mathbf{z} + \mathbf{J} \times \mathbf{B}, \tag{3.3}$$

where $g$ = gravitational acceleration, $\mathbf{J}$ = the current field and $\mathbf{B}$ = the magnetic field.

As the normal velocities on liquid/solid boundaries are zero, the boundary condition for the velocity field is written as:

$$\mathbf{U} \cdot \hat{\mathbf{n}} = 0, \tag{3.4}$$

where $\hat{\mathbf{n}}$ is an unit normal vector to the liquid and solid boundaries.

Continuity of normal velocity $U_n$ and pressure $P$ at the aluminum/cryolite interface implies

$$P^a = P^c,$$

$$U_n^a = U_n^c = 0. \tag{3.5}$$

The vorticity equation can be obtained by taking the curl of the equation (3.1):

$$\rho \dot{\mathbf{\Omega}} + \rho \left(\mathbf{U} \cdot \nabla\right) \mathbf{\Omega} - \rho \left(\mathbf{\Omega} \cdot \nabla\right) \mathbf{U} - \nabla \times \mathbf{F} = 0, \tag{3.6}$$

where the vorticity $\mathbf{\Omega} = \nabla \times \mathbf{U}$.

### 3.1.2 Maxwell's equations

Since the materials in the cell interior are not ferromagnetic, Maxwell's equations can be written as follows:

$$\nabla \cdot \mathbf{B} = 0, \tag{3.7}$$

$$\nabla \times \mathbf{E} = -\frac{\partial \mathbf{B}}{\partial t}, \tag{3.8}$$

$$\nabla \cdot \mathbf{D} = q, \tag{3.9}$$

$$\nabla \times \mathbf{H} = \mathbf{J} + \frac{\partial \mathbf{D}}{\partial t}, \tag{3.10}$$

where $\mathbf{E}$ = the electric field, $\mathbf{D}$ = the electric displacement, $\mathbf{H}$ = the magnetic induction and $q$ = the charge density. We also have two other relations by virtue of the definition of the $\mathbf{D}$ and the $\mathbf{H}$,

$$\mathbf{D} = \epsilon_o \mathbf{E}, \tag{3.11}$$

$$\mathbf{H} = \frac{\mathbf{B}}{\mu}, \tag{3.12}$$

where the free space dielectric constant $\epsilon_o$ and the permeability $\mu$ take the following values in S.I.units,

$$\begin{aligned} \epsilon_o &= 8.8552 \times 10^{-2}\ \mathrm{Fm}^{-1}, \\ \mu &= 4\pi \times 10^{-7}\ \mathrm{Hm}^{-1}. \end{aligned}$$

Ohm's law is used to complete the boundary value problem,

$$\mathbf{J} = \sigma \mathbf{E}, \tag{3.13}$$

where the electric conductivity takes the following values:

$$\begin{aligned} \sigma^a &= 5 \times 10^6\ \Omega^{-1}\mathrm{m}^{-1}, \\ \sigma^c &= 10^{-2}\ \Omega^{-1}\mathrm{m}^{-1}. \end{aligned}$$

If we make the usual MHD approximation of neglecting the displacement current $\partial \mathbf{D}/\partial t$ [33], (3.10) becomes

$$\nabla \times \mathbf{H} = \mathbf{J}. \tag{3.14}$$

Using Ohm's law, we can write

$$\mathbf{J} = \sigma \left( \mathbf{E} + \mathbf{U} \times \mathbf{B} \right). \tag{3.15}$$

The second term in the above equation is known as the induced current density and represents current generated by fluid motion. We will discuss further the induced current in Chapter 7.

Thus, we have the electromagnetic equations as follows:

$$\nabla \cdot \mathbf{B} = 0,$$

$$\nabla \times \mathbf{B} = \mu \mathbf{J},$$

$$\nabla \times (\mathbf{J} - \sigma \mathbf{U} \times \mathbf{B}) = -\sigma \frac{\partial \mathbf{B}}{\partial t}. \tag{3.16}$$

By eliminating $\mathbf{J}$ from the above equations, we have finally

$$\nabla \cdot \mathbf{B} = 0,$$

$$\nabla \times \left( \frac{1}{\mu} \nabla \times \mathbf{B} - \sigma \mathbf{U} \times \mathbf{B} \right) = -\sigma \frac{\partial \mathbf{B}}{\partial t}. \tag{3.17}$$

The lateral boundaries for both layers in a cell are made from the frozen cryolite which is an electrical insulator, so the normal component of the electric currents on these boundaries is assumed to be zero

$$\left( \frac{1}{\mu} \nabla \times \mathbf{B} \right) \cdot \hat{\mathbf{n}} = 0.$$

On the top and the bottom of the cell where the currents are distributed through the anode, we have

$$\begin{aligned} \left( \frac{1}{\mu} \nabla \times \mathbf{B} \right) \cdot \mathbf{z} &= J^*_{top}(x, y), \\ \left( -\frac{1}{\mu} \nabla \times \mathbf{B} \right) \cdot \mathbf{z} &= J^*_{bottom}(x, y). \end{aligned} \tag{3.18}$$

where $J^*_{top}$ and $J^*_{bottom}$ represents distributions on the anode/cryolite and aluminium/ cathode interfaces. They are normally unknown and can be solved for in conjunction with the internal fields.

### 3.1.3 The Lorentz force

The magnetic fields can be expressed in terms of the current density, using the Biot-Savart law

$$\mathbf{B} = \frac{\mu}{4\pi} \int \frac{\mathbf{J} \times \mathbf{r}}{r^3} dv, \tag{3.19}$$

where $\mathbf{r}$ is the spatial coordinate vector. The current density $\mathbf{J}$ can be obtained by solving Laplace's equation for the current potential $\phi$ with appropriate boundary conditions. Also it is possible to determine $\mathbf{J}$ from potential theory only if we can assume that $\mathbf{J}$ is slowly-varying, so that $\dot{\mathbf{B}} \approx 0$ and $\nabla \times \mathbf{J} \approx 0$ [72].

Using the conservation of the current $\nabla \cdot \mathbf{J} = 0$, we have another equation as follows:

$$\begin{aligned} \nabla \cdot \nabla \phi &= 0 \\ \nabla^2 \phi &= 0. \end{aligned} \tag{3.20}$$

As defined in the previous section, the Lorentz force is written as:

$$\begin{aligned} \mathbf{F}_L &= \mathbf{J} \times \mathbf{B} && (3.21) \\ &= \frac{1}{\mu} (\nabla \times \mathbf{B}) \times \mathbf{B}. && (3.22) \end{aligned}$$

If we separate the magnetic field into internal $\mathbf{B}_{int}$ and external (background) part $\mathbf{B}_{ext}$ [74], we have

$$\mathbf{F}_L = \frac{1}{\mu} [\nabla \times (\mathbf{B}_{int} + \mathbf{B}_{ext})] \times (\mathbf{B}_{int} + \mathbf{B}_{ext}) . \tag{3.23}$$

or

$$\mathbf{F}_L = \frac{1}{\mu} [\nabla \times (\mathbf{B}_{int})] \times (\mathbf{B}_{int} + \mathbf{B}_{ext}) , \tag{3.24}$$

as $\nabla \times \mathbf{B}_{ext} = 0$ in the fluid. The antisymmetric term $\mathbf{B}_{int}$ represents the internal part $\mathbf{B}$ due to local current, while the symmetric term $\mathbf{B}_{ext}$ represents the external field due to remote current sources, such as those in the bus bar, which is often known by empirical measurements.

## 3.2 Linearised perturbation equations

When we assume a small perturbation from an equilibrium state on the aluminium/ cryolite interface, we can decompose the system variables as follows:

$$\begin{aligned} \mathbf{U}' &= \mathbf{U} + \mathbf{u}, \\ P' &= P + p, \\ \mathbf{J}' &= \mathbf{J} + \mathbf{j}, \\ \mathbf{B}' &= \mathbf{B} + \mathbf{b}, && (3.25) \end{aligned}$$

where capital letters represent the steady state and lower case letters the small perturbation. Only the first order perturbations will be considered in this thesis.

Substituting the above equations into the Navier-Stokes equations, to leading order we have

$$\rho \dot{\mathbf{u}} + \rho (\mathbf{U} \cdot \nabla) \mathbf{u} + \rho (\mathbf{u} \cdot \nabla) \mathbf{U} + \nabla p - \mathbf{f} = 0, \tag{3.26}$$

$$\nabla \cdot \mathbf{u} = 0, \tag{3.27}$$

where

$$\begin{aligned} \mathbf{f} &= \mathbf{j} \times \mathbf{B} + \mathbf{J} \times \mathbf{b} \\ &= (\frac{1}{\mu} \nabla \times \mathbf{b}) \times \mathbf{B} + \mathbf{J} \times \mathbf{b}. \end{aligned} \tag{3.28}$$

On solid boundaries, the normal component of the velocity field is zero,

$$u_n = \mathbf{u} \cdot \hat{\mathbf{n}} = 0. \tag{3.29}$$

On the aluminium/cryolite interface, we have

$$\frac{D}{Dt}(\eta - z) = 0$$

or

$$\begin{aligned} u_z &= \frac{D}{Dt}\eta \\ &= \dot{\eta} + \mathbf{U} \cdot \nabla \eta. \end{aligned} \tag{3.30}$$

By the pressure continuity on the interface, we have

$$P^a + p^a = P^c + p^c. \tag{3.31}$$

Similarly, we can write the magnetic field perturbation as follows:

$$\nabla \cdot \mathbf{b} = 0.$$

$$\nabla \times \left( \frac{1}{\sigma \mu} \nabla \times \mathbf{b} - \mathbf{U} \times \mathbf{b} - \mathbf{u} \times \mathbf{B}_{int} \right) = \nabla \times (\mathbf{u} \times \mathbf{B}_{ext}) - \frac{\partial \mathbf{b}}{\partial t}. \tag{3.32}$$

## 3.3 System analysis

A spectral analysis is widely used to analyse the stability of a linear system. Mathematically, the physical variables such as the velocity, the pressure and the surface wave displacement can be assumed proportional to

$$e^{i(\mathbf{k} \cdot \mathbf{x} - \omega t)}.$$

The wave behaviour is determined by the dispersion relation between the wave number vector $\mathbf{k}$ and the angular frequency $\omega$ of the system. All modes can be examined at a time by this method.

Another method is a time evolution simulation. This is often an inevitable option for the analysis of the nonlinear system. We shall adopt this method to calculate the critical steady velocity in this thesis, as our equations are dependent on time with the transient adjustment of the basic steady velocity.

# Chapter 4

# Two-dimensional flows in rectangular containers

In this chapter, we will discuss the stability of the two-dimensional flows with closed streamlines in rectangular containers. It is interesting to discuss the stability of single layer, before we investigate the interfacial instability between two liquid layers in aluminium reduction cells. This study is to find whether single layer flows are stable themselves without any interfacial mechanism or not. First, two-dimensional steady laminar flows and the representation of stream functions for basic steady flows will be discussed. Then Arnol'd's stability theorem will be discussed. The global stability criteria provided by this theorem will give a general picture about the disturbances and the stability. A normal mode analysis is introduced to investigate an unsteady evolution of flow when two different modes are initially present.

## 4.1 Two-dimensional steady laminar flows with closed streamlines

First we discuss the features of two-dimensional steady laminar flows with closed streamlines consisting of one or several eddies. We assume steady laminar motion of large Reynolds number - i.e. that viscous forces are small compared with pressure forces nearly everywhere in the cell. It is assumed that the Reynolds number is large

enough for the thickness of the associated viscous layers to be small compared with the linear dimensions of the region of fluid under consideration.

The equations governing the steady laminar motion of a uniform incompressible fluid are obtained from the continuity equation and the Navier-Stokes equation as follows [8]:

$$\nabla \cdot \mathbf{u} = 0, \tag{4.1}$$

$$\begin{aligned} \mathbf{u} \times \omega - \nabla \left( \frac{p}{\rho} + \frac{q^2}{2} \right) + \nu \nabla \times \omega &= \frac{\partial \mathbf{u}}{\partial t} \\ &= 0, \end{aligned} \tag{4.2}$$

where the vorticity term $\omega$ and the scalar velocity term $q$ are defined by:

$$\omega = \nabla \times \mathbf{u}, \tag{4.3}$$

$$q = |\,\mathbf{u}\,|\,. \tag{4.4}$$

When the Reynolds number of the motion is large, viscous forces are small everywhere except in the neighbourhood of certain singular surface and the equation (4.2) reduces approximately to

$$\mathbf{u} \times \omega = \nabla H, \tag{4.5}$$

where $H$ is the local total head in the fluid,

$$H = \frac{p}{\rho} + \frac{q^2}{2}. \tag{4.6}$$

The local total head $H$ is constant over stream-vortex surfaces or 'Bernoulli surfaces', each such surface containing the local vectors $\mathbf{u}$ and $\omega$ in its tangent plane everywhere and being swept out by a vortex line. However, when the viscosity $\nu \neq 0$ the stream-vortex surfaces will not exist because $\mathbf{u} \times \omega$ is then not necessarily parallel everywhere to the gradient of some scalar function.

In order to understand the effect of viscosity, no matter how small the value of $\nu$ may be, we take the line integral of equation (4.2) around a closed contour with line element $d\mathbf{l}$,

$$\oint (\mathbf{u} \times \omega) \cdot d\mathbf{l} - \oint d\mathbf{l} \cdot \nabla H - \nu \oint (\nabla \times \omega) \cdot d\mathbf{l} = 0. \tag{4.7}$$

The second term on the left-hand side vanishes since $H$ is a single-valued function of position. We can make the first term on the left-hand side zero by choosing the

closed contour to coincide with a streamline, of which a line element will be denoted by $d\mathbf{s}$. Thus we have the exact integral condition

$$\oint (\nabla \times \boldsymbol{\omega}) \cdot d\mathbf{s} = 0, \tag{4.8}$$

to be satisfied for every closed streamline.

When the flow is two-dimensional, we can introduce the stream function $\psi$,and use the orthogonal curvilinear coordinates ($\psi$,$\xi$), the lines $\xi$ = *constant* being everywhere normal to the streamlines. The displacements corresponding to increments in $\psi$ and $\xi$ are $d\psi/q$ and $hd\xi$, where $h$ is an unknown function of $\psi$ and $\xi$. Now the inviscid flow equation (4.5) can be written as:

$$\omega(\psi) = \frac{dH(\psi)}{d\psi}. \tag{4.9}$$

The above equation is approximately valid everywhere when the Reynolds number of the motion is large.

When evaluating the integral in (4.8) for streamlines lying in the region of small viscous forces, we can make use of the approximation (4.5) whence $\nabla \times \boldsymbol{\omega}$ becomes a vector parallel to the local streamline and (4.8) takes the form

$$\frac{d\omega}{d\psi} \oint q ds = 0. \tag{4.10}$$

Thus we have

$$\frac{d\omega}{d\psi} = 0,$$

or

$$\omega(\psi) = \frac{dH(\psi)}{d\psi} = \text{constant}, \tag{4.11}$$

everywhere in a connected region of small viscous forces [8].

The above simple equation contains a significant physical meaning. In steady flows, the net viscous diffusion of vorticity across a closed streamline must be zero. This is possible only if vorticity $\omega$ is approximately constant across streamlines, which is well-known as the Prandtl-Batchelor theorem [9].

Now we consider a stream function for steady flows. Ziegler [85] used a combination of Fourier components as a stream function $\Psi$ for the basic steady flow in his linearised equations as follows:

$$\psi = \sum_{n=1}^{K} U_n H_n(x, y),$$

where the eigenfunctions

$$H_n = \sin\frac{n_x \pi x}{a} \sin\frac{n_y \pi y}{b}$$

satisfy the following equations:

$$\nabla^2 H_n + \lambda_n^2 H_n = 0, \tag{4.12}$$

$$H_n = 0 \text{ on lateral boundaries.} \tag{4.13}$$

However, the above expression for the stream function does not in general represent a steady flow. We must first check the physical and mathematical features of the basic flow.

When the flow in the cell is steady, the vorticity must be constant along closed stream lines. Thus we can express this mathematically as follows:

$$\begin{aligned} \frac{D}{Dt}\omega &\equiv \frac{\partial}{\partial t}\omega + \mathbf{u}\cdot\nabla\omega \\ &= 0. \end{aligned} \tag{4.14}$$

where the first term is zero for steady flow,

$$\frac{\partial}{\partial t}\omega = 0. \tag{4.15}$$

Thus the second term of the above equation must be zero,

$$\mathbf{u}\cdot\nabla\omega = 0. \tag{4.16}$$

As the velocity $\mathbf{u}$ can be expressed in terms of stream function as follows:

$$\mathbf{u} = \nabla\psi \times \hat{\mathbf{z}},$$

we can obtain the relationship between $\Psi$ and $\omega$ in two dimensional flow as follows:

$$\begin{aligned} \mathbf{u}\cdot\nabla\omega &= (\nabla\psi\times\hat{\mathbf{z}})\cdot\nabla\omega \\ &= -[\psi,\omega] \\ &= 0, \end{aligned} \tag{4.17}$$

where the Poisson bracket $[\psi,\omega]$ denotes

$$[\psi,\omega] = \begin{vmatrix} \partial_x\psi & \partial_y\psi \\ \partial_x\omega & \partial_y\omega \end{vmatrix}.$$

The steady-flow condition $[\psi, \omega] = 0$ is equivalent to the condition that $\psi$ is a function of $\omega$,

$$\psi = F(\omega).$$

For example, when the stream function has a single Fourier component,

$$\psi = U_1 H_1(x, y), \tag{4.18}$$

it is clear that this represents a steady flow. Indeed

$$\omega = -\nabla^2 U_1 H_1 = \lambda_1^2 U_1 H_1 = \lambda_1^2 \psi,$$

so $\omega$ and $\psi$ are functionally related. However, when we consider a stream function with two Fourier components,

$$\psi = U_1 H_1(x, y) + U_2 H_2(x, y), \qquad \omega = \lambda_1^2 U_1 H_1 + \lambda_2^2 U_2 H_2 \tag{4.19}$$

$\psi$ and $\omega$ are not functionally related unless $\lambda_1 = \lambda_2$. Thus a stream function with several Fourier components will not generally represent a steady flow. Ziegler neglected this point in some of his numerical applications.

## 4.2 Global stability criteria in rectangular containers

In the previous section, we summarised the approximate relationship between the vorticity and the streamline in two-dimensional high Reynolds number steady laminar flow. The linear stability of flows of this type to two-dimensional disturbances will be discussed by Arnol'd's stability theorems in this section.

### 4.2.1 Arnol'd's stability theorems

When the two-dimensional steady flow $\psi(x, y)$ is perturbed by an unsteady disturbance $\phi(x, y, t)$ the stream function $\Psi(x, y, t)$ [45] may be represented by

$$\Psi(x, y, t) = \psi(x, y) + \epsilon\phi(x, y, t), \tag{4.20}$$

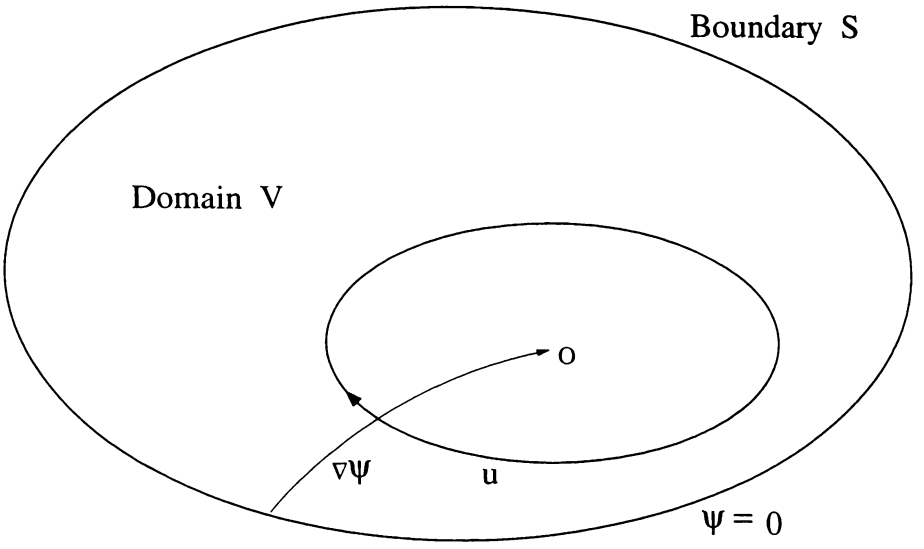


Figure 4.1: A topologically simple streamline pattern.

where $\epsilon$ is some small parameter and $\phi(x,y,t)$ and $\Psi(x,y,t)$ vanish on the boundary $S$. Because the vorticity is constant on a fluid particle

$$\begin{aligned} \frac{D\omega}{Dt} &= \frac{D}{Dt}\left[-\nabla^2\Psi(x,y,t)\right] \\ &= 0. \end{aligned} \tag{4.21}$$

Arnol'd [7], [6] observed that for any such flow, the functional

$$A(\Psi) = \int_V \left[\frac{1}{2}|\nabla\Psi|^2 - C\left(-\nabla^2\Psi\right)\right] dV, \tag{4.22}$$

is also conserved by the flow for any function $C$, i.e.

$$\frac{d}{dt}A(\Psi) = 0. \tag{4.23}$$

This follows from the individual conservation laws for kinetic energy and vorticity. To first order in $\epsilon$ the functional $A(\Psi)$ will be written as follows:

$$A(\Psi) = A(\psi) + \epsilon \int_V \left[\nabla\psi\cdot\nabla\phi + \nabla^2\phi C'(-\nabla^2\psi)\right] dV. \tag{4.24}$$

Now, by the relation

$$\nabla\psi\cdot\nabla\phi = \nabla\cdot(\psi\nabla\phi) - \psi\nabla^2\phi,$$

and by the divergence theorem

$$\int_V \nabla\cdot(\psi\nabla\phi)dV = \int_S \psi\nabla\phi\cdot\hat{\mathbf{n}}dS = 0, \tag{4.25}$$

we have

$$\begin{aligned} A(\Psi) &= A(\psi) + \epsilon\int_V \left[-\psi\nabla^2\phi + \nabla^2\phi C'(-\nabla^2\psi)\right] dV \\ &= A(\psi) + \epsilon\int_V \left[C'(-\nabla^2\psi) - \psi\right]\nabla^2\phi dV. \end{aligned} \tag{4.26}$$

where the $S$ denotes the boundary of the volume $V$. The functional $A(\Psi)$ will be stationary for any function $\phi(x,y)$ when $\Psi = \psi$ if the function $C$ is chosen so that

$$C'(\omega) = \psi(\omega). \tag{4.27}$$

Then by Taylor expansion of the vorticity function in the equation (4.22),

$$\begin{aligned} C(-\nabla^2\Psi) &= C(-\nabla^2(\psi + \epsilon\phi)) \\ &= C(-\nabla^2\psi) + C'\epsilon\nabla^2\phi + \frac{1}{2}C''\epsilon^2(\nabla^2\phi)^2 + o(\epsilon^2). \end{aligned} \tag{4.28}$$

The functional $A(\Psi)$ will be written as follows:

$$A(\Psi) = A(\psi) + \frac{1}{2}\epsilon^2 B(\phi) + o(\epsilon^2), \tag{4.29}$$

where the functional $B(\phi)$ is given by

$$B(\phi) = \int_V \left[ |\nabla\phi|^2 - \frac{d\psi}{d\omega}(\nabla^2\phi)^2 \right] dV. \tag{4.30}$$

Because $A(\Psi)$ is constant, for all time the functional $B(\phi)$ is equal to its initial value in the linear approximation. The Arnol'd stability theorem can be summarised as follows; the magnitude of the perturbation $|\phi|$ can only increase when it contrives to keep the value of $B(\phi)$ small [4], [48], [10]. Thus an unstable normal mode $\phi = |\phi|e^{\sigma t}$, when Real$(\sigma) > 0$, must satisfy $B(\phi) = 0$.

### 4.2.2 Global stability criterion in two dimensional vortex flows

Now we consider the functional in the previous section

$$B(\phi) = \int_V \left[ |\nabla\phi|^2 - \frac{d\psi}{d\omega}(\nabla^2\phi)^2 \right] dV,$$

expressing the disturbance $\phi$ (see the section 4.3) as

$$\phi = a_\alpha(t)H_\alpha(x,y), \tag{4.31}$$

where the Greek subscript $\alpha$ is used for summation — i.e.

$$a_\alpha(t)H_\alpha(x,y) = \sum_{n=1}^{\infty} a_n H_n(x,y).$$

For a steady flow $\psi = H_m$, the functional will have the form as

$$\begin{aligned} B(\phi) &= \int_V \left[ |\nabla\phi|^2 - \frac{d\psi}{d\omega}(\nabla^2\phi)^2 \right] dV \\ &= \int_V \left[ a_\alpha^2\lambda_\alpha^2 ||H_\alpha||^2 - \frac{1}{\lambda_m^2} a_\alpha^2\lambda_\alpha^4 ||H_\alpha||^2 \right] dV \\ &= \int_V (1 - \frac{\lambda_\alpha^2}{\lambda_m^2}) a_\alpha^2\lambda_\alpha^2 ||H_\alpha||^2 dV. \end{aligned} \tag{4.32}$$

Each term of the functional will have a positive or a negative value according to the ratio $\frac{\lambda_\alpha}{\lambda_m}$. If we separate the functional with the positive and the negative terms and make it zero as follows:

$$\begin{aligned} B(\phi) &= \int_V (1 - \frac{\lambda_\alpha^2}{\lambda_m^2}) a_\alpha^2\lambda_\alpha^2 ||H_\alpha||^2 dV \\ &= \sum_{n=1}^{N-1} \int_V (1 - \frac{\lambda_n^2}{\lambda_m^2}) a_n^2\lambda_n^2 ||H_n||^2 dV \\ &\quad + \sum_{n=N}^{\infty} \int_V (1 - \frac{\lambda_n^2}{\lambda_m^2}) a_n^2\lambda_n^2 ||H_n||^2 dV \\ &= 0. \end{aligned} \tag{4.33}$$

The above equation is a necessary condition for a perturbation $\phi$ to be destabilising. Although (4.33) does not provide complete stability information, nevertheless some interesting conclusions can be drawn. Since the first sum is positive and the second negative, terms from each must be present to satisfy the equation. Thus a destabilising $\phi$ must contain some positive $H_m$ components with $n < m$ and some negative with $n > m$.

In the next section, we shall use a normal mode analysis in order to find the exact stability boundary.

## 4.3 Nonlinear evolution of flow

In this section we consider the time-evolution of non-steady flow. We derive a system of ordinary differential equations for the evolution of the Fourier coefficients in the normal mode expansion of the stream function. Then we use these equations to give the general condition for steady flow and to show that single Fourier-component flows are stable.

A general velocity field $\mathbf{u}$ can be represented with the stream function

$$\mathbf{u} = \nabla\psi \times \hat{\mathbf{z}}, \tag{4.34}$$

and the stream function $\psi$ can be expanded in terms of Fourier components,

$$\psi = a_\alpha(t) H_\alpha(x, y). \tag{4.35}$$

The vorticity equations are obtained from the Navier-Stokes equations as follows:

$$\frac{\partial\omega}{\partial t} + \mathbf{u} \cdot \nabla\omega = 0. \tag{4.36}$$

Substituting (4.34) and (4.35) into (4.36), we have

$$\dot{a}_\alpha(t)\lambda_\alpha^2 H_\alpha + a_\beta(t) a_\alpha(t)\lambda_\alpha^2 [H_\alpha, H_\beta] = 0. \tag{4.37}$$

By taking the inner product of the above equation with the eigenfunctions $H_m$ and by the property of orthogonality, we have

$$\dot{a}_m(t)\lambda_m^2 ||H_m||^2 + \lambda_\alpha^2 M_{m\alpha\beta}\, a_\alpha a_\beta = 0, \tag{4.38}$$

where

$$M_{m\alpha\beta} = \int_\Gamma H_m [H_\alpha, H_\beta] d\Gamma. \tag{4.39}$$

The above system of ordinary differential equations were numerically integrated in time using the NAG routine D02BBF. At each calculation step we checked the total kinetic energy $\Delta E$,

$$\begin{aligned} \Delta E &= \frac{1}{2}\rho \int_\Gamma \mathbf{u} \cdot \mathbf{u} d\Gamma \\ &= \frac{1}{2}\rho \int_\Gamma (\nabla\psi \times \hat{\mathbf{z}}) \cdot (\nabla\psi \times \hat{\mathbf{z}}) d\Gamma \\ &= \frac{1}{2}\rho\lambda^2 \int_\Gamma |\psi|^2 d\Gamma, \end{aligned} \tag{4.40}$$

and the total vorticity $\Omega$,

$$\begin{aligned} \Omega &= \int_\Gamma (-\nabla^2\psi) d\Gamma \\ &= \lambda^2 \int_\Gamma \psi d\Gamma, \end{aligned} \tag{4.41}$$

in order to ensure the energy and the vorticity conservation.

## 4.4 Steady flow

### 4.4.1 Derivation of the steady-flow condition

From the nonlinear flow evolution equation of flow (4.38) it follows that the condition for steady flow is

$$\lambda_\alpha^2 M_{m\alpha\beta}\, a_\alpha a_\beta = 0, \qquad m = 1,\ 2,\ 3, \ldots\ . \tag{4.42}$$

Clearly the coefficient $M_{m\alpha\beta}$ is antisymmetric in $\alpha$ and $\beta$ so (4.42) can be written in a more symmetrical form. Interchanging the dummy indices $\alpha$ and $\beta$, obtain

$$\begin{aligned} \lambda_\alpha^2 M_{m\alpha\beta} a_\alpha a_\beta &= \lambda_\beta^2 M_{m\beta\alpha} a_\beta a_\alpha \\ &= -\lambda_\beta^2 M_{m\alpha\beta} a_\alpha a_\beta. \end{aligned} \tag{4.43}$$

Thus the equation (4.42) can be written as

$$(\lambda_\alpha^2 - \lambda_\beta^2) M_{m\alpha\beta} a_\alpha(t) a_\beta(t) = 0, \qquad m = 1,\ 2,\ 3, \ldots\ . \tag{4.44}$$

One obvious solution of (4.44) is

$$\begin{cases} a_i = c \text{ (a constant)} & \text{when } i = k, \\ a_i = 0 & \text{when } i \neq k, \end{cases}$$

i.e. a flow consisting of just one Fourier component. In this case, $\omega = -\lambda_k^2 \psi$. For a flow consisting of just two Fourier components $a_i$ and $a_j$ say the condition for steady flow becomes

$$(\lambda_i^2 - \lambda_j^2) M_{mij} a_i(t) a_j(t) = 0, \qquad m = 1,\ 2,\ 3, \ldots\ , \tag{4.45}$$

which is satisfied only when $\lambda_i = \lambda_j$. Such repeated eigenvalues could occur for example in a square cell. Generally speaking, however, there seem to be no simple solutions for an infinite number of non-zero $a_\alpha$.

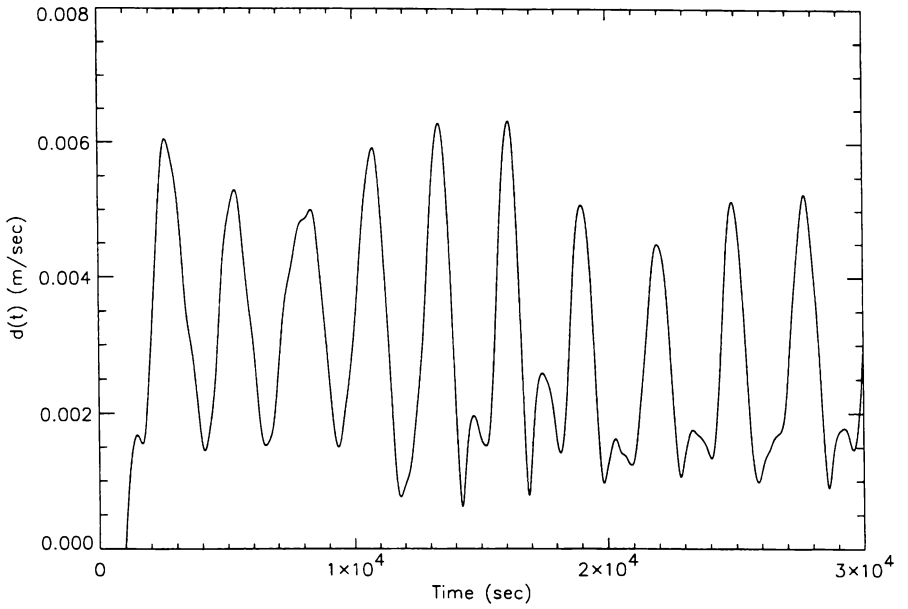


Figure 4.2: A typical unsteady oscillation of $d(t)$ in a rectangular container, where the initial disturbances $a_1 = a_2 = 0.01$m/sec and $t_0 = 1000$ sec.

### 4.4.2 Periodic flows

A more general question is the existence of periodic solutions. It is convenient to define a norm for the vector $\mathbf{A} = (a_1, a_2, a_3, ..., a_n)$ of Fourier components by setting

$$|\mathbf{A}(t)| = \left[\sum_{n=1}^{\infty} a_n^2(t)\right]^{\frac{1}{2}} \tag{4.46}$$

In order to test for periodic solutions we investigate the difference magnitude $d(t) = |\mathbf{A}(t) - \mathbf{A}(t_0)|$, where $t_0$ denotes a fixed time after the initial transient behavior during the wave oscillation. When we apply an initial disturbance such as $a_1 = a_2 = 10^{-2}$m/sec, $a_3 = a_4...a_n = 0$, a typical oscillation of $d(t)$ is shown in Figure 4.2. Figure 4.3 also shows an unsteady oscillation of $d(t)$ with various combinations of initial disturbances $a_2 = ra_1$.

If $d(t) = 0$, it means that $a_n(t) - a_n(t_0) = 0$ for all $n$ - i.e. the $a_n(t)$ are identical with the $a_n(t_0)$ so the solution over the next time interval $t - t_0$ will be a repeat of the previous one. This establishes that the solution is periodic. We calculated $d(t)$ for only the first 6000 seconds on account of numerical error. At least one of the solutions in figure 4.3 (when $r = 0.2$) appears to be periodic.

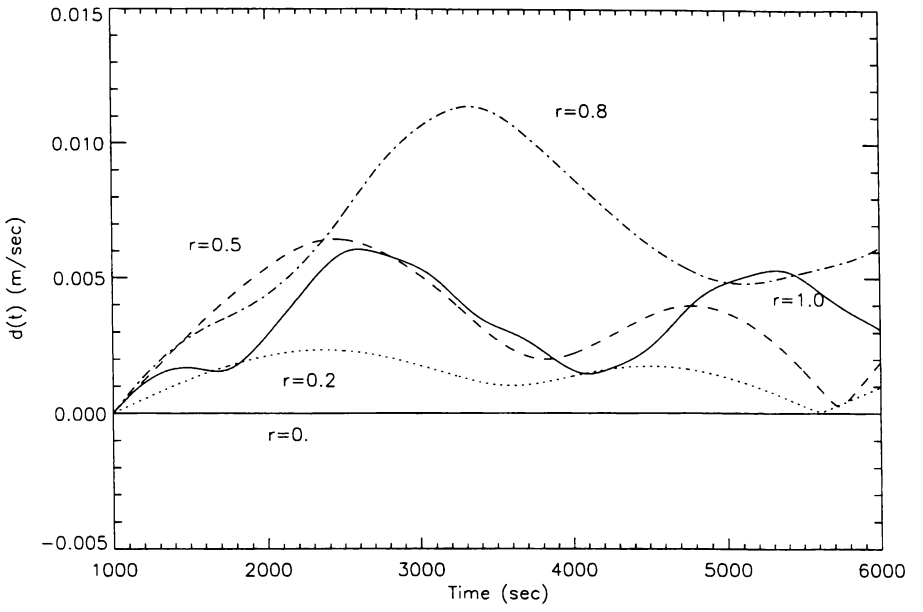


Figure 4.3: An unsteady oscillation of $d(t)$ where the initial disturbances $a_1 = 0.01, a_2 = ra_1$m/sec and $t_0 = 1000$ sec.

### 4.4.3 Linearised stability analysis of single-component flows

Suppose that $a_k = 1$ so that the basic flow is $\nabla H_k \times \hat{\mathbf{z}}$ and let the remaining $a_\alpha$ be small perturbations. The linearised form of equation (4.38) can be written

$$\lambda_m^2 ||H_m||^2 \dot{a}_m(t) + \frac{1}{2}(\lambda_k^2 - \lambda_\alpha^2) M_{mk\alpha} a_\alpha(t) + \frac{1}{2}(\lambda_\alpha^2 - \lambda_k^2) M_{m\alpha k} a_\alpha(t) = 0. \qquad (4.47)$$

It is shown in Appendix I that $M_{lmn}$ is antisymmetric in each pair of suffixes, so

$$(\lambda_\alpha^2 - \lambda_k^2) M_{m\alpha k} a_\alpha = (\lambda_k^2 - \lambda_\alpha^2) M_{mk\alpha} a_\alpha.$$

Thus we can write

$$\lambda_m^2 ||H_m||^2 \dot{a}_m(t) + (\lambda_k^2 - \lambda_\alpha^2) M_{mk\alpha} a_\alpha(t) = 0. \qquad (4.48)$$

Now if we define

$$b_\alpha = \left(\lambda_k^2 - \lambda_\alpha^2\right) a_\alpha, \qquad (4.49)$$

equation (4.48) can be written in the form

$$\frac{\lambda_m^2 ||H_m||^2}{(\lambda_m^2 - \lambda_k^2)} \dot{b}_m = M_{mk\alpha} b_\alpha, \qquad (4.50)$$

The final form of the evolution equation is

$$A_m \dot{b}_m = S_{m\alpha} b_\alpha, \tag{4.51}$$

where

$$A_m = \frac{\lambda_m^2 ||H_m||^2}{(\lambda_m^2 - \lambda_k^2)}, \qquad S_{m\alpha} = M_{mk\alpha}.$$

We can view (4.51) as a matrix equation

$$A\dot{\mathbf{b}} = S\,\mathbf{b}$$

where $\mathbf{b}$ is the vector of perturbed Fourier coefficients, $A$ is a diagonal (and hence symmetric) matrix and $S$ an antisymmetric matrix. The growth rates are the eigenvalues of the generalised eigenvalue problem

$$A\mathbf{x} = \lambda S\mathbf{x},$$

which are purely imaginary [34]. The instability growth is proportional to $e^{\lambda t}$, and since all $\lambda$ are purely imaginary there is no exponential growth. We conclude therefore that single-component flows are stable.

In order to confirm the analytical result, we calculated the eigenvalues numerically. When a large number of modes are involved it will take much time to find the eigenvalues so we calculated only the first ten modes in each direction using the NAG routine F02AFF. High-frequency modes in any case are more strongly damped. The numerical results also show that the eigenvalues are purely imaginary.

## 4.5 Conclusion

In this chapter, we showed single-component flows are steady, but it is not clear that any flow with more than one Fourier component is steady except in the case of repeated eigenvalues. We have also derived a global stability criterion by Arnol'd's stability theorem. Arnol'd's stability theorem gives some insight into the stability of a single-component flow but not a complete picture. A non-linear evolution equation is derived for multi-component flows. Numerical integration shows that periodic flows exist, but with quite long periods. The non-linear evolution equation can be used to derive conditions for a general steady flow.

Finally, we have shown that a single-component flow is stable. Hence any hydrodynamic instability must be due to interfacial effects.

In the following chapter we investigate interfacial instability between two liquid layers which is our main interest.

# Chapter 5

# Wave evolution equations

It is well known that disturbances can grow at the interface in aluminium reduction cells. The steady velocity difference is one of the main destabilising factors, as reviewed in Chapter 2. In this chapter, in order to investigate the interfacial instability, we shall formulate the wave evolution equations with the normal mode method. A simulation program is developed to follow the evolution of the interface using the wave evolution equations. The code is verified by reproducing gravity wave modes and by confirming energy conservation of the perturbed system.

## 5.1 Physical and mathematical simplifications

Some physical and mathematical simplifications are inevitable to formulate the system equations, as is usual in most analyses. The following simplifications are adopted in our model:

- The cell geometry is rectangular as shown in Figure 1.3. *The cell geometry is not simply rectangular but includes a frozen ledge as shown in Figure 1.1. This assumption is essential to formulate system equations analytically.*
- The gaps between the anodes are neglected. *The current and magnetic fields are not exactly uniform in most cases. Sometimes, we assume a uniform magnetic field to simplify the numerical calculations.*

- The basic flows are known and steady. *The basic flows are driven by the stationary electromagnetic forces in the cell and can be obtained from experimental data or numerical simulations.*

- The flows in both liquid layers are incompressible. *Both liquid aluminium and cryolite are almost incompressible.*

- The vertical component of rotational velocity is small. *Because of the strong turbulence, there is efficient vertical transport in a cell. We ignore the dependence of the rotational velocity in the vertical direction and consider only variations in the horizontal direction as the aluminium and the cryolite layers are relatively thin compared with the cell length and width .*

- Viscosity is negligible. *This is acceptable as the dynamic viscosity term is much smaller than other physical terms such as pressure, inertia and magnetic forces. However, the boundary effect is used to estimate a frictional damping in this thesis by a model introduced by Moreau [51].*

- The bubble induced flow is neglected. *It can influence the flow in the cryolite layer [87]. However, we will ignore it to simplify our analysis, and it would be very difficult to estimate.*

## 5.2 Normal mode analysis

In this section the system equations will be obtained from the linearised equations of the motion, the interface boundary condition and the vorticity equations. The normal mode method will be adopted to formulate the wave evolution equations in terms of eigenfunctions which satisfy the lateral boundary conditions. The velocity field is decomposed into rotational and irrotational terms, which can be expressed in terms of a stream function and velocity potential respectively. Then we shall substitute the velocity perturbation into the equation of motion and the interface equation and make use of the orthogonality of the basis eigenfunctions in order to obtain scalar equations. Finally, a system of ordinary differential equations for the eigenfunction coefficients will be obtained.

The steady velocity difference causes a pressure difference at the interface between

two liquid layers, which disturbs the flow in the cell. Thus the steady pressure terms will be included for the continuity of the pressure at the interface. We integrate numerically the wave evolution equations forwards in time from an initial equilibrium state, where the steady velocity is zero.

### 5.2.1 Eigenfunctions

As is usual in the normal mode analysis, the eigenfunctions $E_n(x,y)$, $n = 1, 2, ...$, of the eigenvalue problem

$$\nabla^2 E + \lambda^2 E = 0, \tag{5.1}$$

$$\nabla E \cdot \hat{\mathbf{n}} = 0 \quad \text{on lateral boundaries}, \tag{5.2}$$

are chosen as our basis functions, satisfying the same lateral boundary conditions as the velocity field. The eigenvalue corresponding to $E_n$ is denoted by $\lambda_n$. The basis eigenfunctions $E_n$ satisfy the following orthogonality relations:

$$\int_S E_n E_m dxdy = \delta_{mn}||E_n||^2 = ||E_m||^2,$$

$$\int_S \nabla E_n \cdot \nabla E_m dxdy = \delta_{mn}\lambda_n^2||E_n||^2 = \lambda_m^2||E_m||^2. \tag{5.3}$$

In a rectangular cell, $E_n$ are chosen as

$$E_n = \cos\frac{n_x \pi x}{a} \cos\frac{n_y \pi y}{b}.$$

Then, the interface displacement can be expanded in terms of the $E_n$ as:

$$\eta = \sum_{n=1}^{\infty} \eta_n(t) E_n, \tag{5.4}$$

where the $\eta_n(t)$ are functions of time, which we call wave evolution coefficients. We adopt the usual assumption of linear wave theory that $\eta$ is very small, compared with the wavelength.

### 5.2.2 Velocity perturbation

In general, the Lorentz force is rotational and therefore so is the fluid motion in a cell. It is useful to decompose the velocity perturbation $\mathbf{u}$ into a rotational term $\mathbf{u}_r$

which is purely horizontal and an irrotational term $\mathbf{u}_p$. The velocity field $\mathbf{u}_p$ can be expressed in terms of a velocity potential $\phi$ and $\mathbf{u}_r$ in terms of a stream function $\psi$ mathematically as follows:

$$\begin{aligned} \mathbf{u} &= \mathbf{u}_p + \mathbf{u}_r \\ &= \nabla\phi(x,y,z) + \nabla\psi(x,y)\times\mathbf{z}. \end{aligned} \tag{5.5}$$

The boundary conditions for the $\phi$ and the $\psi$ are summarised as:

$$\begin{aligned} \nabla^2\phi &= \nabla\cdot\mathbf{u}_p = 0, \frac{\partial\phi}{\partial n} = 0 \text{ on solid boundaries,} \\ \nabla^2\psi &= -\omega, \psi = 0 \text{ on lateral boundaries.} \end{aligned} \tag{5.6}$$

For the aluminium and cryolite layers, since $\mathbf{u}$ and $\mathbf{u_r}$ are both solenoidal we have

$$\nabla^2\phi^i = 0, \quad \text{(i=a,c)}.$$

Also on the solid walls, the boundary condition are written as:

$$\frac{\partial\phi^i}{\partial n} = 0, \psi^i = 0.$$

The $\phi^i$ are both specified uniquely since they must satisfy the kinematic boundary condition,

$$\frac{\partial\phi^i}{\partial n} = \dot{\eta}$$

on the interface. The velocity potential $\phi$ is chosen to have the following form:

$$\begin{aligned} \phi &= \sum_{n=0}^{\infty} g_n(z)E_n(x,y)b_n(t) \\ &\stackrel{def}{=} \phi_\alpha b_\alpha(t), \end{aligned} \tag{5.7}$$

where the function $g_n(z)$ is chosen as:

$$\begin{aligned} g_n^a(z) &= \frac{\cosh\left[\lambda_n\left(z+h^a\right)\right]}{\lambda_n\sinh\left(\lambda_n h^a\right)}, \\ g_n^c(z) &= -\frac{\cosh\left[\lambda_n\left(z-h^c\right)\right]}{\lambda_n\sinh\left(\lambda_n h^c\right)}, \end{aligned} \tag{5.8}$$

to satisfy the vertical boundary conditions

$$g_n^a(z)' = g_n^c(z)' = 1 \text{ at } z = 0,$$

$$g_n^a(z)' = g_n^c(z)' = 0 \text{ at } z = -h^a \text{ or } z = h^c, \tag{5.9}$$

where $h^a$ and $h^c$ denote liquid aluminium depth and ACD respectively (see Figure 1.3).

As we assume the vertical component of $\mathbf{u}_r$ is small, we can expand the rotational velocity field in terms of two dimensional stream function $\psi(x, y)$ as follows:

$$\psi = H_\alpha(x, y)c_\alpha(t), \tag{5.10}$$

where, in order to expand $\psi$, we introduce a second set of eigenfunction

$$H_n = \sin\frac{n_x\pi x}{a}\sin\frac{n_y\pi y}{b},$$

satisfying

$$\nabla^2 H + \lambda^2 H = 0, \tag{5.11}$$

$$H = 0 \text{ on lateral boundaries.} \tag{5.12}$$

Similarly, in steady state, the basic flow $\mathbf{U}$ and the steady vorticity $\mathbf{\Omega}$ can be expressed in terms of scalar function $\Psi$ as follows:

$$\begin{aligned} \mathbf{U} &= \nabla\Psi \times \hat{\mathbf{z}} \\ &= U\nabla H(x, y) \times \hat{\mathbf{z}}, \end{aligned} \tag{5.13}$$

$$\begin{aligned} \mathbf{\Omega} &= \nabla \times \mathbf{U} \\ &= U\nabla \times \{\nabla H(x, y) \times \hat{\mathbf{z}}\} \\ &= -U\nabla^2 H(x, y)\hat{\mathbf{z}} \\ &= U\lambda^2 H(x, y)\hat{\mathbf{z}}. \end{aligned} \tag{5.14}$$

The steady velocity $U$ is assumed to be constant in Ziegler's work. The pressures vary as $\frac{1}{2}\rho^a(v^a)^2$ in the aluminium and as $\frac{1}{2}\rho^c(v^c)^2$ in the cryolite, so they cannot balance everywhere on the interface because $\rho^a \neq \rho^c$ and $v^a \neq v^c$. Thus, his computation begins with an initial pressure imbalance between two liquid layers. However, in order to avoid the initial pressure difference, we increase the steady velocity gradually from zero to a constant value for the transient period of 10 seconds as shown in Figure 5.1,

$$U = U_0(1 - e^{-\beta t}), \tag{5.15}$$

where the $\beta$ is related to the acceleration rate. The value of $U$ will be constant after the initial transient period $t_0 = O(\beta^{-1})$.

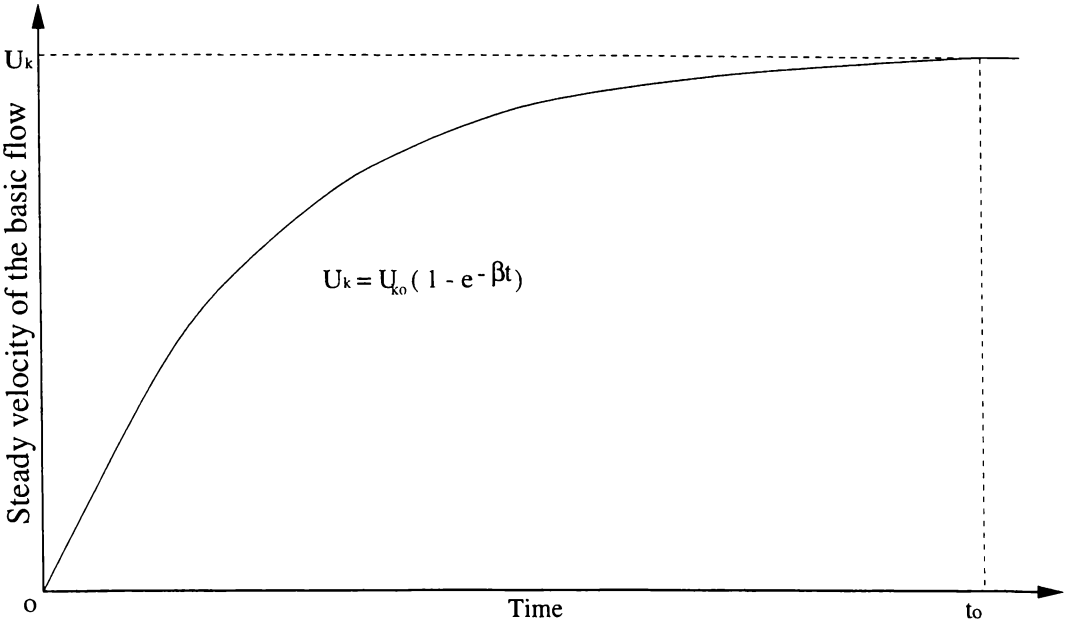


Figure 5.1: The initial adjustment of the steady velocity.

### 5.2.3 Equations of motion

The first-order perturbation of the Navier-Stokes equations (see Section 3.2) is written as :

$$\begin{aligned} & \rho\frac{\partial \mathbf{u}}{\partial t} + k\mathbf{u} + \rho\Omega\hat{\mathbf{z}} \times \mathbf{u} + \rho\omega\hat{\mathbf{z}} \times \mathbf{U} \\ & +\nabla p_T - \mathbf{f} \\ = \; & 0, \end{aligned} \tag{5.16}$$

where $k$ and $\mathbf{f}$ denote frictional drag coefficient and body force respectively and the pressure term $p_T$ is represented as:

$$p_T = p + \rho\mathbf{U} \cdot \mathbf{u}. \tag{5.17}$$

### 5.2.4 The pressure distribution of the basic steady flow

In order to formulate the pressure continuity condition at the interface we must first find the zeroth-order pressure distribution. From Navier-Stokes equations for two dimensional steady flows, we can obtain the pressure gradient term $\nabla P$ as follows:

$$\rho\ \mathbf{U}\cdot\nabla\ \mathbf{U} = -\nabla P - \rho g\hat{\mathbf{z}}, \tag{5.18}$$

$$\rho(\ \mathbf{\Omega} \times \mathbf{U} + \nabla \frac{U^2}{2}) = -\nabla P - \rho g \hat{\mathbf{z}}$$

$$\rho\lambda^2\psi\nabla\psi + \nabla\left(P + \rho\frac{U^2}{2}\right) = -\rho g\hat{\mathbf{z}}. \tag{5.19}$$

Then integration of the above equation gives the pressure distribution as

$$P = c - \frac{\rho}{2}\left(\lambda^2\psi^2 + |\nabla\psi|^2\right) - \rho g z.$$

By the boundary condition $\psi = 0$ at $x = y = z = 0$, when we take a single-Fourier component flow $\psi = UH_n$ we have

$$\begin{aligned} P &= P_0 - \frac{\rho}{2}\left(\lambda^2\psi^2 + |\nabla\psi|^2\right) - \rho g z \\ &= P_0 - \frac{\rho}{2}U^2\left(\lambda^2 H^2 + |\nabla H|^2\right) - \rho g z, \end{aligned} \tag{5.20}$$

where $U$ is a constant and $P_0$ denotes the pressure at $x = y = z = 0$.

The above equation represents the pressure distribution by the steady velocity field. It is interesting to observe that the wave length of the pressure distribution is half that of the velocity distribution because of the square terms in the above equation. In the next section, this expression for the steady pressure $P$ is needed to formulate the pressure continuity condition at the interface.

### 5.2.5 The continuity of the pressure at the interface

From the continuity of the total pressure across the interface, we can write

$$P^a + p^a = P^c + p^c.$$

or

$$p^a - p^c = P^c - P^a. \tag{5.21}$$

where $p$ =the pressure perturbation and $P$ =the steady pressure distribution of the basic flow.

Using (5.20) we find that pressure continuity across the interface implies

$$\begin{aligned} p^a - p^c &= (P^c - P^a) \\ &= \frac{1}{2}\left(\rho^a(U^a)^2 - \rho^c(U^c)^2\right)\left(\lambda^2 H^2 + |\nabla H|^2\right) \\ &\quad + (\rho^a - \rho^c)\, g\eta. \end{aligned} \tag{5.22}$$

This equation gives the displacement of the interface necessary for continuity of pressure.

### 5.2.6 Scalar formulation

All the dynamic equations obtained from the previous sections are vector equations; to obtain the scalar evolution equation for time-dependent coefficients $b_m$, $c_m$ and $\eta_m$, we take the inner product of the equation of motion with $\nabla\phi_m$ as follows:

$$\begin{aligned} \rho &< \dot{\mathbf{u}}, \nabla\phi_m > + < k\mathbf{u}, \nabla\phi_m > + \rho < \Omega\hat{\mathbf{z}} \times \mathbf{u}, \nabla\phi_m > \\ +\rho &< \omega\hat{\mathbf{z}} \times \mathbf{U}, \nabla\phi_m > + < \nabla p_T, \nabla\phi_m > - < \mathbf{f}, \nabla\phi_m >= 0, \end{aligned} \tag{5.23}$$

where the symbol <> denotes the inner product in the domain $V$,

$$< \mathbf{x}, \mathbf{y} >= \int_V \mathbf{x} \cdot \mathbf{y} dV.$$

The first inner product term $\rho < \dot{\mathbf{u}}, \nabla\phi_m >$ is written by the divergence theorem as:

$$\begin{aligned} &< \dot{\mathbf{u}}, \nabla\phi_m >= \int_V \nabla \cdot (\dot{\mathbf{u}}\phi_m)\, dV \\ &= \int_\Gamma (\dot{\mathbf{u}} \cdot \hat{\mathbf{n}})\, \phi_m d\Gamma, \end{aligned} \tag{5.24}$$

where $\hat{\mathbf{n}}$ is a normal vector to the boundaries in the domain $V$. The only contribution to the above integral arises from the upper and lower surface of the interface, $\Gamma^+$ and $\Gamma^-$, as $\dot{\mathbf{u}} \cdot \hat{\mathbf{n}} = 0$ on solid boundaries. Thus, we have the result for each layer in terms of the evolution variable $\dot{b}_m$ as follows:

$$\begin{aligned} \rho &< \dot{\mathbf{u}}, \nabla\phi_m >= \rho \int_\Gamma (\dot{\mathbf{u}} \cdot \hat{\mathbf{n}})\, \phi_m d\Gamma \\ &= \rho \int_\Gamma \frac{\partial}{\partial t} (\nabla\phi + \nabla\psi \times \mathbf{z}) \cdot \hat{\mathbf{n}} \phi_m d\Gamma. \end{aligned}$$

As the second rotational velocity term is horizontal, it will vanish with the inner product of the vertical vector $\hat{\mathbf{n}}$ and only the vertical irrotational velocity term will remain as follows:

$$\begin{aligned} \rho &< \dot{\mathbf{u}}, \nabla\phi_m >= \rho \int_\Gamma \frac{\partial}{\partial t} (\nabla\phi) \cdot \hat{\mathbf{z}} \phi_m d\Gamma \\ &= \rho \int_\Gamma E_\alpha\, \dot{b}_\alpha\, \phi_m d\Gamma \\ &= \rho \int_\Gamma E_\alpha\, (g_m(0) E_m)\, d\Gamma \dot{b}_\alpha \\ &= \rho g_m(0) \int_\Gamma E_\alpha E_m d\Gamma \dot{b}_\alpha \\ &= \rho g_m(0) \delta_{m\alpha} ||E_m||^2 \dot{b}_\alpha \\ &= \rho g_m(0) ||E_m||^2 \dot{b}_m. \end{aligned} \tag{5.25}$$

The above calculation is obtained on the lower surface of the interface (aluminium layer). This calculation applies to the aluminium layer where the outward normal on the interface is $\hat{\mathbf{z}}$. In the cryolite layer the normal is $-\hat{\mathbf{z}}$ and the negative result will be obtained. Thus, we use a variable $\gamma$ to represent the direction of integration as follows:

$$\rho < \dot{\mathbf{u}}, \nabla\phi_m >= \gamma\rho g_m(0)||E_m||^2\dot{b}_m, \tag{5.26}$$

where $\gamma^a = 1$ and $\gamma^c = -1$, which depends on the lower and upper surface of interface, $\Gamma^-$ and $\Gamma^+$. Here we take $\hat{\mathbf{n}} = \hat{\mathbf{z}}$ by linearisation.

Similarly, we have the second inner product $< k\mathbf{u}, \nabla\phi_m >$ in terms of the evolution variable $b_m$ as follows:

$$\begin{aligned} < k\mathbf{u}, \nabla\phi_m >= & \int_V \nabla\cdot(k\mathbf{u})\,\phi_m dV \\ = & \int_\Gamma (k\mathbf{u}\cdot\hat{\mathbf{n}})\,\phi_m d\Gamma \\ = & kg_m(0)b_\alpha \int_\Gamma E_\alpha E_m d\Gamma \\ = & \gamma k g_m(0)\delta_{m\alpha}||E_\alpha||^2 b_\alpha \\ = & \gamma k g_m(0)||E_m||^2 b_m. \end{aligned} \tag{5.27}$$

The third inner product $\rho < \Omega\hat{\mathbf{z}}\times\mathbf{u}, \nabla\phi_m >$ is written in terms of the evolution variables $b_\alpha$ and $c_\alpha$ as follows:

$$\begin{aligned} \rho < \Omega\hat{\mathbf{z}}\times\mathbf{u}, \nabla\phi_m >= & \rho\int_V (\Omega\hat{\mathbf{z}}\times\mathbf{u})\cdot\nabla\phi_m dV \\ = & \rho\int_V (\Omega\hat{\mathbf{z}}\times\mathbf{u})\cdot\nabla\left(g_m(z)E_m\right)dV \\ = & \rho\int_V \{\Omega\hat{\mathbf{z}}\times(\nabla b_\alpha E_\alpha g_\alpha + \nabla c_\alpha H_\alpha\times\hat{\mathbf{z}})\}\cdot\nabla\left(g_m(z)E_m\right)dV. \end{aligned} \tag{5.28}$$

By the separation of variables for the volume integration, this equation can be expressed in terms of $b_n$ and $c_n$ as:

$$\begin{aligned} \rho < \Omega\hat{\mathbf{z}}\times\mathbf{u}, \nabla\phi_m >= & \rho\int g_\alpha(z)g_m(z)dz\int_\Gamma \Omega[E_\alpha, E_m]d\Gamma b_\alpha \\ & +\rho\int g_m(z)dz\int_\Gamma \Omega\nabla H_\alpha\cdot\nabla E_m d\Gamma c_\alpha \\ = & \rho\lambda_k^2 U_k\,\bar{g}_{m\alpha}\,Q^{(1)}_{m\alpha k}b_\alpha \\ & +\rho\lambda_k^2 U_k\,\bar{g}_m\,Q^{(2)}_{m\alpha k}c_\alpha, \end{aligned} \tag{5.29}$$

where the subscript $k$ represents the basic steady flow configuration and the integration coefficients are defined in Appendix II.

The fourth inner product $\rho < \omega\hat{\mathbf{z}} \times \mathbf{U}, \nabla\phi_m >$ is written in terms of the evolution variable $c_\alpha$ as follows:

$$\begin{aligned}
\rho \;<\; & \omega\hat{\mathbf{z}} \times \mathbf{U}, \nabla\phi_m >= \rho \int_V (\omega\hat{\mathbf{z}} \times \mathbf{U}) \cdot \nabla\phi_m dV \\
= \; & \rho \int_V \left[ \left( -\nabla^2\psi \right) \hat{\mathbf{z}} \times (U_k \nabla H_k \times \mathbf{z}) \right] \cdot \nabla\phi_m dV \\
= \; & \rho \int_V \left[ \left( \lambda_\alpha^2 H_\alpha c_\alpha \right) \hat{\mathbf{z}} \times (U_k \nabla H_k \times \mathbf{z}) \right] \cdot \nabla\phi_m dV \\
= \; & \rho \int_V \left( \lambda_\alpha^2 U_k H_\alpha \nabla H_k c_\alpha \right) \cdot \nabla \left( g_m(z) E_m \right) dV \\
= \; & \rho \lambda_\alpha^2 U_k \; \bar{g}_m \; Q^{(3)}_{m\alpha k} c_\alpha .
\end{aligned} \tag{5.30}$$

The fifth inner product $< \nabla p_T, \nabla\phi_m >$ is written in terms of the evolution variables $b_\alpha$, $c_\alpha$ and $\eta_\alpha$ as follows:

$$\begin{aligned}
< \; & \nabla p_T, \nabla\phi_m >= \int_V \nabla p_T \cdot \nabla\phi_m dV \\
= \; & \int_\Gamma p_T \left( \nabla\phi_m \cdot \hat{\mathbf{n}} \right) d\Gamma \\
= \; & \int_\Gamma p_T E_m d\Gamma \\
= \; & \int_\Gamma \left( p + \rho \mathbf{U} \cdot \mathbf{u} \right) E_m d\Gamma \\
= \; & \frac{1}{2} \rho (U_k)^2 \int_\Gamma \left( \lambda_k^2 H_k^2 + |\nabla H_k|^2 \right) E_m d\Gamma \\
& + \rho g ||E_\alpha||^2 \delta_{m\alpha} \eta_\alpha \\
& + \rho U_k g_\alpha(0) Q^{(4)}_{m\alpha k} b_\alpha \\
& + \rho U_k Q^{(5)}_{m\alpha k} c_\alpha ,
\end{aligned} \tag{5.31}$$

where the following calculations are used to obtain the integration coefficients:

$$\begin{aligned}
\int_\Gamma p E_m d\Gamma \; = \; & \int_\Gamma \left[ \frac{1}{2} \rho (U_k)^2 \left( \lambda_k^2 H_k^2 + |\nabla H_k|^2 \right) \right] E_m d\Gamma \\
& + \int_\Gamma \left( \rho g \eta \right) E_m d\Gamma \\
= \; & \frac{1}{2} \rho (U_k)^2 \int_\Gamma \left( \lambda_k^2 H_k^2 + |\nabla H_k|^2 \right) E_m d\Gamma \\
& + \rho g \int_\Gamma E_\alpha E_m d\Gamma \eta_\alpha \\
= \; & \frac{1}{2} \rho (U_k)^2 \int_\Gamma \left( \lambda_k^2 H_k^2 + |\nabla H_k|^2 \right) E_m d\Gamma \\
& + \rho g ||E_m||^2 \eta_m ,
\end{aligned} \tag{5.32}$$

$$\begin{aligned}
\mathbf{U} \cdot \mathbf{u} \; = \; & \mathbf{U} \cdot (\mathbf{u}_p + \mathbf{u}_r) \\
= \; & (U_k \nabla H_k \times \mathbf{z}) \cdot \nabla \left( g_\alpha(z) E_\alpha b_\alpha \right)
\end{aligned}$$

$$
\begin{aligned}
& + (U_k \nabla H_k \times \hat{\mathbf{z}}) \cdot (\nabla H_\alpha c_\alpha \times \hat{\mathbf{z}}) \\
= \; & U_k g_\alpha(z)[E_\alpha, H_k] b_\alpha \\
& + U_k \nabla H_k \cdot \nabla H_\alpha c_\alpha. \qquad (5.33)
\end{aligned}
$$

Finally, the last inner product $< \mathbf{f}, \nabla\phi_m >$ is written in terms of the evolution variable $\eta_\alpha$ as follows:

$$
\begin{aligned}
& < \mathbf{f}, \nabla\phi_m > \\
= \; & < \mathbf{f}_{M\alpha}\eta_\alpha, \nabla\phi_m > \\
= \; & \int_V \mathbf{f}_{M\alpha} \cdot \nabla\phi_m dV \eta_\alpha \\
= \; & \bar{G}_{m\alpha}\, \eta_\alpha, \qquad (5.34)
\end{aligned}
$$

where

$$
\begin{aligned}
\bar{G}_{m\alpha} &= < \mathbf{f}_{M\alpha}, \nabla\phi_m > \\
&= \int_V \mathbf{f}_{M\alpha} \cdot \nabla\phi_m dV, \\
\mathbf{f}_{M\alpha} &= \mathbf{j}_\alpha \times \mathbf{B}. \qquad (5.35)
\end{aligned}
$$

The $\mathbf{f}_{M\alpha}$ and the $\mathbf{j}_\alpha$ denote the current perturbation and the magnetic force due to the $\alpha$'th mode of the interfacial wave respectively. By combining the above results, we have the first of five evolution equations:

$$
\begin{aligned}
& A_m \dot{b}^a_m + B_m \dot{b}^c_m + C_{m\alpha} b^a_\alpha + D_{m\alpha} b^c_\alpha \\
& + E_{m\alpha} c^a_\alpha + F_{m\alpha} c^c_\alpha + G_{m\alpha}\eta_\alpha + Q_m = 0. \qquad (5.36)
\end{aligned}
$$

The coefficient matrices in the above equation are listed in Appendix II.

### 5.2.7 The interface boundary condition

The kinematic condition on the interface is considered in this section. The vertical velocity of the fluid particles on the interface satisfies:

$$
\begin{aligned}
\mathbf{u}_{z=0} &= \frac{D\eta}{Dt} \\
&= \dot{\eta} + \mathbf{U} \cdot \nabla\eta, \qquad (5.37)
\end{aligned}
$$

and

$$
\begin{aligned}
\mathbf{u}_{z=0} &= \frac{\partial\phi}{\partial z} \\
&= E_\alpha b_\alpha. \qquad (5.38)
\end{aligned}
$$

Thus we have

$$\begin{aligned} E_\alpha b_\alpha &= \dot{\eta} + \mathbf{U} \cdot \nabla \eta \\ &= \dot{\eta} + (U_k \nabla H_k \times \mathbf{z}) \cdot \nabla E_\alpha \eta_\alpha \\ &= E_\alpha \dot{\eta}_\alpha + U_k [E_\alpha, H_k] \eta_\alpha, \end{aligned} \tag{5.39}$$

where the square bracket [A,B] denotes a Jacobian.

By the orthogonal property of the eigenfunctions $E_n$,

$$\begin{aligned} b_\alpha \int_\Gamma E_\alpha E_m d\Gamma &= \dot{\eta}_\alpha \int_\Gamma E_\alpha E_m d\Gamma \\ &\quad + U_k \int_\Gamma [E_\alpha, H_k] E_m d\Gamma \eta_\alpha, \end{aligned}$$

or

$$||E_m||^2 b_m = ||E_m||^2 \dot{\eta}_m + U_k Q^{(4)}_{m\alpha k} \eta_\alpha.$$

Dividing both sides by $||E_m||^2$, we have the interface equations as follows:

$$b_m = \dot{\eta}_m + \frac{U_k}{||E_m||^2} Q^{(4)}_{m\alpha k} \eta_\alpha. \tag{5.40}$$

From the above equations, we can obtain the second and the third evolution equations in terms of the variable $b_m$ and $\eta_\alpha$:

$$b^a_m - b^c_m = \frac{(U^a_k - U^c_k)}{||E_m||^2} Q^{(4)}_{m\alpha k} \eta_\alpha,$$

$$b^a_m = \dot{\eta}_m + \frac{U^a_k}{||E_m||^2} Q^{(4)}_{m\alpha k} \eta_\alpha,$$

or

$$b^c_m = b^a_m - H_{m\alpha} \eta_\alpha, \tag{5.41}$$

$$\dot{\eta}_m + I_{m\alpha} \eta_\alpha - b^a_m = 0. \tag{5.42}$$

### 5.2.8 The vorticity equation

The perturbation of vorticity can be obtained by taking the $z$-component of the curl of (5.16) as follows:

$$\frac{\partial \omega}{\partial t} + \frac{k}{\rho} \omega + \mathbf{u} \cdot \nabla \Omega + \mathbf{U} \cdot \nabla \omega - \frac{1}{\rho} (\nabla \times \mathbf{f}) \cdot \hat{\mathbf{z}} = 0, \tag{5.43}$$

where

$$\begin{aligned}
\mathbf{u}\cdot\nabla\Omega &= (\mathbf{u}_p+\mathbf{u}_r)\cdot\nabla\left(\lambda_k^2U_kH_k\right)\\
&= \nabla\left(g_\alpha(z)E_\alpha b_\alpha\right)\cdot\nabla\left(\lambda_k^2U_kH_k\right)\\
&\quad +(\nabla H_\alpha c_\alpha\times\hat{\mathbf{z}})\cdot\nabla\left(\lambda_k^2U_kH_k\right)\\
&= g_\alpha(z)\lambda_k^2U_k\nabla E_\alpha\cdot\nabla H_k b_\alpha\\
&\quad -\lambda_k^2U_k[H_\alpha,H_k]c_\alpha, \qquad (5.44)
\end{aligned}$$

$$\begin{aligned}
\mathbf{U}\cdot\nabla\omega &= \mathbf{U}\cdot\nabla\left(\lambda_\alpha^2H_\alpha c_\alpha\right)\\
&= (U_k\nabla H_k\times\hat{\mathbf{z}})\cdot\nabla\left(\lambda_\alpha^2H_\alpha c_\alpha\right)\\
&= \lambda_\alpha^2U_k[H_\alpha,H_k]c_\alpha. \qquad (5.45)
\end{aligned}$$

Taking the inner product with the eigenfunction $H_m$, we have

$$\begin{aligned}
&\lambda_m^2||H_m||^2\,\dot{c}_m+\lambda_\alpha^2\frac{k}{\rho}||H_\alpha||^2\delta_{m\alpha}c_\alpha\\
&+\bar{g}_\alpha\,\lambda_k^2U_kQ^{(3)}_{\alpha km}b_\alpha\\
&+\left(\lambda_\alpha^2-\lambda_k^2\right)U_kQ^{(7)}_{m\alpha k}c_\alpha\\
&-\frac{1}{\rho}Q^{(8)}_{m\alpha}\eta_\alpha=0. \qquad (5.46)
\end{aligned}$$

Finally we can obtain two additional evolution equations as follows:

$$J_m\dot{c}^a_m+K_{m\alpha}b^a_\alpha+L_{m\alpha}c^a_\alpha+M_{m\alpha}\eta_\alpha = 0, \qquad (5.47)$$

$$J_m\dot{c}^c_m+N_{m\alpha}b^c_\alpha+O_{m\alpha}c^c_\alpha+P_{m\alpha}\eta_\alpha = 0, \qquad (5.48)$$

where the wave evolution coefficients are listed in Appendix II.

## 5.3 Wave evolution equations

As a result, we have the wave evolution equations for the five sets of unknown variables $b^a_\alpha, b^c_\alpha, c^a_\alpha, c^c_\alpha$ and $\eta_\alpha$ in the aluminium reduction cell as follows:

$$\begin{aligned}
&A_m\dot{b}^a_m+B_m\dot{b}^c_m+C_{m\alpha}b^a_\alpha+D_{m\alpha}b^c_\alpha\\
&+E_{m\alpha}c^a_\alpha+F_{m\alpha}c^c_\alpha+G_{m\alpha}\eta_\alpha+Q_m=0,
\end{aligned}$$

$$b^c_m=b^a_m-H_{m\alpha}\eta_\alpha,$$

$$\dot{\eta}_m + I_{m\alpha}\eta_\alpha - b^a_m = 0,$$

$$\begin{aligned} J_m\dot{c}^a_m + K_{m\alpha}b^a_\alpha + L_{m\alpha}c^a_\alpha + M_{m\alpha}\eta_\alpha &= 0, \\ J_m\dot{c}^c_m + N_{m\alpha}b^c_\alpha + O_{m\alpha}c^c_\alpha + P_{m\alpha}\eta_\alpha &= 0. \end{aligned} \tag{5.49}$$

The first set of equations are obtained from the linearised Navier-Stokes equations, the second and the third from the interface equations and the last two sets from the vorticity equations. The second equation (5.49) can be used to eliminate $\dot{b}^c_\alpha$ and $b^c_\alpha$ in the above equations. Thus we can reduce the number of the equations as follows:

$$\begin{aligned} &A_m\dot{b}^a_m + B_m\left(\dot{b}^a_m - H_{m\alpha}\dot{\eta}_\alpha\right) + C_{m\alpha}b^a_\alpha + D_{mk}\left(b^a_k - H_{kn}\eta_\alpha\right) \\ &+E_{m\alpha}c^a_\alpha + F_{m\alpha}c^c_\alpha + G_{m\alpha}\eta_\alpha + Q_m = 0. \end{aligned}$$

$$\begin{aligned} J_m\dot{c}^a_m + K_{m\alpha}b^a_\alpha + L_{m\alpha}c^a_\alpha + M_{m\alpha}\eta_\alpha &= 0, \\ J_m\dot{c}^c_m + N_{mk}\left(b^a_k - H_{kn}\eta_\alpha\right) + O_{m\alpha}c^c_\alpha + P_{m\alpha}\eta_\alpha &= 0, \end{aligned}$$

$$\dot{\eta}_m + I_{m\alpha}\eta_\alpha - b^a_m = 0. \tag{5.50}$$

Sometimes, it is convenient to write the above equations as $4m \times 4m$ matrix form as follows:

$$\begin{aligned} &\begin{bmatrix} (A_\alpha + B_\alpha)\,\delta_{m\alpha} & 0 & 0 & -B_m H_{m\alpha} \\ 0 & J_\alpha\delta_{m\alpha} & 0 & 0 \\ 0 & 0 & J_\alpha\delta_{m\alpha} & 0 \\ 0 & 0 & 0 & \delta_{m\alpha} \end{bmatrix} \begin{Bmatrix} \dot{b}^a_\alpha \\ \dot{c}^a_\alpha \\ \dot{c}^c_\alpha \\ \dot{\eta}_\alpha \end{Bmatrix} \\ &= -\begin{bmatrix} (C_{m\alpha} + D_{m\alpha}) & E_{m\alpha} & F_{m\alpha} & (G_{m\alpha} - D_{mk}H_{kn}) \\ K_{m\alpha} & L_{m\alpha} & 0 & M_{m\alpha} \\ N_{m\alpha} & 0 & O_{m\alpha} & (P_{m\alpha} - N_{mk}H_{kn}) \\ -\delta_{m\alpha} & 0 & 0 & I_{m\alpha} \end{bmatrix} \begin{Bmatrix} b^a_\alpha \\ c^a_\alpha \\ c^c_\alpha \\ \eta_\alpha \end{Bmatrix} \\ &-\begin{bmatrix} Q_m \\ 0 \\ 0 \\ 0 \end{bmatrix}, \end{aligned} \tag{5.51}$$

or simply we can write

$$\dot{\mathbf{X}} = \mathbf{A}\mathbf{X} + \mathbf{B}, \tag{5.52}$$

where the coefficient matrices are:

$$\mathbf{A} = -\begin{bmatrix} (A_\alpha + B_\alpha)\,\delta_{m\alpha} & 0 & 0 & -B_m H_{m\alpha} \\ 0 & J_\alpha \delta_{m\alpha} & 0 & 0 \\ 0 & 0 & J_\alpha \delta_{m\alpha} & 0 \\ 0 & 0 & 0 & \delta_{m\alpha} \end{bmatrix}^{-1} \times$$

$$\begin{bmatrix} (C_{m\alpha} + D_{m\alpha}) & E_{m\alpha} & F_{m\alpha} & (G_{m\alpha} - D_{mk} H_{kn}) \\ K_{m\alpha} & L_{m\alpha} & 0 & M_{m\alpha} \\ N_{m\alpha} & 0 & O_{m\alpha} & (P_{m\alpha} - N_{mk} H_{kn}) \\ -\delta_{m\alpha} & 0 & 0 & I_{m\alpha} \end{bmatrix}$$

$$\mathbf{B} = -\begin{bmatrix} (A_\alpha + B_\alpha)\,\delta_{m\alpha} & 0 & 0 & -B_m H_{m\alpha} \\ 0 & J_\alpha \delta_{m\alpha} & 0 & 0 \\ 0 & 0 & J_\alpha \delta_{m\alpha} & 0 \\ 0 & 0 & 0 & \delta_{m\alpha} \end{bmatrix}^{-1} \begin{bmatrix} Q_m \\ 0 \\ 0 \\ 0 \end{bmatrix}. \quad (5.53)$$

The above wave evolution equations are linear, but have time-dependent coefficients because of the initial adjustment period for the basic flow. Thus, we are unable to use an eigenvalue analysis to obtain the wave growth rate. Only the time integration method is possible to investigate the instability.

## 5.4 Verification

The wave evolution equations obtained in the previous sections were integrated forward in time by the NAG routine D02PDF and the Numerical Recipes routine RK4 in Fortran [61]. We found the critical steady velocity such that the interface displacement just becomes unstable. When we use a typical cell shown in Chapter 5 with a single-eddy steady flow, the critical steady velocity of 0.23 m/sec is obtained (with two eddies, 0.24 m/sec). It is of the same order as those that are measured in industrial cells [85]. In order to minimise the numerical error, we use the integration step 0.05 sec in this thesis. The critical steady velocity is changed according to the integration step as follows:

| Integration step (sec) | Critcal steady velocity (m/sec) |
|---|---|
| 0.01 | 0.23 |
| 0.5 | 0.23 |
| 0.7 | 0.22 |
| 0.8 | 0.2 |
| 1.0 | 0.19 |

A detailed description of the scheme will be given in Chapter 6.

To verify our model and its implementation, we first will recover the natural frequencies for a cell under the gravity force by letting the steady flows be zero. These results will be compared with Urata's analytic calculation. Segatz (see [67], [65] and [66]) used a similar verification without Lorentz forces for his model.

Secondly, we check the total energy to confirm energy conservation and the energy exchange between the kinetic energy and the potential energy when there is no damping term.

Finally, we calculate the energy dissipation by the frictional damping in order to compare it with the total energy loss during the perturbation process.

### 5.4.1 Gravity wave period

It is well known that an internal gravity wave arises at the interface between two liquids having different densities. As the difference of both densities is small, the long period oscillation may be expected. By neglecting viscosity of both liquids and the electromagnetic forces, the period $T$ is derived from the dynamic equations as follows:

$$T = 2\pi \sqrt{\frac{\rho^a \coth(kh^a) + \rho^c \coth(kh^c)}{kg(\rho^a - \rho^c)}}, \tag{5.54}$$

where the wave number:

$$k = \sqrt{\frac{k_x^2}{a^2} + \frac{k_y^2}{b^2}}. \tag{5.55}$$

The above simple calculation indicates fairly good agreement with the observed periods in a real cell. The slight discrepancy is due to neglecting the effects of the electromagnetic forces, the basic steady flow of the liquid metal and cell geometry.

Using the above equations, the pure gravity wave period $T$ of a typical cell used in

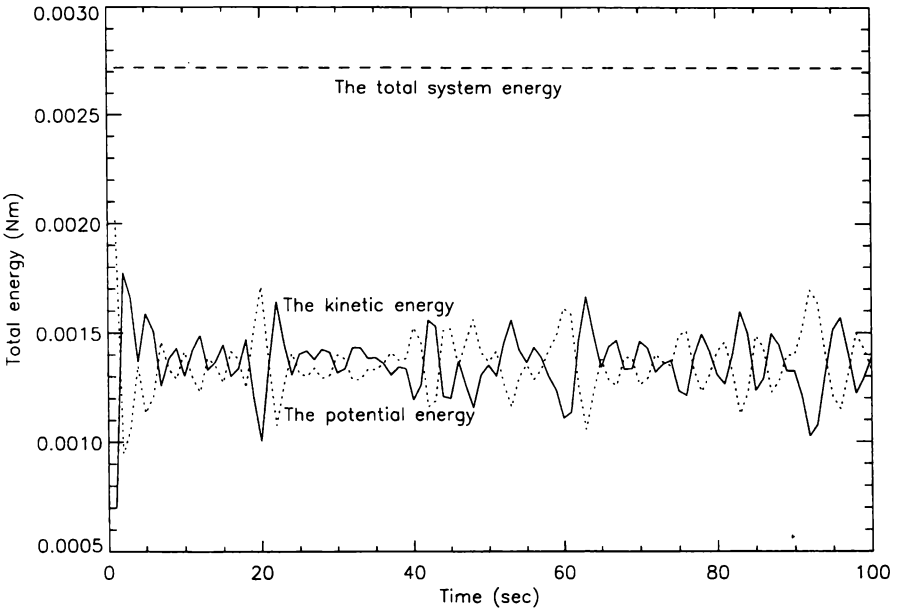


Figure 5.2: The total energy conservation, where $h_1 = 0.2$m, $h_2 = 0.04$m, $\rho_1 = 2270$kg/m, $\rho_2 = 2088$kg/m and the initial interface displacement $\eta_1 = \eta_2 ... = \eta_n = 0.001m$.

Chapter 6 is analytically estimated as follows:

$$\begin{aligned} T &= 2\pi\sqrt{\frac{\rho^a \coth(kh^a) + \rho^c \coth(kh^c)}{kg(\rho^a - \rho^c)}} \\ &= 2\pi\sqrt{\frac{2270\coth(1.03574\times 0.2) + 2088\coth(1.03574\times 0.04)}{1.03574\times 9.8(2270-2088)}} \\ &= 36.26, \end{aligned}$$

where the wave number $k$ of (1,1) mode is calculated by

$$\begin{aligned} k &= \pi\sqrt{\frac{k_x^2}{a^2} + \frac{k_y^2}{b^2}} \\ &= \pi\sqrt{\frac{1}{7.7^2} + \frac{1}{3.3^2}} \\ &= 1.03574. \end{aligned}$$

The period of 36.26 sec shows a good agreement with our numerical result 36.4 sec.

### 5.4.2 Energy conservation

In order to confirm energy conservation and the energy conversion between the kinetic and potential energy, we check the total energy at every calculation step

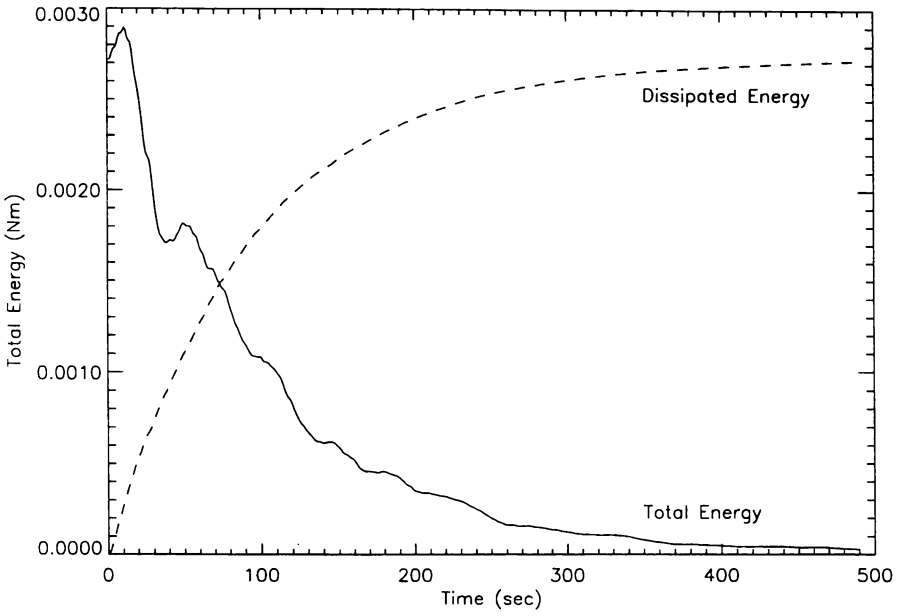


Figure 5.3: The energy dissipation by the frictional damping force, where $h_1$ = 0.2m, $h_2$ = 0.04m, $\rho_1$ = 2270kg/m, $\rho_2$ = 2088kg/m, $\alpha$=1 and the initial interface displacement $\eta_1 = \eta_2 ... = \eta_n$ = 0.001m. The steady velocity $U^a$ = 0.2m/sec, $U^c$ = 0.1m/sec and the initial adjustment period 10 sec for the basic steady flow are applied.

without any damping terms. Figure 5.2 shows the energy conservation during the perturbation with an initial disturbance.

### 5.4.3 Energy dissipation by the frictional damping force

The energy dissipation is also checked with the frictional damping term. We consider both the rotational and irrotational velocity terms. The total dissipated energy must be equal to the initial perturbation energy. The dissipation rate $R_d$ by the frictional damping force is written as follows:

$$\begin{aligned} R_d &= \int (k\mathbf{u}) \cdot \mathbf{u} dV \\ &= \int k\mathbf{u}_p \cdot \mathbf{u}_p dV + \int k\mathbf{u}_r \cdot \mathbf{u}_r dV + 2\int k\mathbf{u}_p \cdot \mathbf{u}_r dV, \\ &= \int k\mathbf{u}_p \cdot \mathbf{u}_p dV + \int k\mathbf{u}_r \cdot \mathbf{u}_r dV \\ &= R_p + R_r, \end{aligned} \tag{5.56}$$

where the inner product of the rotational and the irrotational term $\int k\mathbf{u}_p \cdot \mathbf{u}_r dV = 0$.

Then the dissipated energy $\Delta E_d$ is written as

$$\Delta E_d = \int R_d dt, \tag{5.57}$$

where the irrotational term $R_p$ and rotational term $R_r$ of the dissipation rate are calculated as

$$\begin{aligned} R_p &= k \int_V \mathbf{u}_p \cdot \mathbf{u}_p dV \\ &= k \int_V \nabla\phi \cdot \nabla\phi dV \\ &= k \int_V [\{\partial_z g_m(z)\}^2 + g_m(z)^2 \lambda_m^2] E_m^2 b_m^2 dV \\ &= k \int_z [\{\partial_z g_m(z)\}^2 + g_m(z)^2 \lambda_m^2] dz \int_\Gamma E_m^2 d\Gamma b_m^2 \\ &= k \int_z [\{\partial_z g_m(z)\}^2 + g_m(z)^2 \lambda_m^2] dz ||E_m||^2 b_m^2 \\ &= k\{\bar{g}'_{mm}(z) + \lambda_m^2 \bar{g}_{mm}(z)\} ||E_m||^2 b_m^2, \end{aligned} \tag{5.58}$$

$$\begin{aligned} R_r &= kh \int_V \mathbf{u}_r \cdot \mathbf{u}_r dV \\ &= kh \int_\Gamma (\nabla\psi \times \hat{\mathbf{z}}) \cdot (\nabla\psi \times \hat{\mathbf{z}}) d\Gamma \\ &= kh\lambda_m^2 \int_\Gamma |\psi|^2 d\Gamma \\ &= kh\lambda_m^2 ||H_m||^2 c_m^2. \end{aligned} \tag{5.59}$$

Figure 5.3 shows the initial perturbation energy and the energy dissipated by the frictional damping force. The initial perturbation energy should exactly equal the total energy dissipated during the frictional damping process. It is interesting to observe the energy increment during the initial transient period (10 seconds), as we gradually increase the steady velocity from zero to a constant value. Even after the transient period, we can observe occasional temporary energy increases. It seems to be the main reason that kinetic energy is transfered from the steady velocity field by the interfacial mechanism continuously. Thus, when the steady velocity is increased beyond the critical speed, the system will be unstable due to the kinetic energy transfer.

Figure 5.4 shows the basic steady flow configurations used in our numerical calculations. Unless otherwise specified, we use the basic flow configuration (1,1) in this thesis.

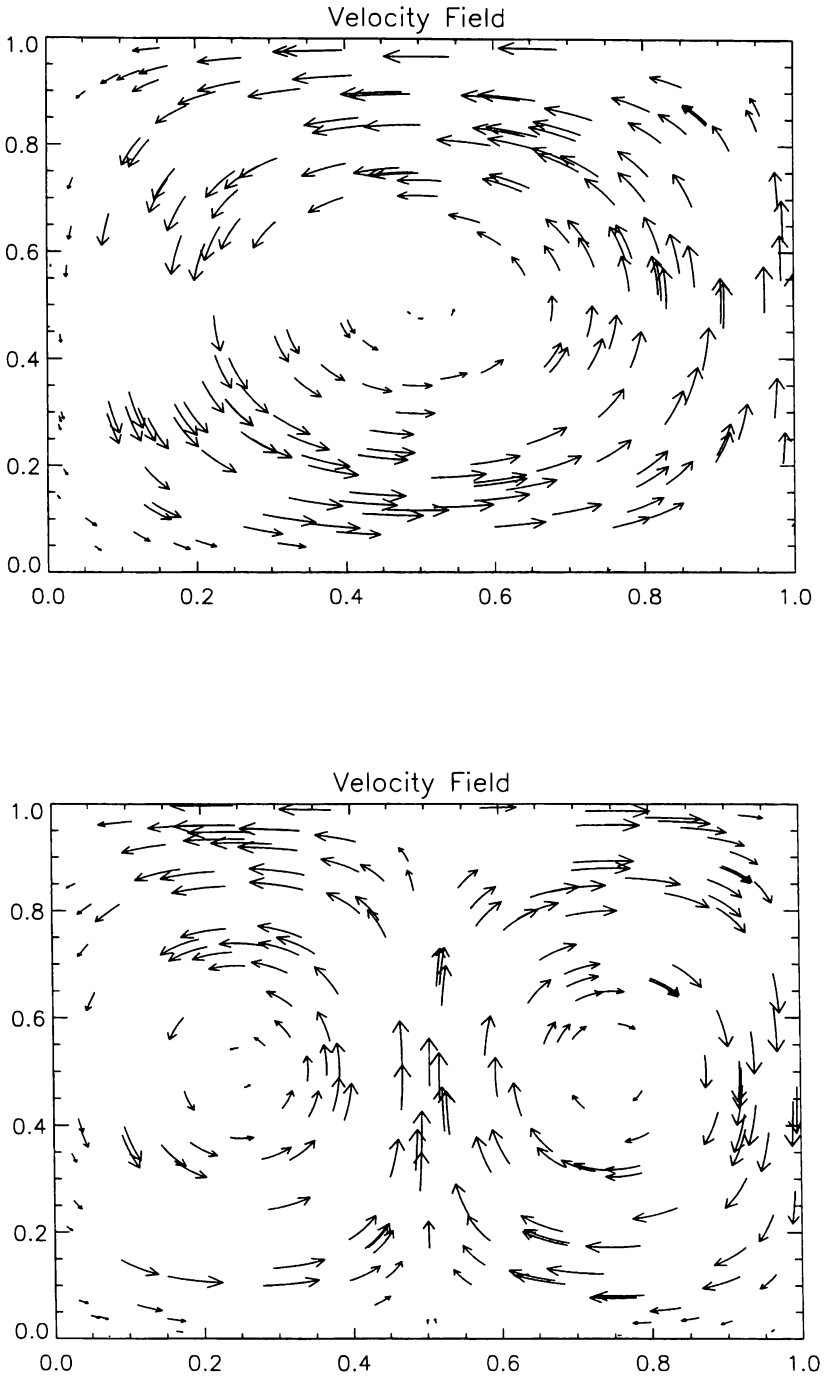


Figure 5.4: Basic flow configuration (1,1) with one eddy (top) and (2,1) with two eddies (bottom).

# Chapter 6

# The Kelvin-Helmholtz and pressure driven instabilities

The K-H instability has been previously discussed by some authors (see Moreau & Ziegler [52], Pigney [57] and Wang [83]). The steady velocity of the basic flow is a main concern in the above analyses, while other studies have been more concerned with instabilities driven by the electromagnetic fields, such as the current instability.

There exist strong circulation flows in the aluminium reduction cell, which are driven mainly by electromagnetic forces. The average velocity of the steady flows depends on the various cell design and operating parameters, and is normally about 0.1 - 0.2m/sec. It is much slower in the cryolite layer because of its relatively weak electrical conductivity and higher viscosity [83]. This give rise to a velocity discontinuity at the interface and the K-H instability.

In this chapter, we review a simplified K-H instability model, then discuss our model which is formulated with the normal mode method in Chapter 5. The former shows the K-H instability mechanism clearly in a two dimensional infinite cell, while we use the three dimensional cell model with vertical and lateral boundary conditions to be more realistic. Both models confirm that the magnitudes of the steady velocities, the ACD and cell geometry are crucial factors.

## 5.5 Conclusion

A coupled system of ordinary differential equations are formulated with the normal mode method and verified by reproducing the gravity wave mode and by confirming the energy conservation. In the next chapter, we shall investigate the dynamic behaviours of the interface in the view of the K-H instability mechanism by calculating the critical steady velocity with the simulation program formulated in this chapter.

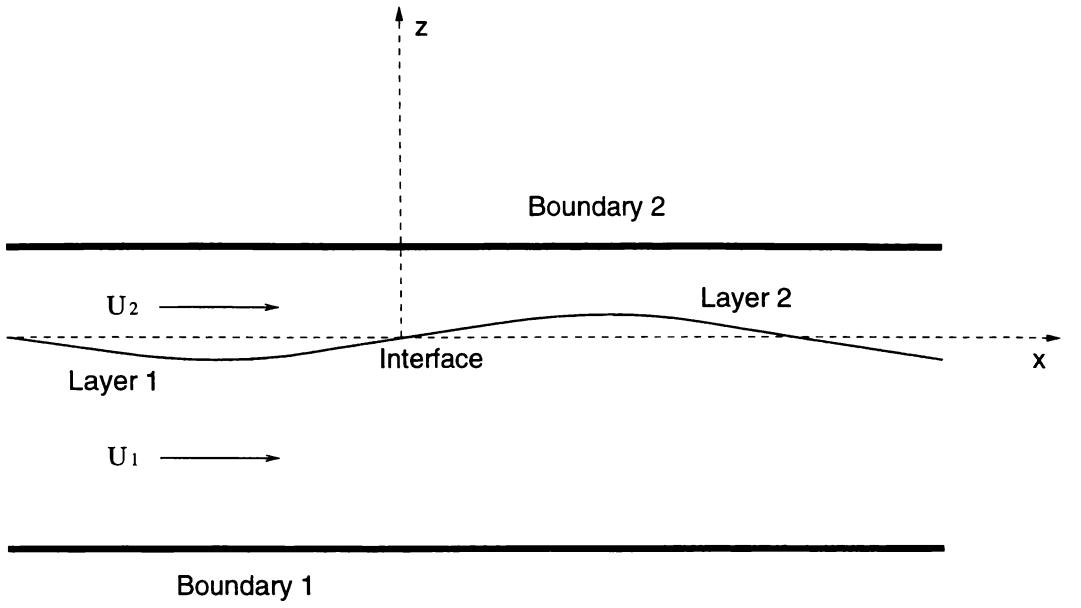


Figure 6.1: A simplified K-H instability model.

## 6.1 A simplified K-H instability model

We shall consider one dimensional flow in two liquid layers with the different horizontal velocities, which are bounded by parallel plane walls as shown in Figure 6.1. There is a discontinuity in the velocity at the interface $z = 0$. We assume an interface perturbation $\eta$ represented by

$$\begin{aligned} \eta &= \eta_o e^{\mathrm{i}\chi} \\ &= \eta_o e^{\mathrm{i}(lx-\omega t)}, \end{aligned} \tag{6.1}$$

where $\eta_o$ is a constant, $l$ is the horizontal wave number and $\omega$ is the angular frequency.

The linearised perturbation in each layer to the Navier-Stokes equation is

$$\rho_j \left( \frac{\partial \mathbf{u}_j}{\partial t} + U_j \partial_x \mathbf{u}_j \right) + k_j \mathbf{u}_j = \nabla p_j, \tag{6.2}$$

where the index $j$ represents the layer, $U_j$ denotes the basic steady flow, $k_j$ is the drag coefficient and $p_j$ is the pressure perturbation.

We assume $\mathbf{u}_j$ and $p_j$ to be proportional to $e^{\mathrm{i}\chi}$:

$$\mathbf{u}_j = u_j(z) e^{\mathrm{i}\chi} \hat{\mathbf{x}},$$

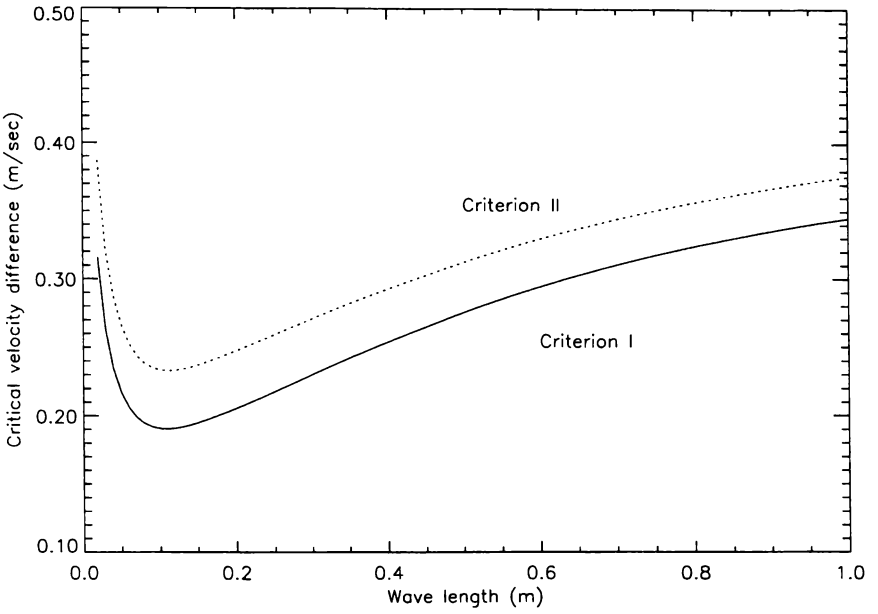


Figure 6.2: The critical velocity difference versus the wavelength, where $h_1 = 0.2$m, $h_2 = 0.04$m, $\rho_1 = 2270$kg/m, $\rho_2 = 2088$kg/m and $\alpha = 1.0$.

$$p_j = g_j(z)e^{\mathrm{i}\chi}. \tag{6.3}$$

By applying the following boundary conditions, $u_z = 0$ on the solid / liquid boundaries

$$\left(\frac{\partial p_1}{\partial z}\right)_{z=h_1} = 0,$$
$$\left(\frac{\partial p_2}{\partial z}\right)_{z=-h_2} = 0,$$

and the interface condition,

$$\begin{aligned} u_z &= \frac{D\eta}{Dt} \\ &= \frac{\partial \eta}{\partial t} + \mathbf{u}_j \cdot \nabla \eta \\ &= -\mathrm{i}\left(\omega - U_j l\right)\eta, \end{aligned} \tag{6.4}$$

to the above equation, we finally obtain the following two instability criteria in terms of the velocity difference $\Delta U$ at the interface [83]:

$$\Delta U^2 \geq \frac{\left(\rho_2 C_2 + \rho_1 C_1\right) \triangle\, \rho g l \left(k_2 C_2 + k_1 C_1\right)^2}{l^2 C_1 C_2 \left[C_1 C_2 \left(\rho^1 k_2\right)^2 + C_1 C_2 \left(\rho_2 k_1\right)^2 + \rho_1 \rho_2 \left(k_1 C_1\right)^2 + \rho_1 \rho_2 \left(k_2 C_2\right)^2\right]},$$

$$\Delta U^2 \geq \frac{4\left(\rho_2 C_2 + \rho_1 C_1\right) \triangle\, \rho g l + \left(k_2 C_2 + k_1 C_1\right)^2}{4 l^2 \rho_1 \rho_2 C_1 C_2}, \tag{6.5}$$

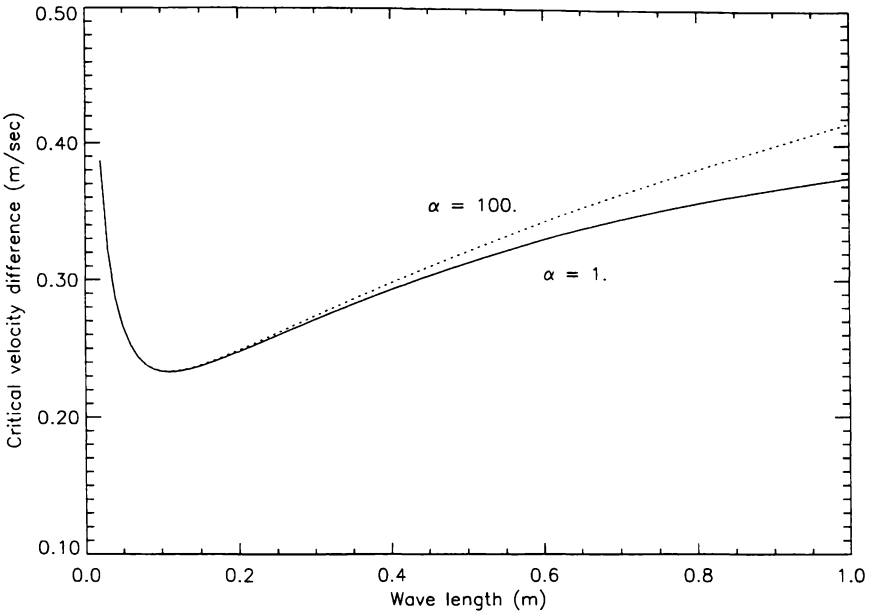


Figure 6.3: The critical velocity difference versus the wavelength for the second criterion with different drag coefficients, where $h_1 = 0.2$m, $h_2 = 0.04$m, $\rho_1 = 2270$kg/m, $\rho_2 = 2088$kg/m and $\alpha = 1$ or 100.

where

$$C_1 = \frac{\cosh(lh_1)}{\sinh(lh_1)}, C_2 = \frac{\cosh(lh_2)}{\sinh(lh_2)}.$$

Both criteria must be satisfied for a cell to be stable as shown in Figure 6.2. They show the K-H instability can occur even between the same liquid layers, when $\rho_1 = \rho_2$.

Normally, the first criterion is more important than the second. It is also interesting to observe that the first criterion does not depend on the drag coefficient greatly, while the second does as shown in Figure 6.3. Though this model is not enough for real applications, it shows the K-H instability mechanism very simply and clearly.

## 6.2 Normal mode method for the K-H instability in aluminium reduction cells

When we neglect the electromagnetic fields, the wave evolution equation can be written as follows:

$$\begin{bmatrix} (A_m + B_m)\,\delta_{m\alpha} & 0 & 0 & -B_m H_{m\alpha} \\ 0 & J_m \delta_{m\alpha} & 0 & 0 \\ 0 & 0 & J_m \delta_{m\alpha} & 0 \\ 0 & 0 & 0 & \delta_{m\alpha} \end{bmatrix} \begin{Bmatrix} \dot{b}^a_\alpha \\ \dot{c}^a_\alpha \\ \dot{c}^c_\alpha \\ \dot{\eta}_\alpha \end{Bmatrix}$$

$$= -\begin{bmatrix} (C_{m\alpha} + D_{m\alpha}) & E_{m\alpha} & F_{m\alpha} & (G_{m\alpha} - D_{mk} H_{k\alpha}) \\ K_{m\alpha} & L_{m\alpha} & 0 & M_{m\alpha} \\ N_{m\alpha} & 0 & O_{m\alpha} & (P_{m\alpha} - N_{mk} H_{k\alpha}) \\ -\delta_{m\alpha} & 0 & 0 & I_{m\alpha} \end{bmatrix} \begin{Bmatrix} b^a_\alpha \\ c^a_\alpha \\ c^c_\alpha \\ \eta_\alpha \end{Bmatrix}$$

$$-\begin{bmatrix} Q_m \\ 0 \\ 0 \\ 0 \end{bmatrix}, \tag{6.6}$$

where all the coefficients are the same as shown in Chapter 5.

The model developed in Chapter 5 is employed for the hydrodynamic instability in an aluminium reduction cell. Current perturbation effects are not included in this stage. As one of most important results in this research, two different hydrodynamic instability mechanisms will be introduced. The first mechanism, which was studied by Ziegler, shows that instability is possible even when the velocity difference = 0. This must be due to the density difference between two liquid layers, and seems to be generated from the steady pressure difference at the interface (see Section 5.2.4).

However, the second mechanism known as the K-H instability is due to the velocity difference between the liquid layers and is much stronger. It occurs between the liquid layers of the same density, if there is a steady velocity difference. The cell instability is determined by a complex interaction of both mechanisms. We include the above two mechanisms in our model. Various design and operation parameters such as ACD, liquid metal depth, cell length and steady flow pattern are investigated in this chapter.

### 6.2.1 Instability threshold

In Ziegler's work, the instability of a cell is measured by an alternative form of kinetic and potential energy of the system expressed in terms of the Fourier coefficients. The total perturbation energy is a useful indicator of instability growth when an initial disturbance is applied at the interface, which is affected by the steady velocity of the basic flow in the interfacial mechanism. The system can be perturbed without the initial disturbance because the initial pressure imbalance causes the interface to grow immediately. However, in our perturbation we apply the initial disturbance as it is necessary to check the critical velocity with an instability threshold.

The system is deemed unstable if the perturbation energy increases over the threshold during the simulation and stable if it decreases or does not change. Ziegler assumed a cell to be unstable if the energy is 100 times greater than that calculated from the initially given perturbation to the interface. The simplified energy form was evaluated using square terms of all the coefficients. The initial perturbation was applied to the interface displacement $\eta$, not to the velocity fields.

In our model, we are going to take a slightly different formulation from Ziegler's. We calculate the exact values of the perturbation kinetic energy $\Delta KE$ and the potential energy $\Delta PE$ for the irrotational velocity, the rotational velocity and the interface displacement terms as follows:

$$\begin{aligned}
\Delta KE &= \int_V \rho\{(\mathbf{U}+\mathbf{u})\cdot(\mathbf{U}+\mathbf{u}) - \mathbf{U}\cdot\mathbf{U}\}dV \\
&= \rho\int_V (2\mathbf{U}\cdot\mathbf{u} + \mathbf{u}\cdot\mathbf{u})dV \\
&= \rho\int_V \{2\mathbf{U}\cdot(\mathbf{u}_p+\mathbf{u}_r) + \mathbf{u}_p\cdot\mathbf{u}_p + 2\mathbf{u}_p\cdot\mathbf{u}_r + \mathbf{u}_r\cdot\mathbf{u}_r\}dV. \qquad (6.7)
\end{aligned}$$

As $\int_V \mathbf{u}_p\cdot\mathbf{u}_r dV = \int_V \mathbf{U}\cdot\mathbf{u}_p dV = 0$ in the above equation, when we take a steady flow $\mathbf{U} = U_k\nabla H_k \times \hat{\mathbf{z}}$, we have

$$\begin{aligned}
\Delta KE &= \rho\int_V (2\mathbf{U}\cdot\mathbf{u}_r + \mathbf{u}_p\cdot\mathbf{u}_p + \mathbf{u}_r\cdot\mathbf{u}_r)dV \\
&= \rho 2U_k c_k \int_V \nabla H_k\cdot\nabla H_k dV + \Delta KE_p + \Delta KE_r \\
&= \rho 2U_k h c_k \int_\Gamma \nabla H_k\cdot\nabla H_k d\Gamma + \Delta KE_p + \Delta KE_r \\
&= \rho 2U_k h\lambda_k^2 ||H_k||^2 c_k + \Delta KE_p + \Delta KE_r, \qquad (6.8)
\end{aligned}$$

where the kinetic energy perturbation terms for the irrotational and the rotational

velocity are written as

$$\begin{aligned}
\Delta KE_p &= \rho \int_V \mathbf{u}_p \cdot \mathbf{u}_p dV \\
&= \rho \int_V \nabla\phi \cdot \nabla\phi dV \\
&= \rho \int_V [\{\partial_z g_\alpha(z)\}^2 + g_\alpha(z)^2 \lambda_\alpha^2] E_\alpha^2 b_\alpha^2 dV \\
&= \rho \int_z [\{\partial_z g_\alpha(z)\}^2 + g_\alpha(z)^2 \lambda_\alpha^2] dz \int_\Gamma E_\alpha^2 d\Gamma b_\alpha^2 \\
&= \rho \int_z [\{\partial_z g_\alpha(z)\}^2 + g_\alpha(z)^2 \lambda_\alpha^2] dz ||E_\alpha||^2 b_\alpha^2, \qquad (6.9)
\end{aligned}$$

$$\begin{aligned}
\Delta KE_r &= \rho \int_V \mathbf{u}_r \cdot \mathbf{u}_r dV \\
&= \rho h \int_\Gamma (\nabla\psi \times \mathbf{z}) \cdot (\nabla\psi \times \mathbf{z}) d\Gamma \\
&= \rho h \lambda_\alpha^2 \int_\Gamma |\psi|^2 d\Gamma \\
&= \rho h \lambda_\alpha^2 ||H_\alpha||^2 c_\alpha^2. \qquad (6.10)
\end{aligned}$$

$$\begin{aligned}
\Delta PE &= (\rho^a - \rho^c) g \int_V \eta dV \\
&= (\rho^a - \rho^c) g \int_\Gamma \int_\eta \eta d\eta d\Gamma \\
&= \frac{1}{2} (\rho^a - \rho^c) g \int_\Gamma \eta^2 d\Gamma \\
&= \frac{1}{2} (\rho^a - \rho^c) g \int_\Gamma E_\alpha^2 d\Gamma \eta_\alpha^2 \\
&= \frac{1}{2} (\rho^a - \rho^c) g ||E_\alpha||^2 \eta_\alpha^2. \qquad (6.11)
\end{aligned}$$

Thus we have the total perturbation energy $\Delta E$ as:

$$\Delta E = \Delta KE + \Delta PE, \qquad (6.12)$$

while Ziegler took a pseudo-energy term which is roughly approximated from the wave evolution coefficients to simplify the calculation [85]. His energy term is a little far from the exact value of the perturbation energy.

In our simulations, we adopt Ziegler's threshold and assume a cell to be unstable if the perturbation energy $\Delta E$ is 100 times greater than that of the initial perturbation. The initial perturbation of $10^{-3}$m is given only to all the coefficients associated with the interface displacement $\eta$ ($\eta_1 = \eta_2 = ...\eta_n = 0.001$m) while others are assumed

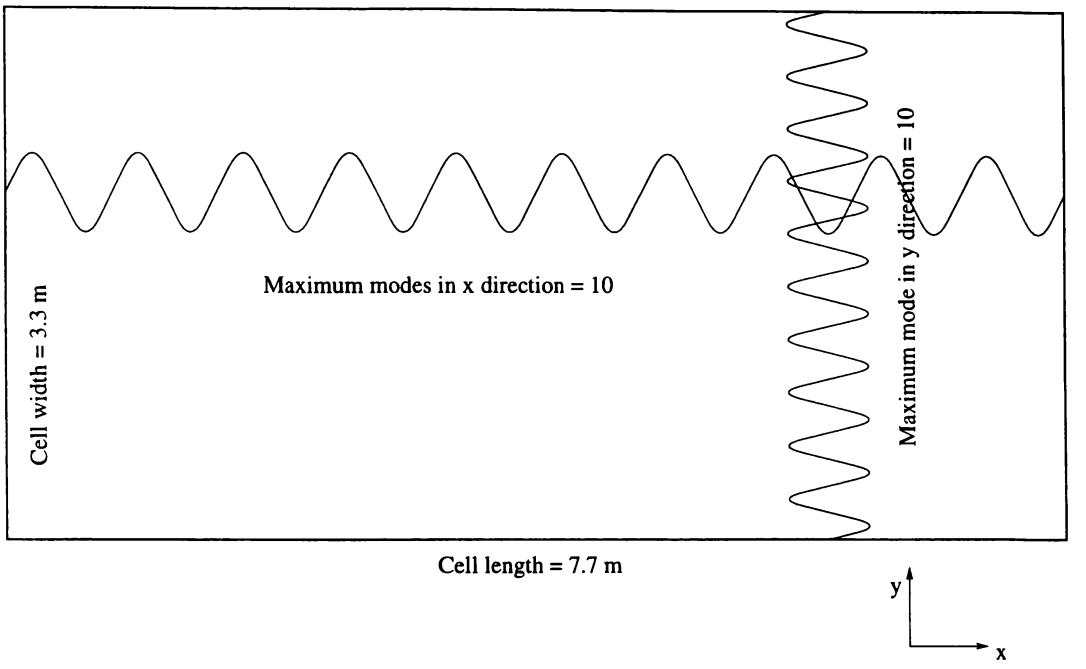


Figure 6.4: Maximum number of mode in each direction.

zero ($b_1 = b_2 = ...b_n = 0$ and $c_1 = c_2 = ...c_n = 0$). If the perturbation energy is 100 times less than that calculated from the initially given perturbation to the interface or the simulated time exceeds 1.5 hours without the above divergence occurring, the system is considered to be stable. According to our simulation, Ziegler's assumption for the instability threshold of 100 times greater or less than the initial perturbation energy looks reasonable, since the critical velocity is quite insensitive to the value of this threshold. Using a threshold value of 500 or reducing it to 20 makes no measurable difference.

When the configuration is stable, the steady velocity is incremented, the initial conditions reset and the process repeated in Ziegler's calculation. However, in order to find the critical steady velocity more conveniently, we use a bisection method in our simulations. We use an initial interval [0.1, 0.4] m/sec for the steady velocities and bisect until the error is less than $10^{-3}$m/sec. Thus we can simply vary the parameters gradually to plot the relationship to the critical steady velocity.

### 6.2.2 Wave modes

In Chapter 5 we derived the following wave evolution equations:

$$\dot{\mathbf{X}} = \mathbf{A}\mathbf{X} + \mathbf{B}, \tag{6.13}$$

which are solved by the NAG routine D02PDF or the Numerical Recipes RK4 [61]. The elements of the matrix **A** and **B** are listed in Chapter 5. The wave Fourier expansion is truncated to 120 modes in total from 0 to 10 in the $x$-direction and from 0 to 10 in the $y$-direction respectively, as shown in Figure 6.4. The mode (0,0) is not included. The higher frequency waves are quickly dissipated by viscosity, so do not affect the long period stability seriously. However, generally speaking, the more wave modes we take in each direction, the greater opportunity for cell instability. Thus we would expect the critical steady velocity to decrease somewhat as the number of modes increases.

The following table shows the critical steady velocity vs. number of modes in a reduction cell:

| Number of modes | Critical steady velocity |
|---|---|
| 24 | 0.228m/sec |
| 48 | 0.227m/sec |
| 63 | 0.227m/sec |
| 80 | 0.227m/sec |
| 99 | 0.227m/sec |
| 120 | 0.226m/sec |
| 224 | 0.226m/sec |

It is interesting to observe that the above result shows that high frequency waves less than a wavelength of 1m do not affect the K-H instability significantly.

### 6.2.3 Cell dimension and operation parameters

The cell dimension and operation parameters used in this thesis are as follows, unless specified otherwise:

| | |
|---|---|
| Cell length | $a = 7.7\text{m}$ |
| Cell width | $b = 3.3\text{m}$ |
| Anode-cathode distance | $ACD = 0.04\text{m}$ |
| Aluminium liquid depth | $h^a = 0.2\text{m}$ |
| Density of aluminium | $\rho^a = 2270\text{kg/m}^2$ |
| Density of cryolite | $\rho^c = 2088\text{kg/m}^2$ |
| Drag coefficient | $\alpha = 1$ |
| Basic flow configuration | (1,1) or (2,1) |

### 6.2.4 Steady flow pattern

Ziegler (1993) took the steady flows in both the aluminium and cryolite layer as expressed by the following stream function:

$$\psi = \psi_o \sin\left(\frac{k_x \pi x}{a}\right) \sin\left(\frac{k_y \pi y}{b}\right),$$

where $k_x$ and $k_y$ are positive integers which determine the number of steady eddies in a cell in the $x$ and $y$ direction respectively. As his analysis assumes that both the layers have the identical velocity fields,

$$\psi_o^c = \psi_o^a, \tag{6.14}$$

no K-H instability is present.

Wang (1996) also assumed identical flow patterns but of different magnitudes, taking

$$\begin{aligned} \psi_o^c &= r_d \psi_o^a \\ &= \frac{1}{2}\psi_o^a. \end{aligned} \tag{6.15}$$

The exact value of the velocity difference ratio $r_d$ is difficult to measure in real cell. Wang's assumption [83] is based on the fact that the velocity field in the cryolite layer is much smaller than that in the aluminium layer. The discontinuity in the velocity fields at the interface will give rise to a K-H instability when $\psi_o$ attains a certain critical value.

We adopt Wang's assumption $r_d = \frac{1}{2}$ unless otherwise indicated. The effect of the velocity difference on the critical steady velocity is shown in Figure 6.5. We hold $\psi^a$ constant so that

$$\psi^a - \psi^c = \psi^a(1 - r_d)$$

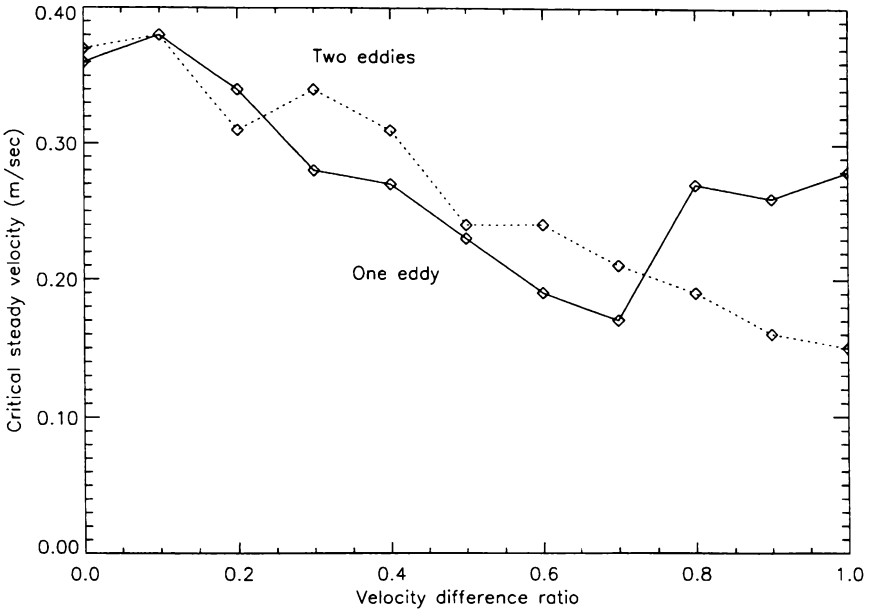


Figure 6.5: The critical steady velocity versus the velocity difference ratio $r_d$ in an aluminium reduction cell, where a=7.7m, b=3.3m, $h_a$=0.2m, ACD=0.04m and the initial interface displacement $\eta_1$=$10^{-4}$m is applied.

and the velocity difference varies from $\psi^a$ to 0 as $r_d$ increases. Hence generally K-H instability decreases with $r_d$. The one-eddy curve shows the K-H instability between $r_d = 0.7$ and $r_d = 1.0$. However, the two-eddies curve does not leap up near $r_d = 1$. That is not easy to explain because of some complicated interaction with the pressure-driven instability.

We also impose a gradual acceleration of the steady flow in order to avoid an initial pressure difference between the liquid interface due to the steady velocities of both the layers. The steady velocity becomes constant after the initial acceleration for $t_0$=10 seconds as shown in Figure 5.1. We apply the perturbation to an initial equilibrium state, which is theoretically very important in our instability analysis (see Section 5.2.2).

## 6.3 Operation and design parameters

In this section, we discuss effects of some operation and design parameters in the aluminium reduction process. Notwithstanding our complicated formulation of the

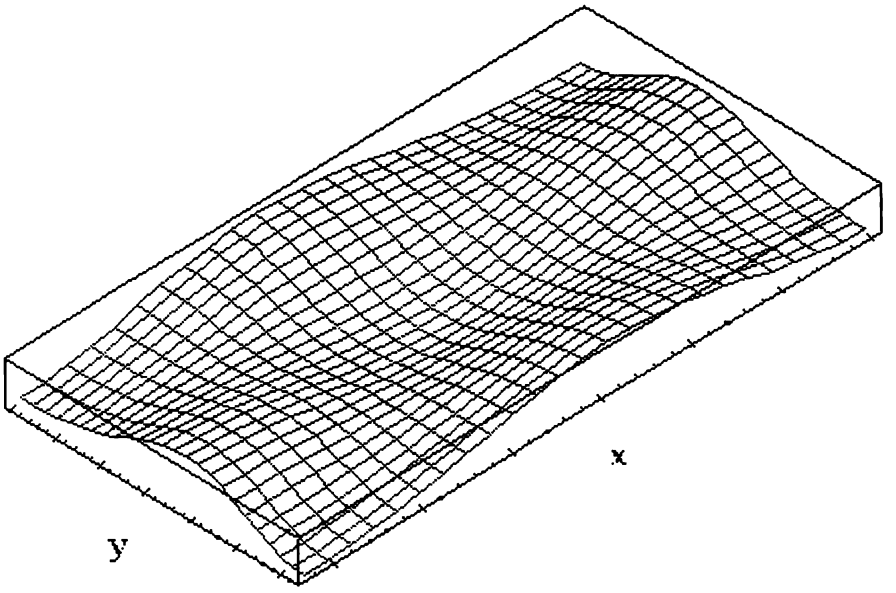


Figure 6.6: A typical interface displacement under a one-eddy basic flow

wave evolution equations, the numerical simulation results give us reasonable predictions for the interfacial instability, which are mostly found to be physically realistic. A typical interface displacement under one eddy basic flow is shown in Figure 6.6.

### 6.3.1 Steady velocity of the basic flow

One of the most important factors in the hydrodynamic cell instability is the basic steady velocity driven by the electromagnetic forces. It is obvious that generally the higher steady velocity differences make the system more unstable, as they will generate more pressure difference at the interface. However, the instability is not linearly dependent on the steady velocity, as shown in Figure 6.5. Although it is hard to explain simply because of some complicated interaction with the pressure-driven instability, the system becomes more unstable with the greater kinetic energy (i.e. $r_d = 1.0$) applied to the steady flow, especially in case of one eddy. The opposite trends in the curves seems to be due to the velocity difference, when K-H instability is dominant against other mechanisms.

We can also confirm the existence of Ziegler's instability mechanism when $r_d = 1$ in Figure 6.4. When the circulation of the basic flow is stirred by the electromagnetic forces, it is well-known that the interaction between $B_z$, $j_z$ and $j_y$ provides the main

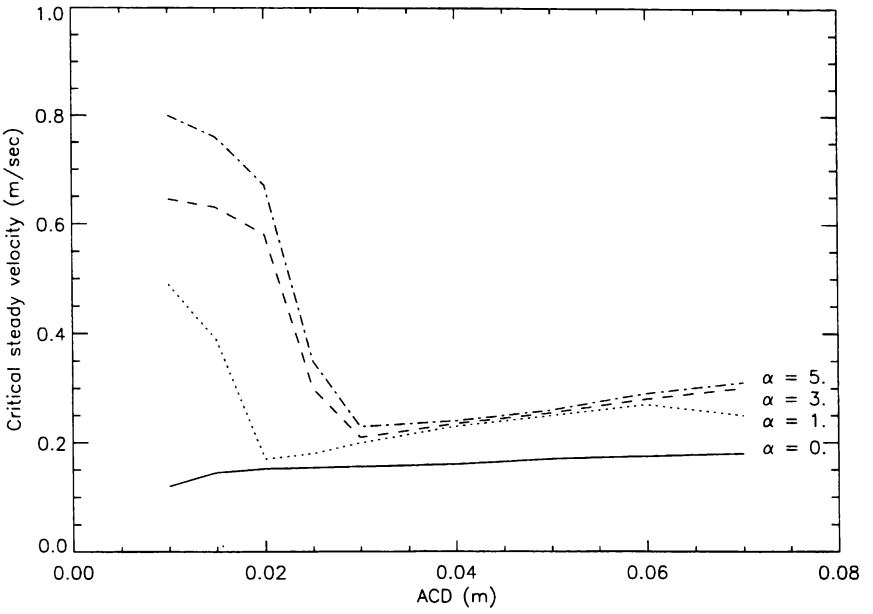


Figure 6.7: The critical steady velocity $U_c$ versus the ACD with different drag coefficients $\alpha$, with a one-eddy basic flow. Here a=7.7m, b=3.3m and $h_a$=0.2m.

driving source. Thus, in order to reduce the steady velocity, the vertical magnetic component $B_z$ must be minimised during the cell operation. It goes without saying that this result coincides with most previous MHD analyses also.

The critical steady velocity $U_c$ for onset of instability is clearly sensitive to the magnitude of the velocity discontinuity $\Delta U$, but there does not appear to be a simple relation between them. Moreover $U_c$ cannot be determined easily in real cells since there is no obvious way of controlling the steady induced velocity fields. Also an approximate calculation from the dynamic equations does not guarantee the result as well. Thus, the empirical data should be carefully checked with the simulation results and adjusted properly.

### 6.3.2 Effect of ACD

It is often observed that cells tend to become more stable when the ACD is increased [83] and our predictions generally follow this trend. It is common for a cell system to become stable as the ACD increases between 0.03m - 0.07m in our model as shown in Figures 6.7 and 6.8, which agrees with previous observations [83] very well.

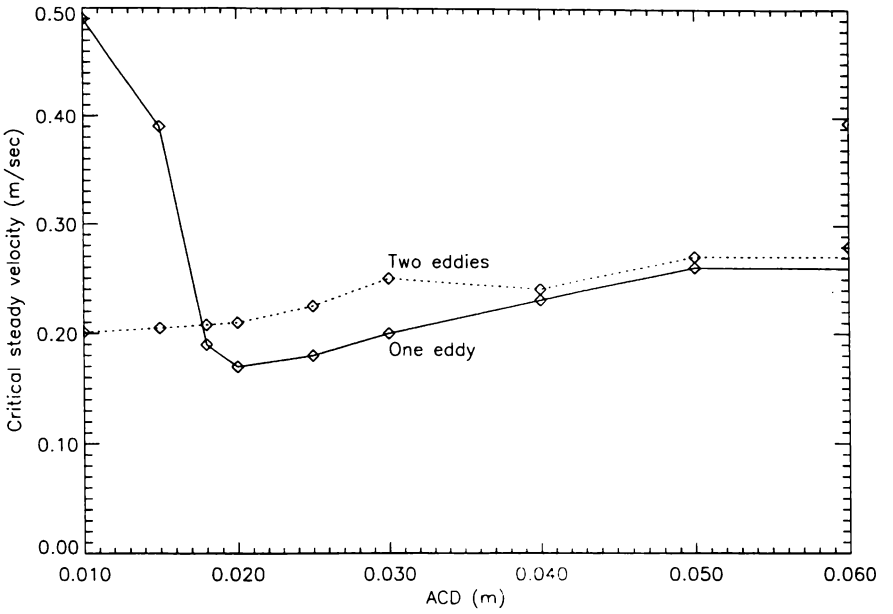


Figure 6.8: The critical steady velocity $U_c$ versus the ACD with different basic flow configurations in an aluminium reduction cell, where a=7.7m, b=3.3m, $h_a$=0.2m, ACD=0.04m and the initial interface displacement $\eta_1$=$10^{-4}$ m.

However, the system will be more stable as the ACD decreases below 0.03m, because the frictional damping force increases with decreasing depth, being proportional to $1/h$ in Moreau's model. If we assume no frictional damping force ($\alpha = 0$), the critical velocity decreases continuously as the ACD decreases (see Figure 6.7). Therefore, the simple application of the frictional drag coefficient can produce an unrealistic damping force in our simulation, especially in the range of the ACD under 0.03m.

Ziegler's result in Figure 2.2 shows this mechanism very clearly, which is contradictory to the usual observations and measurements [38]. As his model neglects the vertical velocity field, only the effect of the frictional drag force seems to be reflected in the change in ACD. Our model explains both the usual observations and the Ziegler's result together.

In practice, the ACD is usually around 0.04 m. Unfortunately, we find that it is not the optimum value for cell stability as shown in Figure 6.7. If we are able to take this to 0.03m, the system will become more unstable. However, as we reviewed earlier, if we reduce the ACD too much, the electrical short will occur between the anode and the liquid flow, which must be the first thing to avoid in cell operation. If we increase the ACD vice versa, it will cost too much electrical power normally. No

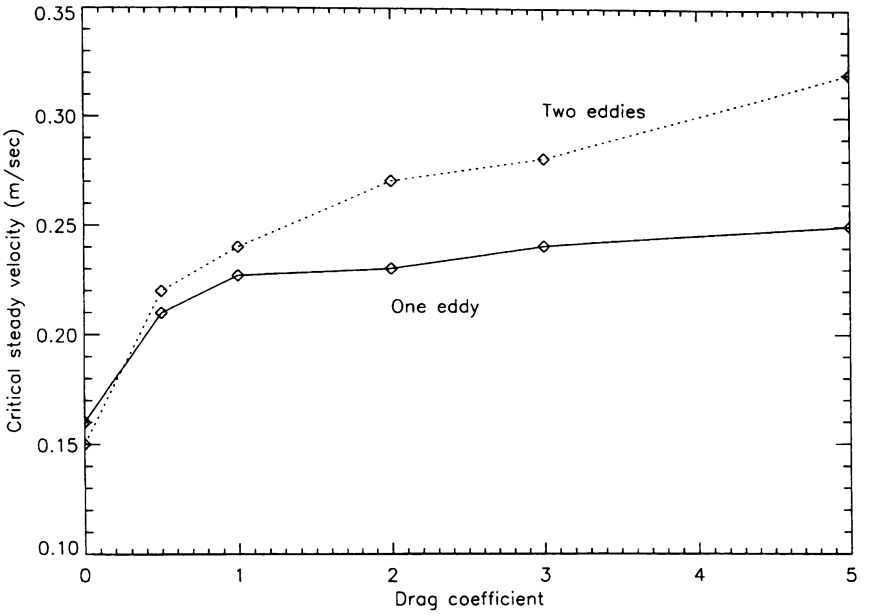


Figure 6.9: The critical steady velocity $U_c$ versus the drag coefficient $\alpha$ in an aluminium reduction cell, where a=7.7m, b=3.3m, $h_a$=0.2m, ACD=0.04m and the initial interface displacement $\eta_1$=$10^{-4}$m.

doubt the ACD is the most important and sensitive factor among the cell operation parameters, which should be determined not only by cell instability, but also by electric power economy.

### 6.3.3 Effect of frictional drag

The frictional drag force is one of the main factors in reducing the cell instability. As is usual, the higher damping force makes the system more stable. Unfortunately, in real applications, there is no practical way to maximize the frictional drag as it depends on the liquid viscosity and turbulence, although it is slightly related to the ACD, the steady velocity and the cell dimension.

It is interesting to observe that at a certain steady velocity, the system still remains stable even without any drag force as shown in Figure 6.9. Also it shows the system will become less stable unless there is a frictional drag force.

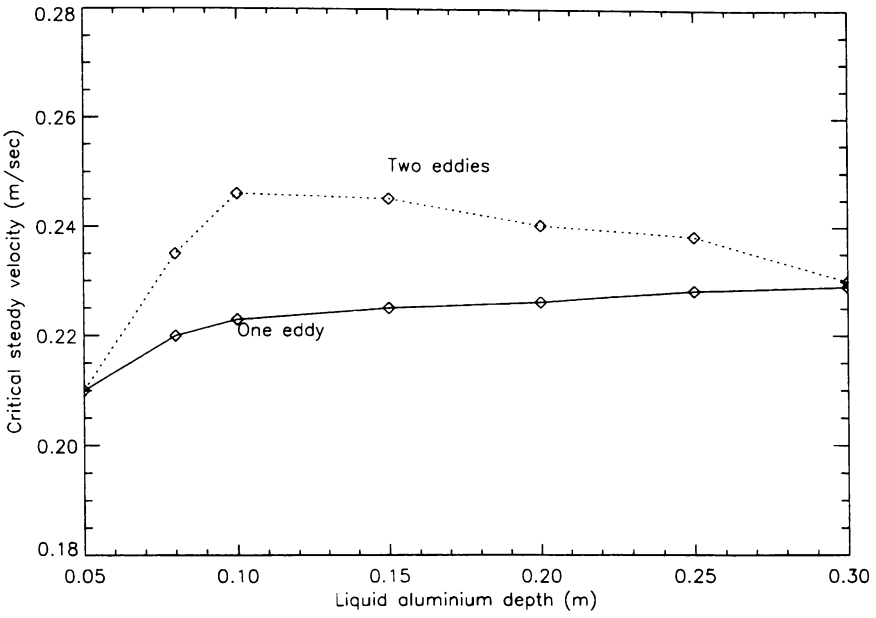


Figure 6.10: The critical steady velocity $U_c$ versus the liquid aluminium depth in an aluminium reduction cell, where a=7.7m, b=3.3m, ACD=0.04m and the initial interface displacement $\eta_1$=$10^{-4}$m.

### 6.3.4 Liquid aluminium depth

The liquid aluminium depth is also one of the factors, which affects cell instability, particularly in the range between 0.15m - 0.25m as shown in Figure 6.10. Normally the aluminium depth is about 0.2m in real cells.

### 6.3.5 Cell length

The cell length also affects $U_c$ and determines the natural frequencies of interfacial gravity waves, as reviewed in Chapter 2. It is interesting to find that the cell length affects the K-H/pressure instability very little in the case of a one-eddy flow, as shown in Figure 6.11.

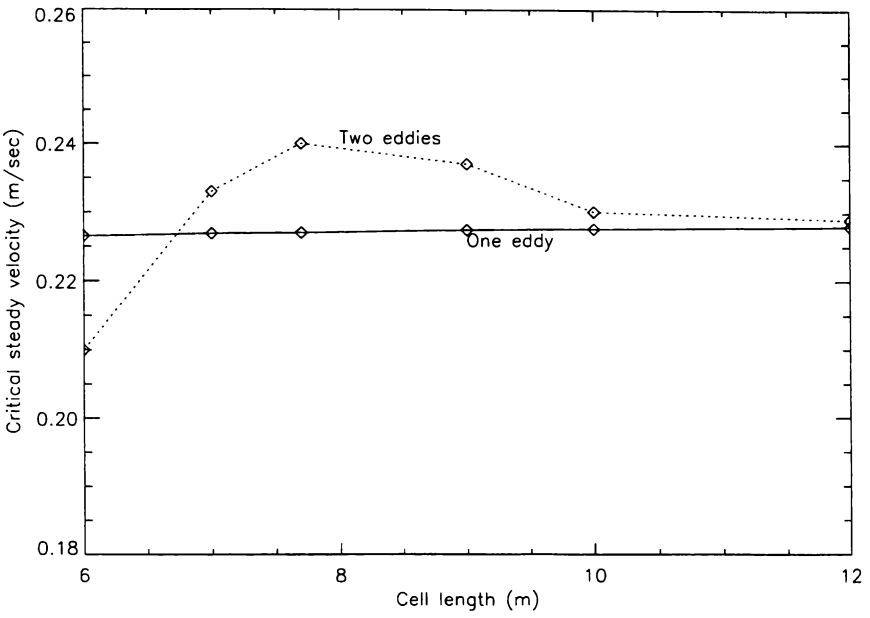


Figure 6.11: The critical steady velocity $U_c$ versus the cell length, where b=3.3m, $h_a$=0.2m, ACD=0.04m and the initial interface displacement $\eta_1$=$10^{-4}$m.

### 6.3.6 Basic steady flow configurations

The basic flow configuration is one of the major factors affecting cell stability, as shown in Ziegler's work. The following table summarises the relationship between $U_c$ and the steady flow pattern.

| No. of eddies | Basic flow | $U_c$(m/sec) |
|---|---|---|
| 1 | (1,1) | 0.23 |
| 2 | (2,1) | 0.24 |
| 2 | (1,2) | 0.12 |
| 4 | (2,2) | 0.08 |

The system is dramatically more unstable for the (1,2) and (2,2) flows. Generally speaking, the system will become more unstable, the more eddies of the basic steady flow.

According to the basic flow configuration, the effect of other cell parameters such as the ACD, frictional drag, liquid aluminium depth and cell length is varied as shown in the previous sections. Especially, the ACD is affected by the steady flow pattern significantly in the range under 0.02m (see Figure 6.8).

### 6.3.7 Ziegler's work ($U^a = U^c$) and the K-H instability ($U^a \neq U^c$)

We calculated the critical steady velocity with the same dimensions and operation parameters as used by Ziegler in our model as follows:

| Steady Flow Configuration | modes | Ziegler's results | Our results |
|---|---|---|---|
| (1,1) | 8×8 | 0.43m/sec | 0.12m/sec |
| (2,1) | 6×6 | 0.16m/sec | 0.12m/sec |

The above results show that Ziegler's calculation cannot detect some instabilities which ours can. One of the main difference is due to the vertical velocity field, which he ignored. Another problem is that his numerical integration begins with an unbalanced pressure difference at the interface.

## 6.4 Conclusion

The K-H instability always occurs with the velocity difference between the liquid layers. We can find the K-H mechanism as shown in Figure 6.5. The critical steady velocity does not linearly depend on the velocity difference, because of the complicated interaction of the pressure difference between two liquid layers. We include both the K-H and the pressure difference effects in our analysis.

In the K-H instability mechanism, the steady velocity difference of the basic flow generates the kinetic energy at the interface. Due to this mechanism with the other design and the operating parameters in the cells, the interfacial instability has always been a challenge.

In most cases, the steady velocity in aluminium layer is much greater than that in cryolite layer. Wang [83] assumed the value of the aluminium steady velocity twice greater than that of the cryolite velocity, $U_c = \frac{1}{2}U_a$ in his analysis. As a matter of fact, Ziegler's result does not seem to occur in real cell operations although it is assumed theoretically. The steady velocity in the aluminium layer is always greater than that in the cryolite layer. Thus, we find that the K-H instability is one of the most destabilising mechanisms in aluminium reduction cells.

We estimated the critical steady velocity with various cell operation and design parameters in our K-H instability model. It is shown that the ACD, the frictional drag coefficient, the liquid aluminium depth, the cell length and the basic flow configurations are the main parameters affecting stability. Among them, the ACD is a dominant and sensitive parameter in real cell operation, as the other parameters are not so simple to control.

The K-H instability mechanism shows that a cell system can become more unstable even when we reduce the steady velocity in cryolite layer while the aluminium layer

maintains the original velocity, because the velocity difference is increased. Thus, the simple reduction of the cryolite velocity does not help a cell system become more stable. This is one of interesting results in our study. Because the steady velocity in aluminium layer is always greater than that in cryolite layer, the hydrodynamic coupling mechanism in spite of its complexity guides us to the following conclusion. The steady velocity in aluminium layer must be minimised during the reduction process in order to control the cell instability properly.

# Chapter 7

# Induced magnetic damping

In this chapter, we explore a method of incorporating induced electric currents into our model. The main effect of the induced currents is to damp the instability. In a mean flow, the induced magnetic force can be as large as 40% of the imposed magnetic force according to previous research [35]. The induced current is driven by the EMF caused by the conducting fluid flowing across magnetic field lines. The kinetic energy is converted to electric energy via Ohmic dissipation of the induced currents. Thus, this force acts as a damping source by dissipating the kinetic energy.

In the first section, the general features of induced magnetic damping will be briefly introduced. In the second section, we will consider magnetic damping of surface waves for liquid metal in a rectangular insulating container. The aim is to study induced magnetic damping in a simple situation to illustrate some important features. In the third section, we study the same problem, but in a perfectly conducting container, to illustrate the importance of the container conductivity. Finally, in the last section we re-calculate the critical steady velocity with magnetic damping included.

## 7.1 Introduction

As we reviewed in Chapter 1, liquid aluminium flows are predominantly driven by the strong magnetic forces which can be calculated from the magnetic fields and the electric currents flowing in the metal pad. In a real cell, apart from the electric currents imposed on the cell through the anodes, the metal motion in the magnetic fields induces extra currents in the pad. If the cell boundaries are insulating, electric charge may accumulate and create the induced electric field which partly counteracts the imposed electric field.

Thus the magnetic forces consist of two parts: one due to the imposed currents and the other due to the induced currents. Thus we can decompose the current density in terms of the imposed currents $\mathbf{J}_o$ and the induced current $\mathbf{J}_I$ which consists of

the induced term $\sigma\mathbf{u} \times \mathbf{B}$ and the induced current potential term $\varphi$ as follows:

$$\begin{aligned} \mathbf{J} &= \mathbf{J}_o + \mathbf{J}_I \\ &= \mathbf{J}_o + (\sigma\mathbf{u} \times \mathbf{B} + \nabla\varphi). \end{aligned} \tag{7.1}$$

It is essential to include the induced electric potential $\nabla\varphi$, which represents a back electromagnetic force [83] necessary to satisfy the lateral boundary condition $\mathbf{J} \cdot \mathbf{n} = 0$ where the cell boundary is insulated. Actually the cell boundary is conducting, but since carbon is a much poorer conductor than aluminium we treat it as insulating. Here we assume shallow layer, so the vertical velocity component is much smaller than the horizontal velocity components. We also assume a well-mixed layer so that the velocity is independent of $z$. Also the induced current $\mathbf{J}$ will have only horizontal components (see Section 7.2.5).

Using the conservation of the induced current $\nabla \cdot \mathbf{J}_I = 0$ and the electromagnetic boundary condition, we have equations for the induced electric potential $\varphi$ as follows:

$$\nabla^2\varphi = -\sigma\nabla \cdot (\mathbf{u} \times \mathbf{B}), \tag{7.2}$$

$$\frac{\partial\varphi}{\partial n} = -\sigma\hat{\mathbf{n}} \cdot (\mathbf{u} \times \mathbf{B}) \text{ on all the boundaries.} \tag{7.3}$$

The second equation indicates that no induced current escapes from the liquid metal because the aluminium is much better electrical conductor than its surrounding material. The induced current potential $\varphi$ can be calculated numerically for given velocity $\mathbf{u}$ and magnetic fields $\mathbf{B}$ from the above Poisson equation.

Generally, the $\nabla\varphi$ term tends to oppose the induced force term $\mathbf{u} \times \mathbf{B}$ in order to cancel the normal component at the boundary. Considering only $\sigma\mathbf{u} \times \mathbf{B}$ as the induced current density and neglecting the effect of $\nabla\varphi$ will probably overestimate the damping effects of the induced current density [83].

The Lorentz force $\mathbf{f}$ takes the following form:

$$\begin{aligned} \mathbf{f} &= \mathbf{J} \times \mathbf{B} \\ &= \mathbf{J}_o \times \mathbf{B} + [\sigma(\mathbf{u} \times \mathbf{B}) + \nabla\varphi] \times \mathbf{B}. \end{aligned} \tag{7.4}$$

The induced magnetic force is strong in the aluminium layer while the turbulent drag force dominates it in the cryolite layer because $\sigma^a \gg \sigma^c$. Thus, in our formulation, the induced magnetic damping term will be considered only in aluminium layer.

## 7.2 Induced magnetic damping of free-surface waves in an insulating container

To simplify the physical problem, first we shall consider the induced magnetic damping in an insulating rectangular container as shown in Figure 7.1. This analysis assumes a shallow layer and $\mathbf{B} = B_z\hat{\mathbf{z}}$ for simplicity. The purpose of the following section is to illustrate the crucial influence of the conductivity of the container.

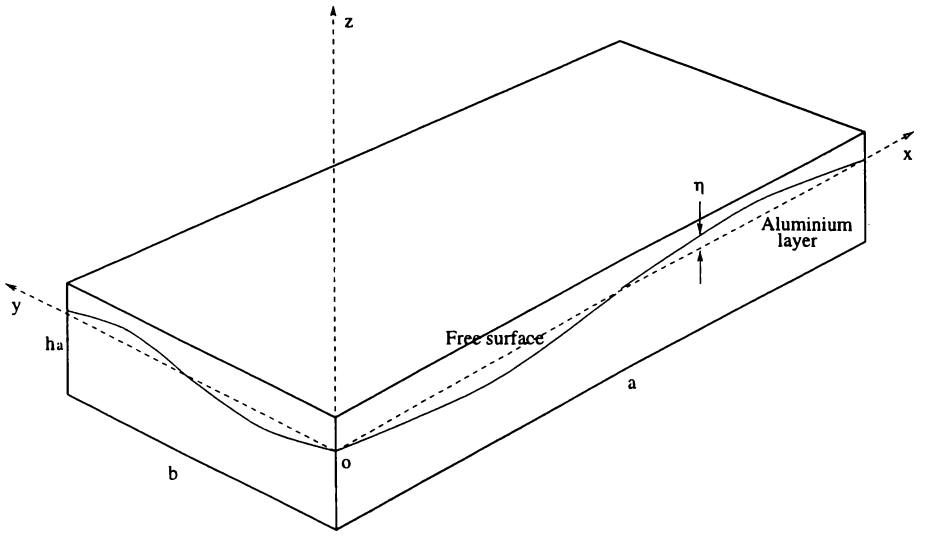


Figure 7.1: A rectangular container, where the free surface of liquid aluminium flow is affected by the electromagnetic force.

### 7.2.1 Velocity perturbation

We apply similar methods to obtain the wave evolution equations to those used in Chapter 5. The perturbation velocity field can be expressed by a velocity potential $\phi$ and a stream function $\psi$ mathematically as follows:

$$\mathbf{u} = \nabla\phi + \nabla\psi \times \hat{\mathbf{z}}. \tag{7.5}$$

The velocity potential $\phi$ is chosen to have the following form, which satisfies the boundary conditions,

$$\begin{aligned} \phi &= g_\alpha(z)E_\alpha(x,y)b_\alpha(t) \\ &\stackrel{def}{=} \phi_\alpha b_\alpha(t), \end{aligned} \tag{7.6}$$

where the $g_\alpha(z) = g^a_\alpha(z)$ (here we have only one liquid layer) and $E_\alpha$ are exactly the same functions as used in Chapter 5.

Then, the free surface displacement $\eta$ can be expanded in terms of the $E_\alpha$ and the time $t$,

$$\eta = \eta_\alpha(t)E_\alpha. \tag{7.7}$$

### 7.2.2 Equations of motion

The general form of the linearised equation of motion is simplified from the Navier-Stokes equations as follows:

$$\begin{aligned} &\rho\frac{\partial \mathbf{u}}{\partial t} + k\mathbf{u} + \rho\Omega\hat{\mathbf{z}} \times \mathbf{u} + \rho\omega\hat{\mathbf{z}} \times \mathbf{U} \\ &+\nabla p_T - \mathbf{f}_I = 0, \end{aligned} \tag{7.8}$$

where $\mathbf{f}_I$ denotes the induced magnetic damping force.

The governing equations for the $\phi$ are written as:

$$\nabla \cdot \mathbf{u} = \nabla^2 \phi = 0,\ \frac{\partial \phi}{\partial n} = 0 \text{ on solid boundaries, } \dot{\eta} = \frac{\partial \phi}{\partial z} \text{ on free surface.}$$

### 7.2.3 Scalar formulation

As before to obtain the scalar evolution equation for the variables $b_m$, we shall take the inner product of the equation of motion with $\nabla \phi_m$ as follows:

$$\begin{aligned} \rho &< \dot{\mathbf{u}}, \nabla \phi_m > + < k\mathbf{u}, \nabla \phi_m > + < \nabla p, \nabla \phi_m > \\ - &< \mathbf{f}_I, \nabla \phi_m >= 0. \end{aligned} \tag{7.9}$$

Now we have the evolution equations as follows:

$$A_m \dot{b}_m + C_m b_m + G_m \eta_m - f_m = 0, \tag{7.10}$$

where $f_m$ denotes the induced magnetic damping term.

The coefficient matrices in the above equation are listed as:

$$\begin{aligned} A_m &= \rho g_m(0) ||E_m||^2, \\ C_m &= k g_m(0) ||E_m||^2, \\ G_m &= \rho g ||E_m||^2. \end{aligned} \tag{7.11}$$

### 7.2.4 Free surface displacement

The usual kinematic free-surface condition implies:

$$u_{z=0} = \dot{\eta} = \frac{\partial \phi}{\partial z}. \tag{7.12}$$

Thus, we have

$$\begin{aligned} \dot{\eta} &= E_\alpha b_\alpha, \\ E_\alpha \dot{\eta}_\alpha &= E_\alpha b_\alpha, \end{aligned} \tag{7.13}$$

or we simply find

$$\dot{\eta}_m = b_m. \tag{7.14}$$

Now using $b_m = \dot{\eta}_m$, (7.10) can be written as:

$$A_m \ddot{\eta}_m + C_m \dot{\eta}_m + G_m \eta_m - f_m = 0. \tag{7.15}$$

### 7.2.5 Calculating the induced current

From Faraday's law, the induced current $\mathbf{J}_I$ is given by:

$$\begin{aligned} \mathbf{J}_I &= \sigma(\mathbf{u} \times \mathbf{B}) + \nabla\varphi \\ &= \nabla\chi \times \hat{\mathbf{z}}, \end{aligned} \tag{7.16}$$

where the current stream function $\chi$ can be expressed as

$$\chi = H_\alpha d_\alpha(t), \tag{7.17}$$

which automatically satisfies the lateral boundary conditions. In this shallow layer assumption, vertical velocity is considered to be much smaller than horizontal velocity ($u_x$, $u_y \gg u_z$). Then the induced current $\mathbf{J}_I$ will be independent of $z$ (each horizontal cross-section of container is identical).

Taking the $z$-component of the curl of (7.16) we eliminate the current potential term $\varphi$ as follows:

$$\begin{aligned} -\nabla^2\chi &= [\sigma\nabla \times (\mathbf{u} \times \mathbf{B})] \cdot \hat{\mathbf{z}} \\ &= \sigma(\mathbf{B} \cdot \nabla)\,\mathbf{u} \cdot \hat{\mathbf{z}} \\ &= \sigma B_z \frac{\partial u_z}{\partial z} \\ &= \sigma B_z g''_\alpha(z) E_\alpha b_\alpha, \end{aligned} \tag{7.18}$$

where assuming that $\mathbf{B} = B_z\hat{\mathbf{z}}$ is constant, the term $\nabla \times (\mathbf{u} \times \mathbf{B})$ can be simplified using the standard vector identity as

$$\begin{aligned} \nabla \times (\mathbf{u} \times \mathbf{B}) &= (\mathbf{B} \cdot \nabla)\,\mathbf{u} - (\mathbf{u} \cdot \nabla)\,\mathbf{B} + \mathbf{u}(\nabla \cdot \mathbf{B}) - \mathbf{B}(\nabla \cdot \mathbf{u}) \\ &= (\mathbf{B} \cdot \nabla)\,\mathbf{u}. \end{aligned} \tag{7.19}$$

We can use (7.17) and (7.18) to express the $d_m$ coefficients in terms of the $\dot{\eta}_m$. Since

$$\begin{aligned} -\nabla^2\chi &= \lambda_\alpha^2 H_\alpha d_\alpha \\ &= \sigma B_z g''_\alpha(z) E_\alpha b_\alpha. \end{aligned} \tag{7.20}$$

We take the inner product of each side with $H_m$ and obtain,

$$\lambda_m^2 |H_m|^2 d_m = \sigma B_Z Q^{(9)}_{m\alpha} \dot{\eta}_\alpha, \tag{7.21}$$

where the coefficient $Q^{(9)}_{m\alpha}$ is defined in Appendix II. Here we have used the orthogonality of the $H_m$. Also since $g'(0) = 1$ and $g'(-h) = 0$ it follows that

$$\int_{-h}^{0} g''(z)dz = 1. \tag{7.22}$$

To summarise, we can write,

$$d_m = S_{m\alpha}\dot{\eta}_\alpha, \tag{7.23}$$

where

$$S_{m\alpha} = \frac{\sigma B_z Q^{(9)}_{m\alpha}}{\lambda_m^2 h ||H_m||^2}.$$

The above equation shows that the evolution coefficient $d_m$ for the induced current can be expressed in terms of the wave evolution coefficient $\dot{\eta}_\alpha$ and the magnetic field $B_z$. This result will be used to calculate the induced damping force in the next section.

### 7.2.6 Calculating the induced damping force $\mathbf{J}_I \times \mathbf{B}$

When we include the induced magnetic damping term, the general form of the linearised equation of motion is written as:

$$\begin{aligned} &\rho\frac{\partial \mathbf{u}}{\partial t} + k\mathbf{u} + \rho\Omega\hat{\mathbf{z}} \times \mathbf{u} + \rho\omega\hat{\mathbf{z}} \times \mathbf{U} \\ &+\nabla p_T - \mathbf{f}_I = 0, \end{aligned} \tag{7.24}$$

From (7.16), $\mathbf{f}_I$ can be represented by the current stream function $\chi$ and the magnetic field $\mathbf{B}$ as follows:

$$\begin{aligned} \mathbf{f}_I &= \mathbf{J}_I \times \mathbf{B} \\ &= (\nabla\chi \times \hat{\mathbf{z}}) \times \mathbf{B} \\ &= [d_\alpha(t)\nabla H_\alpha \times \hat{\mathbf{z}}] \times \mathbf{B} \\ &= -B_z \nabla H_\alpha d_\alpha(t). \end{aligned} \tag{7.25}$$

Then, by the inner product of the equation of motion (7.24) with $\nabla E_m$, the evolution equations can be written with the additional coefficient $T_{m\alpha}$ as follows:

$$A_m\ \ddot{\eta}_m + C_m\dot{\eta}_m + G_m\eta_m + T_{m\alpha}d_\alpha = 0, \tag{7.26}$$

where the induced damping coefficient $T_{m\alpha}$ is

$$\begin{aligned} T_{m\alpha} &= -B_z \int g_m(z)dz \int_\Gamma \nabla H_\alpha \cdot \nabla E_m d\Gamma \\ &= -B_z\ \bar{g}_m\ Q^{(10)}_{m\alpha}. \end{aligned} \tag{7.27}$$

### 7.2.7 The energy dissipation rate by the induced force

We shall calculate the rate $R_I$ at which the induced magnetic damping force $\mathbf{f}_I$ does work. This rate is useful for investigating the effects of the magnetic field on the induced damping. When $\mathbf{B}$ is constant, we can write the energy dissipation rate

$$R_I = \int \mathbf{f}_I \cdot \mathbf{u} dV$$

$$
\begin{aligned}
&= \int (\mathbf{J}_I \times \mathbf{B}) \cdot \mathbf{u} dV \\
&= \int [(d_m(t) \nabla H_m \times \hat{\mathbf{z}}) \times \mathbf{B}] \cdot \mathbf{u} dV \\
&= \int (-B_z \nabla H_m) d_m(t) \cdot \{\nabla g_\alpha(z) E_\alpha b_\alpha(t) + \nabla H_\alpha c_\alpha(t) \times \hat{\mathbf{z}}\} dV \\
&= -\int B_z \nabla H_m d_m(t) \cdot \nabla g_\alpha(z) E_\alpha b_\alpha(t) dV \\
&\quad -\int B_z \nabla H_m d_m(t) \cdot (\nabla H_\alpha c_\alpha(t) \times \hat{\mathbf{z}}) dV, \qquad (7.28)
\end{aligned}
$$

where the last term of the above equation vanishes as follows:

$$
\begin{aligned}
\int B_z \nabla H_m d_m(t) \cdot (\nabla H_\alpha c_\alpha(t) \times \hat{\mathbf{z}}) dV &= B_z d_m(t) c_\alpha(t) \int \nabla H_m \cdot (\nabla H_\alpha \times \hat{\mathbf{z}}) dV \\
&= B_z d_m(t) c_\alpha(t) h \int \nabla H_m \cdot (\nabla H_\alpha \times \hat{\mathbf{z}}) d\Gamma \\
&= B_z d_m(t) c_\alpha(t) h \int [H_m, H_\alpha] d\Gamma \\
&= 0. \qquad (7.29)
\end{aligned}
$$

Thus, we have

$$
\begin{aligned}
R_I &= -B_z \int \partial_\alpha H_m \partial_\alpha E_\alpha d\Gamma \int g_\alpha(z) dz d_m(t) b_\alpha(t) \\
&= U_{m\alpha} d_m(t) b_\alpha(t) \\
&= U_{m\alpha} S_{mk} b_k(t) b_\alpha(t), \qquad (7.30)
\end{aligned}
$$

where

$$
U_{m\alpha} = -B_z Q_{m\alpha}^{(10)} \bar{g}_\alpha,
$$

and

$$
\begin{aligned}
S_{m\alpha} &= \frac{\sigma B_z Q_{m\alpha}^{(9)}}{\lambda_m^2 h_a ||H_m||^2}, \\
d_m(t) &= S_{m\alpha} b_\alpha(t). \qquad (7.31)
\end{aligned}
$$

from the previous section.

The rate $R_I$ shows that the magnetic damping force is irrotational, and therefore has no affect on the rotational part of the fluid motion. If we integrate the rate $R_I$ in time, we can obtain the total energy dissipated by the induced damping, which must equal the decrease in $\Delta KE + \Delta PE$ over the same time interval.

### 7.2.8 Numerical results

In order to verify the formulation, we calculate the total perturbation energy $\Delta E$ and the dissipated energy $\Delta DE$ by the induced damping as follows:

$$
\Delta E = \Delta PE + \Delta KE, \qquad (7.32)
$$

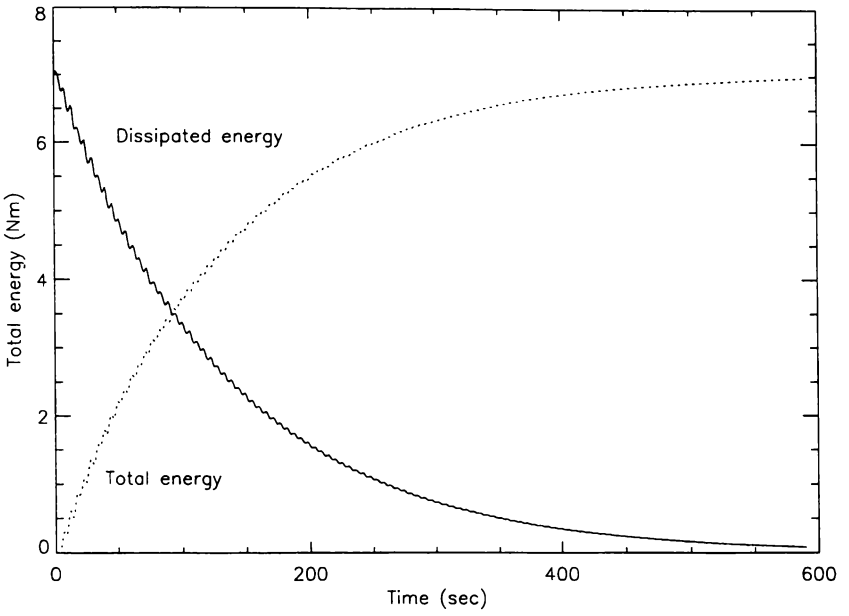


Figure 7.2: The energy dissipation by the induced magnetic damping in a rectangular container, where a=7.7m, b=3.3m, $h_a$=0.2m, $\alpha$=0, $B_z$=0.005 Tesla and the initial interface displacement $\eta_1$=0.01m.

$$\begin{aligned} \Delta DE &= \int R_I dt \\ &= \int U_{m\alpha} S_{mk} b_k b_\alpha dt, \end{aligned} \tag{7.33}$$

where the potential energy $\Delta PE$ and the kinetic energy $\Delta KE$ are written as:

$$\begin{aligned} \Delta PE &= \frac{1}{2}\rho g \int_\Gamma |\eta|^2 d\Gamma \\ &= \frac{1}{2}\rho g \int_\Gamma E_m^2 d\Gamma \eta_m^2 \\ &= \frac{1}{2}\rho g ||E_m||^2 \eta_m^2, \end{aligned} \tag{7.34}$$

$$\begin{aligned} \Delta KE &= \frac{1}{2}\rho \int_V \mathbf{u}\cdot\mathbf{u} dV \\ &= \frac{1}{2}\rho \int_V \nabla\phi\cdot\nabla\phi dV \\ &= \frac{1}{2}\rho \int_V \left[\{\partial_z g_m(z)\}^2 + g_m^2(z)\lambda_m^2\right] E_m^2 b_m^2 dV \\ &= \frac{1}{2}\rho \int_z \left[\{\partial_z g_m(z)\}^2 + g_m^2(z)\lambda_m^2\right] dz ||E_m||^2 b_m^2. \end{aligned} \tag{7.35}$$

In calculating $\Delta KE$, the rotational flow motion is not included, as we give the irrotational perturbation. Figure 7.2 shows all the energy is eventually dissipated by magnetic damping.

Also Figure 7.3 shows the kinetic energy dissipation time by the induced magnetic damping due to the vertical magnetic field $B_z$ in a rectangular container. The stronger magnetic field shows the shorter dissipation time, as we expected.

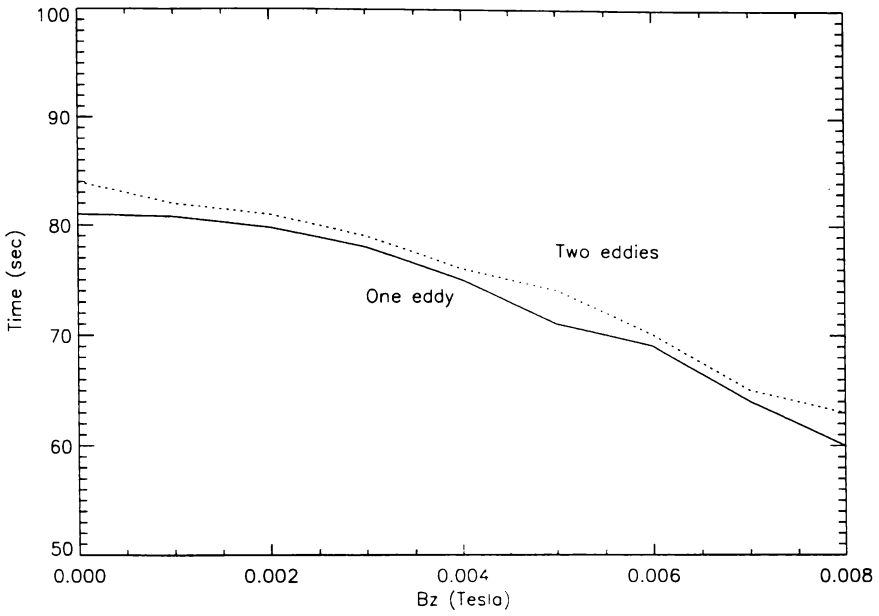


Figure 7.3: The energy dissipation time by the induced magnetic damping in a rectangular container, where a=7.7m, b=3.3m. $h_a$=0.2m, $\alpha$=1, $B_z$=0.005 Tesla and the initial interface displacement $\eta_1$=0.01m. The dissipation time is defined to be the time taken for the energy to decay to 1% of its initial value.

In this section, we investigated the induced magnetic damping in an insulating container. The assumption of insulating walls corresponds to the situation in an alumunium reduction cell, but here for simplicity we have considered only a single layer. This simplification shows us the energy dissipation mechanism by the induced magnetic damping force very well.

## 7.3 Induced magnetic damping in a perfectly conducting container

In this section, we consider the induced magnetic damping in containers with perfectly-conducting walls. In this case, the lateral boundary conditions $\mathbf{J}_I \cdot \hat{\mathbf{n}} = 0$ are no longer valid. On the perfectly-conducting boundaries, the electric field $\mathbf{E}$ is continuous. So $\mathbf{E} = 0$ in fluid adjacent to the boundaries. Thus the induced current potential $\varphi = 0$ on the boundaries.

From Maxwell's equations as in Section 7.2, we write the induced current in the form:

$$\mathbf{J}_I = \sigma \mathbf{u} \times \mathbf{B} + \nabla\varphi. \tag{7.36}$$

By the conservation of the induced current

$$\nabla \cdot \mathbf{J}_I = \nabla \cdot \sigma(\mathbf{u} \times \mathbf{B}) + \nabla^2\varphi$$

$$= 0, \tag{7.37}$$

we have

$$\begin{aligned}
\nabla^2\varphi &= -\sigma\nabla\cdot(\mathbf{u}\times\mathbf{B}) \\
&= -\sigma B_z(\nabla\times\mathbf{u})\cdot\hat{\mathbf{z}} \\
&= -\sigma B_z\omega_z \\
&= -\sigma B_z\lambda_\alpha^2 H_\alpha c_n \\
&= \sigma B_z\nabla^2\psi.
\end{aligned} \tag{7.38}$$

Thus $\varphi = \sigma B_z\psi$ is the solution since this also satisfies the required boundary condition.

Therefore, the induced force $\mathbf{f}_I$ is

$$\begin{aligned}
\mathbf{f}_I &= \mathbf{J}_I\times\mathbf{B} \\
&= [\sigma(\mathbf{u}\times\mathbf{B})+\nabla\varphi]\times\mathbf{B} \\
&= \sigma(\mathbf{B}\cdot\mathbf{u})\mathbf{B} - \sigma(\mathbf{B}\cdot\mathbf{B})\mathbf{u} + \sigma\nabla\varphi\times\mathbf{B}, \\
&= \sigma B_z^2[u_z\hat{\mathbf{z}} - (\nabla\phi + \nabla\psi\times\hat{\mathbf{z}}) + \nabla\psi\times\hat{\mathbf{z}}] \\
&= \sigma B_z^2(u_z\hat{\mathbf{z}} - \nabla\phi) \\
&= -\sigma B_z^2(\nabla\phi_x, \nabla\phi_y, 0),
\end{aligned} \tag{7.39}$$

where $\nabla\phi_z = u_z\hat{\mathbf{z}}$.

### 7.3.1 Equations of motion

When we include the induced damping term, the general form of the linearized equation of motion is written as:

$$\begin{aligned}
&\rho\frac{\partial\mathbf{u}}{\partial t} + k\mathbf{u} + \rho\Omega\hat{\mathbf{z}}\times\mathbf{u} + \rho\omega\hat{\mathbf{z}}\times\mathbf{U} \\
&+\nabla p_T - \mathbf{f}_I = 0,
\end{aligned} \tag{7.40}$$

where the $\mathbf{f}_I$ is the induced magnetic damping force in a electrically conducting container.

The inner product $< \mathbf{f}_I, \nabla\phi_m >$ is written in terms of the wave evolution variable $b_\alpha(t)$ as follows:

$$\begin{aligned}
< \mathbf{f}_I, \nabla\phi_m > &= < \mathbf{J}_I\times\mathbf{B}, \nabla\phi_m > \\
&= < -\sigma B_z^2(\nabla\phi_x, \nabla\phi_y), \nabla\phi_m >,
\end{aligned} \tag{7.41}$$

when

$$\mathbf{B} = B_z\hat{\mathbf{z}}. \tag{7.42}$$

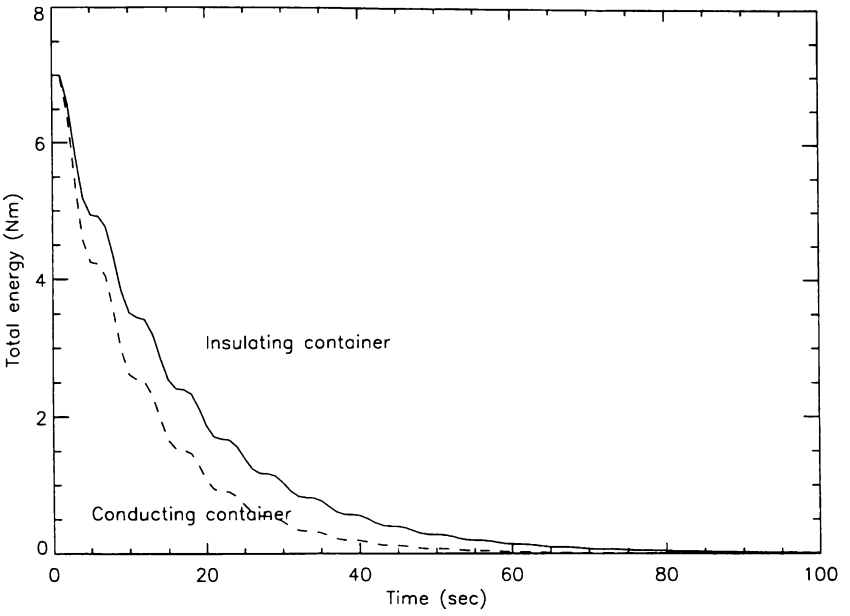


Figure 7.4: The energy dissipation by the induced magnetic damping in a perfectly-conducting container, where $B_z$=0.005 Tesla, a=7.7m, b=3.3m, $h_a$=0.2m, $\alpha$=1 and the initial interface displacement $\eta_1$=0.01m.

Finally, we have

$$\begin{aligned} < \mathbf{f}_I, \nabla\phi_m > &= -\sigma B_z^2 \int g_\alpha(z) g_m(z) dz \int_\Gamma \nabla E_\alpha \cdot \nabla E_m d\Gamma b_\alpha \\ &= T_m^1 b_m, \end{aligned} \tag{7.43}$$

where

$$T_m^1 = -\sigma B_z^2 \lambda_m^2 \, \bar{g}_{mm} \, ||E_m||^2. \tag{7.44}$$

Thus, the first evolution equations can be written with the additional coefficient $T_m^1$ as follows:

$$A_m \dot{b}_m + (C_m + T_m^1) b_m + E_{m\alpha} c_\alpha + G_{m\alpha} \eta_\alpha = 0 \tag{7.45}$$

The perturbation of vorticity can be obtained by taking the $z$-component of the curl of the equation of motion as follows:

$$\frac{\partial \omega}{\partial t} + \frac{k}{\rho}\omega + \mathbf{u} \cdot \nabla\Omega + \mathbf{U} \cdot \nabla\omega + \frac{1}{\rho}(\nabla \times \mathbf{f}_I) \cdot \hat{\mathbf{z}} = 0, \tag{7.46}$$

where the induced damping term vanishes since

$$\begin{aligned} \frac{1}{\rho}(\nabla \times \mathbf{f}_I) \cdot \hat{\mathbf{z}} &= \frac{1}{\rho}\left[\nabla \times \{-\sigma B_z^2 (\nabla\phi)_h\}\right] \cdot \hat{\mathbf{z}} \\ &= 0. \end{aligned} \tag{7.47}$$

Thus, the above equation shows us that the vorticity equation is not affected by the induced damping force.

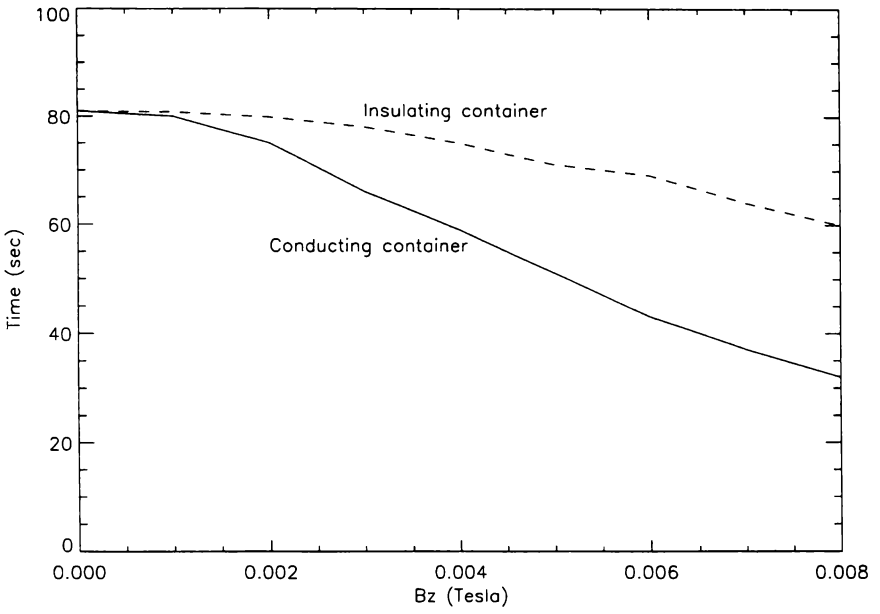


Figure 7.5: The energy dissipation time by the induced magnetic damping in a perfectly-conducting container, where a=7.7m, b=3.3m, $h_a$=0.2m, $\alpha$=1 and the initial interface displacement $\eta_1$=0.01m.

### 7.3.2 Wave evolution equations

Now we have the wave evolution equations with the induced damping term for the three sets of unknown variables $b_\alpha, c_\alpha$ and $\eta_\alpha$ in a electrically conducting container as follows:

$$A_m \ddot{\eta}_m + (C_m + T_m^1)\dot{\eta}_m + E_{m\alpha} c_\alpha + G_{m\alpha}\eta_\alpha = 0, \tag{7.48}$$

$$\dot{\eta}_m - b_m = 0, \tag{7.49}$$

$$J_m \dot{c}_m + K_{m\alpha} b_\alpha + L_{m\alpha} c_\alpha + M_{m\alpha}\eta_\alpha = 0. \tag{7.50}$$

The second equation is derived in Section (7.2) and the last equation is the vorticity equation as used in Section (5.2.8).

### 7.3.3 Numerical results

Figures 7.4 and 7.5 compare the rate of energy dissipation in insulating and conducting containers. Clearly the damping is much stronger in conducting containers. In an insulating container an induced electric field is established to ensure that no current can flow through the wall. This field partially cancels the $\sigma \mathbf{u} \times \mathbf{B}$ field, and so reduces the induced current.

In this section, we investigated the induced magnetic damping in a perfectly-conducting container which has a different electromagnetic boundary condition. Finally, we will explore the induced magnetic damping perturbation in aluminium reduction cells in the next section, which is our main interest.

## 7.4 Induced magnetic damping in aluminium reduction cells

Magnetic damping occurs almost exclusively in the aluminium layer, as the cryolite is much poorer electrical conductor. Because carbon walls are relatively insulating, we can take the induced current $\mathbf{J}_I$ in terms of a current stream function $\chi$ (see Section 7.2.5) as follows:

$$\mathbf{J}_I = \nabla\chi(x,y) \times \hat{\mathbf{z}}, \tag{7.51}$$

so that $\mathbf{J}_I$ satisfies the current continuity equation,

$$\nabla \cdot \mathbf{J}_I = 0. \tag{7.52}$$

The current stream function $\chi$ can be expanded in terms of the eigenfunction $H_\alpha$,

$$\chi(x,y) = H_\alpha(x,y)d_\alpha(t). \tag{7.53}$$

This formulation is based on the same assumptions as discussed in the previous sections.

From Maxwell's equations, we can write

$$\begin{aligned} \sigma\left(\mathbf{u} \times \mathbf{B} + \nabla\varphi\right) &= \mathbf{J}_I \\ &= \nabla\chi \times \hat{\mathbf{z}}, \end{aligned} \tag{7.54}$$

where the $\varphi$ denotes the electric potential.

To determine $\chi$ we consider the $z$-component of the curl of the above equation, eliminating $\varphi$:

$$\begin{aligned} -\nabla^2\chi &= [\sigma\nabla \times (\mathbf{u} \times \mathbf{B})] \cdot \hat{\mathbf{z}} \\ &= \sigma[(\mathbf{B} \cdot \nabla)\,\mathbf{u} - (\mathbf{u} \cdot \nabla)\,\mathbf{B}] \cdot \hat{\mathbf{z}} \\ &= \sigma B_z \partial_z \mathbf{u} \cdot \hat{\mathbf{z}} - \sigma(\mathbf{u} \cdot \nabla)B_z \\ &= \sigma B_z \partial_z(\nabla\phi + \nabla\psi \times \hat{\mathbf{z}}) \cdot \hat{\mathbf{z}} \\ &\quad -\sigma\{(\nabla\phi + \nabla\psi \times \hat{\mathbf{z}}) \cdot \nabla\}B_z \\ &= \sigma B_z \partial_z\{\partial_z g_\alpha(z) E_\alpha b_\alpha\} \\ &\quad -\{\sigma g_\alpha(z)(\nabla E_\alpha \cdot \nabla B_z)b_\alpha + \sigma[B_z, H_\alpha]c_\alpha\} \\ &= \sigma\{B_z\partial_z^2 g_\alpha(z)E_\alpha - g_\alpha(z)\nabla E_\alpha \cdot \nabla B_z\}b_\alpha \\ &\quad -\sigma[B_z, H_\alpha]c_\alpha. \end{aligned} \tag{7.55}$$

Here we have used the vector identity:

$$\begin{aligned} \nabla \times (\mathbf{u} \times \mathbf{B}) &= (\mathbf{B} \cdot \nabla)\,\mathbf{u} - (\mathbf{u} \cdot \nabla)\,\mathbf{B} + \mathbf{u}\,(\nabla \cdot \mathbf{B}) - \mathbf{B}\,(\nabla \cdot \mathbf{u}) \\ &= (\mathbf{B} \cdot \nabla)\,\mathbf{u} - (\mathbf{u} \cdot \nabla)\,\mathbf{B}, \end{aligned} \tag{7.56}$$

assuming incompressible flow, and $\mathbf{B} = B_z\hat{\mathbf{z}}$.

By rearranging (7.55), we have

$$\begin{aligned} -\nabla^2\chi &= \sigma\{B_z\partial_z^2 g_\alpha(z)E_\alpha \\ &\quad -g_\alpha(z)\nabla E_\alpha\cdot\nabla B_z\}b_\alpha - \sigma[B_z,H_\alpha]c_\alpha \\ \lambda_\alpha^2 H_\alpha d_\alpha &= \sigma\{B_z\partial_z^2 g_\alpha(z)E_\alpha - g_\alpha(z)\nabla E_\alpha\cdot\nabla B_z\}b_\alpha \\ &\quad -\sigma[B_z,H_\alpha]c_\alpha, \end{aligned} \tag{7.57}$$

where $b_\alpha$ and $c_\alpha$ denote the same variables as used in Chapter 5.

By taking the inner product of the above equation with $H_m$ over the liquid volume, we have

$$\begin{aligned} \lambda_\alpha^2\int_V H_\alpha H_m dV d_\alpha &= \sigma\int_V\{B_z\partial_z^2 g_\alpha(z)E_\alpha - g_\alpha(z)\nabla E_\alpha\cdot\nabla B_z\}H_m dV b_\alpha \\ &\quad -\sigma\int_V[B_z,H_\alpha]H_m dV c_\alpha, \end{aligned} \tag{7.58}$$

or

$$\begin{aligned} \lambda_\alpha^2 h_a\int_\Gamma H_\alpha H_m d\Gamma d_\alpha &= \sigma\int\partial_z^2 g_\alpha(z)dz\int_\Gamma B_z E_\alpha H_m d\Gamma b_\alpha \\ &\quad -\sigma\int g_\alpha(z)dz\int_\Gamma H_m\nabla B_z\cdot\nabla E_\alpha d\Gamma b_\alpha \\ &\quad -\sigma h_a\int_\Gamma[B_z,H_\alpha]H_m d\Gamma c_\alpha \\ &= (\sigma Q_{m\alpha}^{(11)} - \sigma\,\bar{g}_\alpha\,Q_{m\alpha}^{(12)})b_\alpha \\ &\quad -\sigma h_a Q_{m\alpha}^{(13)}c_\alpha, \end{aligned} \tag{7.59}$$

where the integration coefficients are written in Appendix II.

Finally, by orthogonality of the eigenfunctions $H_\alpha$, we have one more set of evolution equation for the electromagnetic damping as follows:

$$R_m d_m = S_{m\alpha}^{(1)}b_\alpha + S_{m\alpha}^{(2)}c_\alpha, \tag{7.60}$$

where

$$\begin{aligned} R_m &= \lambda_m^2 h_a||H_m||^2, \\ S_{m\alpha}^{(1)} &= \sigma Q_{m\alpha}^{(11)} - \sigma\,\bar{g}_\alpha\,Q_{m\alpha}^{(12)}, \\ S_{m\alpha}^{(2)} &= -\sigma h_a Q_{m\alpha}^{(13)}. \end{aligned} \tag{7.61}$$

### 7.4.1 Equations of motion

When we include the electromagnetic damping term, the general form of the linearised equation of motion is written as:

$$\begin{aligned} &\rho\frac{\partial\mathbf{u}}{\partial t} + k\mathbf{u} + \rho\Omega\hat{\mathbf{z}}\times\mathbf{u} + \rho\omega\hat{\mathbf{z}}\times\mathbf{U} \\ &+\nabla p_T - \mathbf{f}_I = 0, \end{aligned} \tag{7.62}$$

where the $\mathbf{f}_I$ is the electromagnetic damping force by the induced current in a reduction cell.

The inner product $< \mathbf{f}_I, \nabla\phi_m >$ is written in terms of the coefficients $d_\alpha$ as follows:

$$\begin{aligned} & < \mathbf{f}_I, \nabla\phi_m > \\ = & < (-B_z \nabla H_\alpha) d_\alpha(t), \nabla\phi_m > \\ = & \int_V (-B_z \nabla H_\alpha) \cdot \nabla\phi_m dV d_\alpha \\ = & \int_V (-B_z \nabla H_\alpha) \cdot \nabla \left(g_m(z) E_m\right) dV d_\alpha \\ = & - \bar{g}_m \, Q^{(14)}_{m\alpha} d_\alpha \\ = & \; T_{m\alpha} d_\alpha, \end{aligned} \tag{7.63}$$

where

$$\begin{aligned} Q^{(14)}_{m\alpha} &= \int_\Gamma B_z \nabla H_\alpha \cdot \nabla E_m d\Gamma, \\ T_{m\alpha} &= - \bar{g}_m \, Q^{(14)}_{m\alpha}. \end{aligned} \tag{7.64}$$

The induced damping force is given by

$$\begin{aligned} \mathbf{f}_I &= \mathbf{J}_I \times \mathbf{B} \\ &= (\nabla\chi \times \hat{\mathbf{z}}) \times \mathbf{B} \\ &= [d_\alpha(t) \nabla H_\alpha \times \hat{\mathbf{z}}] \times \mathbf{B} \\ &= (-B_z \nabla H_\alpha) d_\alpha(t). \end{aligned} \tag{7.65}$$

The first of six evolution equations can be written with the additional coefficient $T_{m\alpha}$ representing the induced magnetic damping as follows:

$$\begin{aligned} & A_m \dot{b}_m + B_m \dot{b}^c_m + C_{m\alpha} b_\alpha + D_{m\alpha} b^c_\alpha \\ & + E_{m\alpha} c_\alpha + F_{m\alpha} c^c_\alpha + G_{m\alpha} \eta_\alpha + T_{m\alpha} d_\alpha + Q_m = 0. \end{aligned} \tag{7.66}$$

The perturbation of vorticity can be obtained by taking the $z$-component of the curl of (7.62) as follows:

$$\frac{\partial\omega}{\partial t} + \frac{k}{\rho}\omega + \mathbf{u} \cdot \nabla\Omega + \mathbf{U} \cdot \nabla\omega + \frac{1}{\rho}[\nabla \times (-\mathbf{f}_I)] \cdot \hat{\mathbf{z}} = 0, \tag{7.67}$$

where the electromagnetic damping term will vanish as:

$$[\nabla \times \mathbf{f}_I] \cdot \hat{\mathbf{z}} = [\nabla \times (-B_z \nabla H_\alpha) \, d_\alpha(t)] \cdot \hat{\mathbf{z}} \tag{7.68}$$

$$= 0. \tag{7.69}$$

As before we find that the induced magnetic damping term does not affect vorticity.

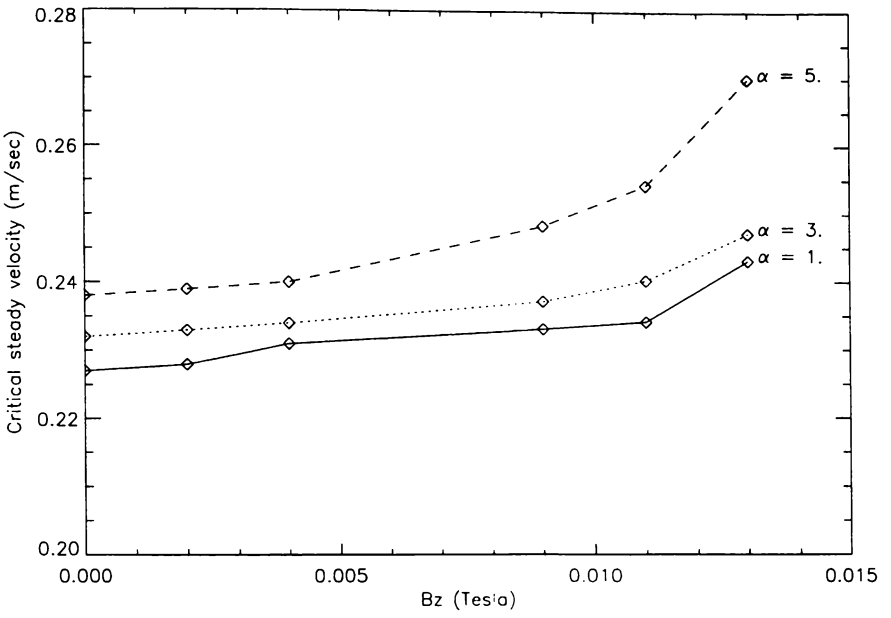


Figure 7.6: The critical steady velocity when the induced magnetic damping force is included, where a=7.7m, b=3.3m, $h_a$=0.2m and ACD=0.04m.

### 7.4.2 Wave evolution equations

When we include magnetic damping the evolution equations for the six coefficients $b^a_\alpha, b^c_\alpha, c^a_\alpha, c^c_\alpha, d^a_\alpha$ and $\eta_\alpha$ take the form:

$$A_m\dot{b}^a_m + B_m\dot{b}^c_m + C_{m\alpha}b^a_\alpha + D_{m\alpha}b^c_\alpha + E_{m\alpha}c^a_\alpha + F_{m\alpha}c^c_\alpha + G_{m\alpha}\eta_\alpha + T_{m\alpha}d^a_\alpha + Q_m = 0, \tag{7.70}$$

$$b^c_m = b^a_m - H_{m\alpha}\eta_\alpha. \tag{7.71}$$

$$\dot{\eta}_m + I_{m\alpha}\eta_\alpha - b^a_m = 0. \tag{7.72}$$

$$J_m\dot{c}^a_m + K_{m\alpha}b^a_\alpha + L_{m\alpha}c^a_\alpha + M_{m\alpha}\eta_\alpha = 0, \tag{7.73}$$

$$J_m\dot{c}^c_m + N_{m\alpha}b^c_\alpha + O_{m\alpha}c^c_\alpha + P_{m\alpha}\eta_\alpha = 0, \tag{7.74}$$

$$R_m d^a_m = S^{(1)}_{m\alpha}b^a_\alpha + S^{(2)}_{m\alpha}c^a_\alpha. \tag{7.75}$$

By eliminating the $\dot{b}^c_\alpha$, the $b^c_\alpha$ and the $d_\alpha$ in the above equations, we can reduce the number of the equations:

$$(A_m + B_m)\dot{b}^a_m - B_m H_{m\alpha}\dot{\eta}_\alpha + (C_{m\alpha} + D_{m\alpha} + T_{mk}S^{(1)}_{k\alpha}/R_k)b^a_\alpha + (E_{m\alpha} + T_{mk}S^{(2)}_{k\alpha}/R_k)c^a_\alpha + F_{m\alpha}c^c_\alpha + (G_{m\alpha} - D_{mk}H_{k\alpha})\eta_\alpha + Q_m = 0, \tag{7.76}$$

$$J_m\dot{c}^a_m + K_{m\alpha}b^a_\alpha + L_{m\alpha}c^a_\alpha + M_{m\alpha}\eta_\alpha = 0, \tag{7.77}$$

$$J_m\dot{c}^c_m + N_{m\alpha}b^a_\alpha + O_{m\alpha}c^c_\alpha + (P_{m\alpha} - N_{mk}H_{k\alpha})\eta_\alpha = 0, \tag{7.78}$$

$$\dot{\eta}_m + I_{m\alpha}\eta_\alpha - b^a_m = 0. \tag{7.79}$$

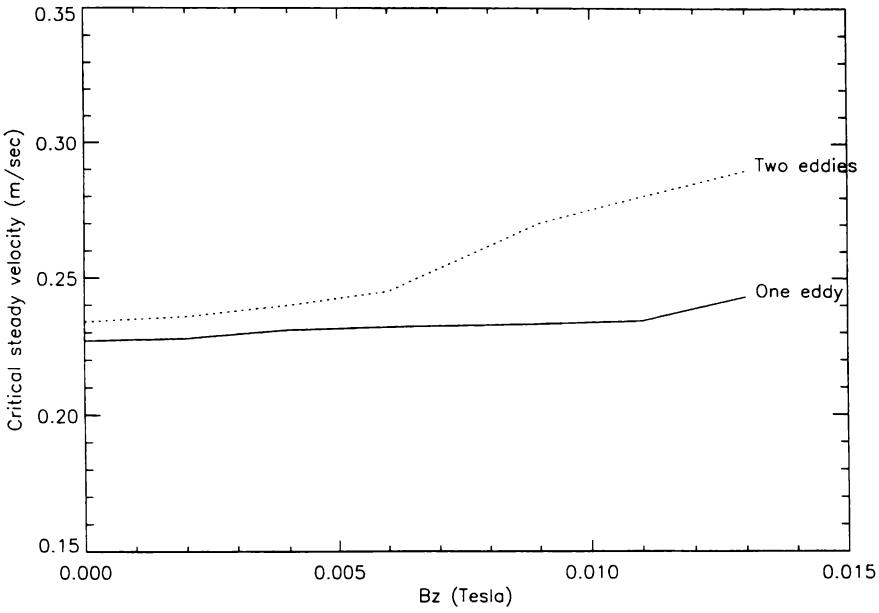


Figure 7.7: The critical steady velocity when the induced magnetic damping force is included, where a=7.7m, b=3.3m, $h_a$=0.2m, ACD=0.04m, $\alpha$=1 and basic flow configuration (1,1) & (2,1).

### 7.4.3 Numerical results

Results for the critical velocity when magnetic damping is included are shown in Figure 7.6. Generally, we find that the induced current is able to increase the critical steady velocity by less than 0.01m/sec approximately. This result shows that the positive effect of the vertical magnetic field due to the induced magnetic damping is only slight. Also Figure 7.7 shows that the induced damping is affected by the basic flow patterns.

In order to compare the electromagnetic boundary conditions, we calculate the critical steady velocity in a perfectly-conducting cell, where there is no insulation between the liquid aluminium and the cell wall. Figure 7.8 shows the effect of the induced magnetic damping force in a conducting cell, which is much stronger than in an insulating cell.

In addition, we reproduce Wang's modified magnetic damping estimation [83] according to the following formulation:

$$k = \frac{\alpha}{h_a} + \beta B_o^2,$$

as reviewed in Chapter 2. This result shows that his formulation is useful only when we estimate the coefficient $\beta$ properly as shown in Figure 7.8. In his approximation, the $\beta$ has the value in the range of $10^{-2}\sigma - 10^{0}\sigma$ which is too wide to be useful. However, if a reasonable estimation is provided from empirical data, his approximation is very convenient for calculation (i.e. $\beta = 0.5\sigma$ works reasonably well).

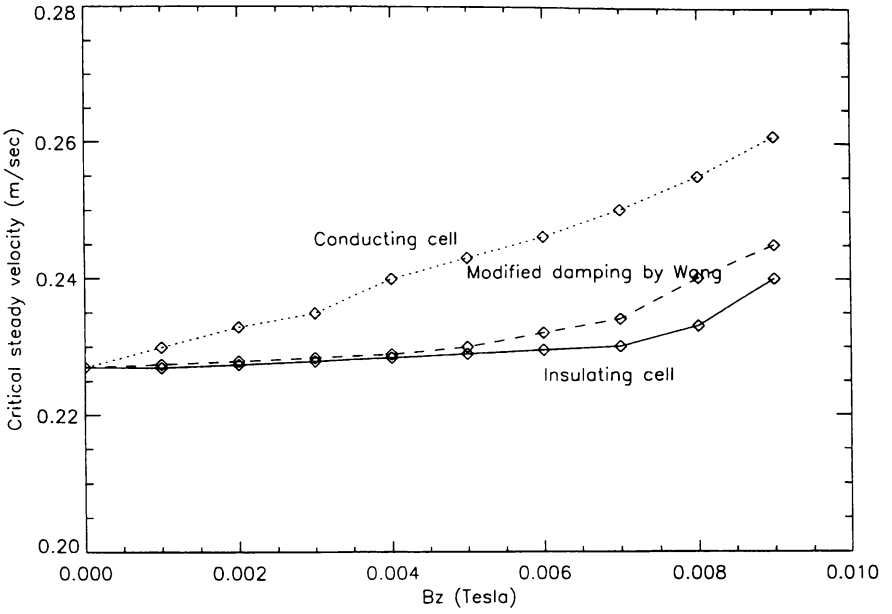


Figure 7.8: The critical steady velocity due to the modified magnetic damping by Wang when $\beta = 0.5\sigma = 2.5 \times 10^6$ is assumed, where a=7.7m, b=3.3m, $h_a$=0.2m, $\alpha$=1 and ACD=0.04m.

## 7.5 Conclusion

In the analysis of the induced magnetic damping perturbation for a single layer container, it is shown that the vertical magnetic field $B_z$ damps the liquid surface movement. The horizontal magnetic field is neglected for simplicity in our analysis.

Also the effect of the induced magnetic damping in a perfectly-conducting container is investigated with a different electromagnetic boundary condition, which shows stronger damping than in an insulating container.

In aluminium reduction cells with two liquid layers, though the induced magnetic damping force is weak, but does slightly improve the cell stability.

In conclusion, the electromagnetic field can affect the cell instability in two different ways. One is the induced magnetic damping effect due to the induced current which is positive for the interfacial instability and another is the driving effect on the steady flow due to the imposed magnetic field which is negative. Our simulation result shows that the negative effect is much greater than the positive. Thus it is very clear that the magnetic field **B**, which is the most dominant factor for the driving source on the basic steady flows, must be minimised for the control of the interfacial instability.

# Chapter 8

# Conclusions

We have investigated the K-H instability, which is a purely hydrodynamic interfacial instability in aluminium reduction cells. Also electromagnetic damping is studied with an improved treatment. The steady velocity difference between two liquid layers has been highlightened to explain the complex nature of the instability. The cryolite and aluminium velocity fields are represented in terms of potentials and stream functions, the Navier-Stokes equations are formulated as a system of ordinary differential equations for the time-dependent coefficients. The system in then integrated forward in time by standard methods. Various cell design and operation parameters such as steady velocity, ACD, frictional drag coefficient, cell dimension, liquid metal depth and velocity difference are considered in the numerical simulations. This study shows the K-H instability is one of the most dominant mechanisms in the interfacial instability.

In this chapter, we shall summarise the major research activities, the conclusions, the limitations and the suggestions on further work.

## 8.1 Research activities

The major research activities performed in this study are summarised as follows:

- A normal mode method is used to derive a system of ordinary differential equations describing the evolution of time-dependent 2D flow in rectangular regions. These can be linearised to determine the stability of steady flows.
- The conditions for steady 2D flow in rectangular regions are examined. In particular we show that a single Fourier-component flow is steady and stable.
- To ensure that the initial state is an equilibrium we start the flow evolution from a state of rest, gradually increasing the layer flows to their steady values.

This avoids an the initial pressure discontinuity across the interface which is present in previous work.

- The total perturbation energy is calculated to verify energy conservation and detect the instability. A bisection method is applied to find the critical steady velocity more efficiently.

- The program is used to predict the critical steady velocity practically with various cell design and operation parameters such as ACD, liquid metal depth, cell length, drag coefficient, steady velocity of basic flow and flow patterns. This may prove a useful tool in cell design.

- The K-H instability mechanism and Ziegler's work are compared in the analysis of the hydrodynamic interfacial instability. It is shown that the K-H instability mechanism is strongly destabilising as there exists a considerable velocity difference between the liquid layers in real cells always.

- Preliminary calculations with a single layer of conducting fluid in a rectangular container showed that electromagnetic damping depends crucially on the electrical conductivity of the container walls. It is much weaker in an insulating container than a perfectly-conducting one, because insulating walls inhibit the flow of induced current. This effect means that magnetic damping is much less effective in aluminium reduction cells than an order-of-magnitude analysis might suggest.

## 8.2 Conclusions

The main conclusions are summarised as follows:

- In a rectangular container a two-dimensional flow which includes only one Fourier component, is stable and steady. So it seems likely that the instability which occurs in aluminium reduction cells is not due to an inherent instability but to the interfacial mechanism between two liquid layers.

- The steady velocity in the aluminium layer is the most significant factor in the K-H instability. The interfacial instability can be improved by reducing the strong magnetic field, which drives the basic steady flow.

- Any interfacial instability approach will not be enough to configure the cell stability without considering the K-H instability mechanism, as the velocity difference always exists between two liquid layers in real cells.

- The purely hydrodynamic approach in the view of the K-H instability mechanism is very practical and useful for the evaluation of the interfacial instability in aluminium reduction cells without damaging the original physics seriously, unless the current flow instability is so dominant.

- The effect of the electromagnetic damping due to the induced current can reduce the interfacial instability slightly. However, the negative effect of the magnetic field by driving the basic flow is much stronger than the positive by the induced magnetic damping for the interfacial instability.

- Using the normal mode method for the form of the steady-state current, magnetic field or flow, the scheme is suitable for industrial application where these would be calculated numerically.

## 8.3 Limitations and further work

Although we are able to achieve some useful results in this research, there are inevitably some physical and mathematical limitations on account of the assumptions and the simplifications we made for our model. The limitations of this study and the suggestions on further work can be summarised as follows:

- The estimation of the frictional drag coefficient $\alpha$: An approximate value of the drag coefficient $\alpha = 1.0\text{kg/m}^2\text{s}$ was used in our simulation, which is calculated with values of $V_x = 0.15\text{m/s}$ and $L = 3\text{m}$ respectively from the formula by Bird [11]. The drag coefficient $\alpha$ can be adjusted properly according to the steady velocity and the cell width. The adjustment will give more realistic results for the simulation as the drag coefficient affects the interfacial instability.

- The estimation of the steady velocity difference ratio $r_d$ for the basic flow from the given electromagnetic field: For theoretical analysis, we assumed the steady cryolite velocity as half of the steady aluminium velocity in reduction cells, as Wang [83] did. However, it is not easy to measure or estimate the exact value of the velocity difference ratio. For more realistic simulation of the cell instability, the steady velocity difference must be estimated properly from the empirical data, as the instability mechanism depends upon it in a complex way. We are able to predict the critical steady velocity at which the system becomes unstable with our simulation program from the given steady velocities. If we can properly estimate and control the steady velocity difference ratio from the given electromagnetic field, it will be more efficient for the instability analysis. Antille, Flueck and Romerio [5] tried to obtain the steady velocity field from simultaneous measurements of anodic current fluctuations, which are analysed by an FFT method giving frequencies and amplitudes of the different modes. This method does not involve solving the Navier-Stokes equations. There are also some useful commercial program packages such as FLUENT [83]. A data acquisition method should be developed with a proper simulation package.

# Appendix I

# Proof that $M_{m\alpha\beta}$ is antisymmetric in each pair of suffixes

In Section 4.3, we defined

$$M_{m\alpha\beta} = \int_S [H_\alpha, H_\beta] H_m dS.$$

This is clearly antisymmetric in $\alpha$ and $\beta$.

Now

$$\nabla \times (H_m H_\alpha \nabla H_\beta) = \nabla(H_m H_\alpha) \times \nabla H_\beta$$
$$= H_m \nabla H_\alpha \times \nabla H_\beta + H_\alpha \nabla H_m \times \nabla H_\beta.$$

Integrating the above equation over the cross-section and applying Stokes's theorem, we have

$$\int_C H_m H_\alpha \nabla H_\beta \cdot d\mathbf{l} = \int_S H_m \nabla H_\alpha \times \nabla H_\beta \cdot d\mathbf{S} + \int_S H_\alpha \nabla H_m \times \nabla H_\beta \cdot d\mathbf{S}$$
$$= M_{m\alpha\beta} + M_{\alpha m\beta},$$

where $C$ is the boundary of the cross-section.

The left-hand side integration equals zero since $H_m$ and $H_\alpha$ vanish on the boundary $C$, so

$$M_{m\alpha\beta} + M_{\alpha m\beta} = 0.$$

Hence $M_{m\alpha\beta}$ is antisymmetric in the first and the second suffixes. Antisymmetry in the first and the third suffixes follows since

$$M_{m\alpha\beta} = -M_{m\beta\alpha} = M_{\beta m\alpha} = -M_{\beta\alpha m}.$$

# Appendix II

# The integration coefficients

$$\bar{g}_m = \int g_m(z)dz$$

$$\bar{g}_{m\alpha} = \int g_m(z)g_\alpha(z)dz$$

$$\bar{g}'_\alpha = \int \partial_z g_\alpha(z)dz$$

$$Q^{(1)}_{m\alpha k} = \int_\Gamma H_k[E_\alpha, E_m]d\Gamma$$

$$Q^{(2)}_{m\alpha k} = \int_\Gamma H_k \nabla H_\alpha \cdot \nabla E_m d\Gamma$$

$$Q^{(3)}_{m\alpha k} = \int_\Gamma H_\alpha \nabla H_k \cdot \nabla E_m d\Gamma$$

$$Q^{(4)}_{m\alpha k} = \int_\Gamma [E_\alpha, H_k]E_m d\Gamma$$

$$Q^{(5)}_{m\alpha k} = \int_\Gamma E_m \nabla H_k \cdot \nabla H_\alpha d\Gamma$$

$$Q^{(6)}_{mk} = \int_\Gamma \left(\lambda_k^2 H_k^2 + |\nabla H_k|^2\right) E_m d\Gamma$$

$$Q^{(7)}_{m\alpha k} = \int_\Gamma [H_\alpha, H_k]H_m d\Gamma$$

$$Q^{(8)}_{m\alpha} = \int_\Gamma \epsilon_{\alpha\beta 3}\partial_\alpha f_{m\alpha,3} H_m d\Gamma$$

$$Q^{(9)}_{m\alpha} = \int_\Gamma E_\alpha H_m d\Gamma$$

$$Q^{(10)}_{m\alpha} = \int_\Gamma \nabla H_\alpha \cdot \nabla E_m d\Gamma$$

$$Q^{(11)}_{m\alpha} = \int_\Gamma B_z E_\alpha H_m d\Gamma$$

$$Q^{(12)}_{m\alpha} = \int_\Gamma H_m \nabla B_z \cdot \nabla E_\alpha d\Gamma$$

$$Q^{(13)}_{m\alpha} = \int_\Gamma [B_z, H_\alpha]H_m d\Gamma$$

$$Q^{(14)}_{m\alpha} = \int_\Gamma B_z \nabla H_\alpha \cdot \nabla E_m d\Gamma$$

$$A_m = \rho^a g^a_m(0)||E_m||^2$$

$$B_m = -\rho^c g_m^c(0)||E_m||^2$$

$$C_{m\alpha} = \rho^a U_k^a g_\alpha^a(0) Q_{m\alpha k}^{(4)} d\Gamma + \rho^a \lambda_k^2 U_k^a \ \bar{g}_{m\alpha}^a \ Q_{m\alpha k}^{(1)} + k^a g_m^a(0)||E_m||^2$$

$$D_{m\alpha} = \rho^c U_k^c g_\alpha^c(0) Q_{m\alpha k}^{(4)} + \rho^c \lambda_k^2 U_k^c \ \bar{g}_{m\alpha}^c \ Q_{m\alpha k}^{(1)} - k^c g_m^c(0)||E_m||^2$$

$$E_{m\alpha} = \rho^a \lambda_\alpha^2 U_k^a \ \bar{g}_m^a \ Q_{m\alpha k}^{(3)} + \rho^a \lambda_k^2 U_k^a \ \bar{g}_m^a \ Q_{m\alpha k}^{(2)} + \rho^a U_k^a Q_{m\alpha k}^{(5)}$$

$$F_{m\alpha} = \rho^c \lambda_\alpha^2 U_k^c \ \bar{g}_m^c \ Q_{m\alpha k}^{(3)} + \rho^c \lambda_k^2 U_k^c \ \bar{g}_m^c \ Q_{m\alpha k}^{(2)} + \rho^c U_k^c Q_{m\alpha k}^{(5)}$$

$$G_{m\alpha} = -\ \bar{G}_{m\alpha} + (\rho^a - \rho^c)\, g||E_\alpha||^2 \delta_{m\alpha}$$

$$H_{m\alpha} = \frac{(U_k^a - U_k^c)}{||E_m||^2} Q_{m\alpha k}^{(4)}$$

$$I_{m\alpha} = \frac{U_k^a}{||E_m||^2} Q_{m\alpha k}^{(4)}$$

$$J_m = \lambda_m^2 ||H_m||^2$$

$$K_{m\alpha} = \bar{g}_\alpha^a \ \lambda_k^2 U_k^a Q_{\alpha k m}^{(3)}$$

$$L_{m\alpha} = \lambda_m^2 \frac{k^a}{\rho^a} ||H_m||^2 + \left(\lambda_\alpha^2 - \lambda_k^2\right) U_k^a Q_{m\alpha k}^{(7)}$$

$$M_{m\alpha} = -\frac{1}{\rho^a} Q_{m\alpha}^{(8)}$$

$$N_{m\alpha} = \bar{g}_\alpha^c \ \lambda_k^2 U_k^c Q_{\alpha k m}^{(3)}$$

$$O_{m\alpha} = \lambda_m^2 \frac{k^c}{\rho^c} ||H_m||^2 + \left(\lambda_\alpha^2 - \lambda_k^2\right) U_k^c Q_{m\alpha k}^{(7)}$$

$$P_{m\alpha} = -\frac{1}{\rho^c} Q_{m\alpha}^{(8)}$$

$$Q_m = \frac{1}{2} \left(\rho^a (U_k^a)^2 - \rho^c (U_k^c)^2\right) Q_{mk}^{(6)}$$

# Appendix III

# Analytic formulation of the wave evolution coefficients

Although most integrals in the wave evolution coefficients are somewhat complicated, fortunately they can be integrated analytically. Numerical integration using such methods as Gaussian Quadrature can also be an alternative for calculating the coefficients. Normally, it will take much time for the computation, while the analytic integration shortens the calculation time greatly. To simplify the integrals, the combination rule of trigonometric functions is used in the analytic formulation.

The functions $\bar{g}^a_\alpha$ and $\bar{g}^a_{m\alpha}$: As the integral form used in the $\bar{g}^a_\alpha$ and the $\bar{g}^a_{m\alpha}$ is part of a volume integral, the integration direction is chosen upward in the $z$-direction as follows;

$$\bar{g}^a_\alpha = \int_{-h^a}^{0} g^a_\alpha(z)dz = \frac{1}{2\lambda^2_\alpha \sinh \lambda_\alpha h^a}\left(e^{\lambda_\alpha h^a} - e^{-\lambda_\alpha h^a}\right),$$

$$\bar{g}^a_{m\alpha} = \int_{-h^a}^{0} g^a_\alpha(z) g^a_m(z)dz$$

$$= \frac{1}{4\lambda_\alpha (\sinh \lambda_\alpha h^a)\, \lambda_m (\sinh \lambda_m h^a)\, (\lambda^2_\alpha - \lambda^2_m)} \times$$

$$[\lambda_\alpha e^{\lambda_\alpha h^a + \lambda_m h^a} - \lambda_\alpha e^{(-\lambda_\alpha h^a - \lambda_m h^a)}$$

$$-\lambda_m e^{\lambda_\alpha h^a + \lambda_m h^a} + \lambda_m e^{(-\lambda_\alpha h^a - \lambda_m h^a)}$$

$$+\lambda_\alpha e^{\lambda_\alpha h^a - \lambda_m h^a} - \lambda_\alpha e^{(-\lambda_\alpha h^a + \lambda_m h^a)}$$

$$+\lambda_m e^{\lambda_\alpha h^a - \lambda_m h^a} - \lambda_m e^{(-\lambda_\alpha h^a + \lambda_m h^a)}].$$

The integration coefficient $Q^{(i)}_{m\alpha k}$: Using the combination rule of trigonometric functions, the integration coefficient $Q^{(1)}_{m\alpha k}$ is written as;

$$Q^{(1)}_{m\alpha k} = \int_\Gamma H_k[E_\alpha, E_m]d\Gamma$$

$$= \int_\Gamma H_k \partial_x E_\alpha \partial_y E_m d\Gamma - \int_\Gamma H_k \partial_y E_\alpha \partial_x E_m d\Gamma$$

$$= \left[\frac{-n_x\pi}{4}(\delta_{k_x,n_x+m_x} + \delta_{k_x,n_x-m_x})\right]\left[\frac{-m_y\pi}{4}(\delta_{k_y,n_y+m_y} - \delta_{k_y,n_y-m_y})\right]$$

$$-\left[\frac{-m_x\pi}{4}(\delta_{k_x,n_x+m_x} - \delta_{k_x,n_x-m_x})\right]\left[\frac{-n_y\pi}{4}(\delta_{k_y,n_y+m_y} + \delta_{k_y,n_y-m_y})\right]$$

$$= \frac{n_x m_y \pi^2}{16}(\delta_{k_x,n_x+m_x} + \delta_{k_x,n_x-m_x})(\delta_{k_y,n_y+m_y} - \delta_{k_y,n_y-m_y})$$

$$-\frac{m_x n_y \pi^2}{16}(\delta_{k_x,n_x+m_x} - \delta_{k_x,n_x-m_x})(\delta_{k_y,n_y+m_y} + \delta_{k_y,n_y-m_y}).$$

Similarly, we can obtain all other integration coefficients in the wave evolution equations analytically.

# Bibliography


[1] K.Ai, The hydrodynamics of the Hall-Héroult cell, *Light Metals*, pages 593-607, 1985.

[2] V.Almukhametov, V.Kolesnichenko and S.Khripchenko, Mathematical model of plane electrical eddy flows in a two layer conducting fluid, *Magnitnaya Gidrodinamika*, **2**, page 137, 1988.

[3] V.Almukhametov, V.Krukovsky, V.Kolesnichenko and S.Khripchenko, Magnetohydrodynamic phenomena in production of aluminium by electrolysis, *Light Metals*, TMS, Warrendale, PA, page 249, 1990.

[4] D.Andrews, A conservation law for small-amplitude quasi-geostrophic disturbances on a zonally asymmetric basic flow, *J.Atmos. Sci.*, **40**, pages 85-90, 1983.

[5] J.Antille, M.Flueck, and M.V.Romerio, Steady velocity field in aluminium reduction cells derived from measurements of the anodic current fluctuations, *Light Metals*, pages 305-312, 1994.

[6] V.I.Arnol'd, Conditions for nonlinear stability of stationary plane curvilinear flows of an ideal fluid, *Dokl. Akad. Nauk. SSSR*, **162**, pages 975-978, 1965.

[7] V.I.Arnol'd, On an a priori estimate in the theory of hydrodynamic stability, *Amer.Math.Soc.Trans.2*, **79**, pages 267-269, 1969.

[8] G.Batchelor, On steady laminar flow with closed streamlines at large Reynolds number, *Journal of Fluid Mechanics*, **4**, pages 177-190, 1956.

[9] G.Batchelor, *An introduction to fluid dynamics*, Cambridge University Press, 1967.

[10] B.J.Bayly, Three-dimensional centrifugal-type instabilities in inviscid two-dimensional flows, *Phys. Fluids*, **31**, pages 56-64, 1988.

[11] R.Bird, W.Stewart, and E.Lightfoot, *Transport phenomena*, Wiley, 1960.

[12] R.Boivin and S.Martel, Effect of an instability of the metal surface on the magnetic field inside a cell, *Light Metals*, pages 233-241, 1990.

[13] V.Bojarevics and M.V.Romerio, Long waves instability of liquid metal-electrolyte interface in aluminium electrolysis cells: a generalization of Sele's criterion, *European Journal of Mechanics, B/Fluids*, pages 33-56, 1994.

[14] S.Cherchi and G.Degan, Oscillation of liquid aluminium in industrial reduction cells: an experimental study, *Light Metals*, pages 457-467, 1983.

[15] P.A.Davidson, An energy analysis of unstable, aluminium reduction cells, *European Journal of Mechanics, B/Fluids*, **13**, pages 15-32, 1994.

[16] P.A.Davidson and R.F.Boivin, Hydrodynamics of aluminium reduction cells, *Magnetohydrodynamics in Process Metallurgy*, pages 111-116, 1992.

[17] P.A.Davidson and R.I.Lindsay, Stability of interfacial waves in aluminium reduction cells, *Journal of Fluid Mechanics*, **362**, pages 273-295, 1998.

[18] A.S.Derkachi and V.I.Shitern, Influence of the instability of line current in aluminium reduction cells, *Tsvvetnye Metally*, **40**, No.3, pages 57-61, 1967.

[19] E.Dernedde and E.L.Cambridge, Gas induced circulation in an aluminium reduction cell, *AIAE Annual Meeting*, New York, Feb 1975.

[20] J.Descloux, M.Flueck, and M.V.Romerio, Modeling for instability in Hall-Héroult cells: mathematical and numerical aspects, *Magnetohydrodynamics in Process Metallurgy*, pages 107-116, 1992.

[21] J.Descloux and M.V.Romerio, On the analysis by perturbation methods of the anodic current fluctuations in an electrolytic cell for Al, *Light Metals*, pages 237-243, 1989.

[22] P.G.Drazin and W.H.Reid, *Hydrodynamic stability*, Cambridge University Press, 1981.

[23] X.N.Duc, Etude théorique et expérimentale sur un modèle hydraulique d'instabilitiés de Rayleigh-Taylor en magnétohydrodynamique, *C.R. Acad. Sc.* Paris, Series A, **226**, page 738, 1968.

[24] M.Echelini, O.Cobo, M.Lacunza, N.Crespo, J.Romagnoli and N.Capiata, Expansion of a pot line with the aid of mathematical modeling, *Light Metals*, page 557, 1988.

[25] Y.Fautrelle, Free surface electromagnetic instabilities in liquid metals, *Magnetohydrodynamics in Process Metallurgy*, pages 63-68, 1991.

[26] B.A.Finlayson, *The Method of weighted residuals and variational principles*, Academic Press, New York, 1972.

[27] R.Fjortoft, On the stability of quasigeostrophic flow, *J. Atmos. Sci.*, **25**, pages 929-931, 1968.

[28] K.Grjotheim and B.J.Welch, Aluminium smelting technology — a theoretic and applied approach, *Aluminium-Verlag*, 1988.

[29] T.Iuchi, Rise and flow of molten metal in aluminium reduction cells, *AIME Anual Meeting, Denver*, 1970.

[30] A.Johnson, Metal pad velocity measurements in aluminium reduction cells, *Light Metals, The Met. Soc. of ASME, New-York*, **1**, pages 45-58, 1978.

[31] A.Johnson, The modeling of aluminium extraction technology, *Journal of Metals*, pages 11-13, 1988.

[32] J.H.Kent, A study of magnetic screens and the effect of pot room structure on current efficiency, *Light Metals*, page 215, 1989.

[33] A.Kovetz, *The principles of electromagnetic theory*, Cambridge University Press, page 146, 1990.

[34] E.Kreyszig, *Advanced engineering mathematics*, John Wiley and Sons Inc., pages 418-419, pages 422-425, 1967

[35] A.F.LaCamera, D.P.Ziegler, and R.L.Kozarek. Magnetohydrodynamics in the Hall-Héroult process, an overview, *Magnetohydrodynamics in Process Metallurgy*, pages 91-98, 1991.

[36] H.Lamb, *Hydrodynamics*, Cambridge University Press, 1932.

[37] R.LeBlanc, V.Potočnik, G.Stockman and D.Shannon, Magnetohydrodynamic analysis of VS soderberg cells, *Light Metals*, page 575, 1988.

[38] G.Lobmann, Utilization of various combined measurements in reduction cells for operation improvement, *Light Metals*, pages 441-447, 1992.

[39] S.D.Lympany, J.W.Evans, and R.Moreau. Hall-Héroult cell: Some design alternatives evaluated by mathematical model. *Met. Trans. B*, page 63, 1983

[40] S.D.Lympany, J.W.Evans, and R.Moreau. Magnetohydrodynamic effects in aluminium reduction cells, *Proc. IUTAM Symp. on metallurgical applications of magnetohydrodynamics*, page 15, 1984.

[41] E.Matsui, Measurement of metal turbulence in aluminium reduction cells, *Light Metals*, pages 373-389, 1982.

[42] M.E.McIntyre and T.G.Shepherd, An exact local conservation theorem for finite amplitude disturbances to non-parallel shear flows, with remarks on Hamiltonian structure and on Arnol'd's stability theorems, *Journal of Fluid Mechanics*, **181**, pages 527-565, 1987.

[43] H.Medina and N.Elarba, Modernization of venalum pots to meet new requirements and higher performance, *Light Metals*, page 623, 1988.

[44] A.J.Mestel, On the stability of high-Reynolds-number flows with closed streamlines, *Journal of Fluid Mechanics*, **200**, pages 19-38, 1989.

[45] A.J.Mestel, An iterative method for high Reynolds number flows with closed streamlines, *Journal of Fluid Mechanics*, **200**, pages 1-18, 1989.

[46] J.L.Meyer, Electromagnetic processes in aluminium casthouses and foundries: an overview, *Magnetohydrodynamics in Process Metallurgy*, pages 127-143, 1992.

[47] H.K.Moffatt, *Magnetic field generation in electrically conducting fluids*, Cambridge University Press, 1978.

[48] H.K.Moffatt, Magnetostatic equilibria and analogous Euler flows of arbitrarily complex topology, Part 2. stability considerations, *Journal of Fluid Mechanics*, **166**, pages 359-378, 1986.

[49] R.J.Moreau, *Magnetohydrodynamics*, Kluwer Academic Publishers, 1990.

[50] R.J.Moreau, Solidification under magnetic field: mechanism, expected results, challenges, *Magnetohydrodynamics in Process Metallurgy*, pages 15-20, 1992.

[51] R.J.Moreau and J.W.Evans, An analysis of the hydrodynamics of aluminium reduction cells, *J. Electrochem. Soc.*, page 251, 1984.

[52] R.J.Moreau and D.Ziegler, Stability of aluminium cells — a new approach, *Light Metals*, page 359, 1986.

[53] R.J.Moreau and D.Ziegler, Moreau-Evans hydrodynamic model applied to actual Hall-Héroult cells, *Metallurgical Transactions B* , page 573, 1976.

[54] K.Mori, K.Shiota, N.Urata and H.Ikeuchi, The surface oscillation of liquid metal in aluminium reduction cells, *Light Metals*, page 77, 1976.

[55] K.Mori, N.Urata and H.Ikeuchi, Behaviour of the bath molten metal in an aluminium electrolytic cell, *J. Japan Inst. Light Metals*, page 573, 1976.

[56] A.H.Nayfeh and D.T.Mook, *Nonlinear oscillations*, Wiley, 1979.

[57] S.Pigny and R.Moreau, Stability of fluid interfaces carrying an electric current in the presence of a magnetic field, *European Journal of Mechanics, B/Fluids*, page 77, 1992.

[58] V.Potŏcnik, A-275 MHD design, *Light Metals*, page 203, 1987.

[59] V.Potŏcnik, Modeling of metal-bath interface waves in Hall-Héroult cells using ESTER/PHOENICS, *Light Metals*, pages 227-235, 1990.

[60] V.Potŏcnik, Principle of MHD design of aluminium electrolysis cells, *Proc. IUTAM symp. on metallurgical applications of magnetohydrodynamics*, pages 99-105, 1991.

[61] W.Press, S.Teukolsky, W.Vetterling and B.Flannery, *Numerical recipes in Fortran 90*, Cambridge University Press, 1996.

[62] Lord Rayleigh, On the stability of a magnetically driven rotating fluid flow, *Proc. Lond. Math. Soc.,* **10**, pages 4-13, 1880.

[63] A.T.Richardson, On the stability of a magnetically driven rotating fluid flow, *Journal of Fluid Mechanics*, **63**, pages 593-605, 1974.

[64] I.S.Robinson, A novel form of the MHD Rayleigh-Taylor instability, *Journal of Fluid Mechanics*, **72**, page 135, 1975.

[65] M.Segatz and C.Droste, Analysis of magnetohydrodynamic instabilities in aluminium reduction cells, *Light Metals*, pages 313-321, 1994.

[66] M.Segatz and D.Vogelsang, Effect of steel parts on magnetic fields in aluminium reduction cells, *Light Metals*, pages 393-398, 1991.

[67] M.Segatz, D.Vogelsang, C.Droste, and P.Baekler, Modeling of transient magnetohydrodynamic phenomena in Hall-Héroult cells, *Light Metals*, 1993.

[68] T.Sele, Magnetic fields, flows, and stability for electrolytic aluminium reduction cells, *Ext. Abs. Mtg. Inter. Soc. Electrochem. Trondheim*, page 5, 1975.

[69] T.Sele, Instabilities of the metal surface in electrolytic alumina reduction cells, *Metal Transaction B*, 1977.

[70] T.Sele, Instabilities of the metal surface in electrolytic cells, *Light Metals*, 1977.

[71] T.Sele, Electromagnetic interactions in Hall-Héroult cells, *International Course on Process Metallurgy of Aluminium*, 1985.

[72] A.D.Sneyd, Stability of fluid layers carrying a normal electric current, *Journal of Fluid Mechanics*, **156**, pages 223-236, 1985.

[73] A.D.Sneyd, Interfacial instability in aluminium reduction cells , *Journal of Fluid Mechanics*, **236**, pages 111-126, 1992.

[74] A.D.Sneyd and A.Wang, Interfacial instability due to MHD mode coupling in aluminium reduction cells, *Journal of Fluid Mechanics*, **263**, pages 343-359, 1994.

[75] B.Straughan, *The Energy method, stability, and nonlinear convection*, Springer-Verlag, 1992.

[76] J.Szekely, J.W.Evans, K.Blazek, and N.Eikaddah, editors, Magnetohydrodynamics in process metallurgy, *The Minerals, Metal & Materials Society*, 1992.

[77] N.Urata, Magnetic and metal pad instability, *Light Metals*, pages 581-591, 1985.

[78] N.Urata, Y.Arita, and H.Ikeuchi, Magnetic field and flow pattern of liquid aluminium in the reduction cells, *AIME Annual Meeting*, New York, Feb 1975.

[79] N.Urata, K.Mori and H.Ikeuchi, Behavior of the bath and molten metal in an aluminium electrolytic cell, *J. Japan Inst. Light Metals*, **26**(11), page 573, 1976.

[80] D.Vogelsang and M.Segatz, Simulation tools for the development of high-amperage reduction cells, *Light Metals*, pages 375-379, 1991.

[81] D.Vogelsang, M.Segatz, C.Droste, P.Baekler, and R.Stucher, Development of a 300-kA reduction cell: application of simulation tools for the conceptual design, *Light Metals*, 1994.

[82] W.E.Wahnsiedler, Hydrodynamic modeling of commercial Hall-Héroult cells, *Light Metals*, pages 269-287, 1987

[83] A.Wang, MHD Interfacial instability in aluminium reduction cells, D.Phil Thesis, *University of Waikato*, pages 140-151, 1996.

[84] G.B.Whitham, *Linear and nonlinear waves*, John Wiley & Sons Inc., 1973.

[85] D.Ziegler, Stability of metal/electrolyte interface in Hall-Héroult cells : effects of the steady velocity, *Metallurgical Transactions B*, **24B** , pages 889-906, 1993.

[86] V.Zimin and N.Kolpakov, *Magnitnaya Gidrodinamika*, **3**, page 89, 1990.

[87] A.Zwart, Bubble driven waves in aluminium reduction cells, D.Phil Thesis, *University of Waikato*, 1998.